DISSERTATION

BIOENGINEERING OF CLONEABLE INORGANIC NANOPARTICLES

Submitted by

Alexander Ryo Hendricks

Department of Chemistry

In partial fulfilment of the requirements

For the Degree of Doctor of Philosophy

Colorado State University

Fort Collins, Colorado

Summer 2023

Doctoral Committee:

Advisor: Christopher J. Ackerson

Jean Chung
Andy McNally
Bob Cohen

ABSTRACT

BIOENGINEERING OF CLONEABLE INORGANIC NANOPARTICLES

When a defined protein/peptide (or combinations thereof) control and define the synthesis of an inorganic nanoparticle, the result is a cloneable NanoParticle (cNP). This is because the protein sequence/structure/function is encoded in DNA, and therefore the physicochemical properties of the nanoparticle are also encoded in DNA. Thus the cloneable nanoparticle paradigm can be considered as an extension of the central dogma of molecular biology (e.g. DNA -> mRNA -> Protein -> cNP); modifications to the DNA encoding a cNP can modify the resulting properties of the cNP. The DNA encoding a cNP can be recombinantly transferred into any organism. Ideally, this enables recombinant production of cNPs with the same defined physiochemical properties. Such cNPs are of primary interest for applications in biological imaging as clonable contrast agents. The advancement of cNPs for broader and more rigorous applications in imaging (and elsewhere) requires further development through multidisciplinary approaches. Described in This Thesis is a bioengineering approach to improve the cNP platform through development of the enzymes responsible for nanoparticle formation.

In the first chapter, background and significance is given to provide rationale behind the cNP platform. Among all the modalities of biological imaging, there is no 'one-size-fits-all' solution. Biological fluorescence microscopy (FM) and electron microscopy (EM) are the preferred methods of choice when imaging at cellular levels. Although the relatively recent advent of fluorescent proteins and super-resolution microscopy have ushered major scientific breakthroughs, FM is resolution-limited: only the cellular components which are labeled by fluorophores can be resolved – everything else in a cell (~99% of components) is imaged with low resolution owing to the diffraction limit of light. Biological EM comparatively can image widefield cells at atomic-level resolution yet lacks an analogous toolset to

fluorescent proteins. cNPs are proposed as a multimodal, uniform, and precise means of clonable contrast for biological EM (and other modalities) analogous to fluorescent proteins.

In the second chapter, a tellurium reductase is isolated and characterized from screened environmental bacterial cultures collected throughout the Colorado Mineral Belt. A strain of *Rhodococcus erythropolis* PR4 was found to be highly resistant to a broad range of metal(loid) species at toxic concentrations – notably 4.5 mM TeO_3^{2-} determined by broth microdilution. Through screening of cell lysate in the presence of metal(loid) substrates, a mycothione reductase was characterized as a Te-specialized enzyme which reduces Te preferentially over Se. This is a surprising finding on the basis of reduction potentials for the two substrates. The standard reduction of potential for the reaction TeO_3^{2-} + 3 H_2O + 4e^- ← → Te + 6 OH^- is −0.57 V vs Hydrogen. The corresponding reduction of SeO_3^{2-} is −0.366 V. Thus, SeO_3^{2-} is the preferred substrate for reduction in the absence of a mechanism for substrate selectivity. We hypothesize that the *R. erythropolis* mycothione reductase may form the basis of a cloneable tellurium nanoparticle (cTeNP).

In the third chapter, metal(loid) reductase substrate specificity is developed through directed evolution of a glutathione reductase-like metalloid reductase (GRLMR). The native substrate of GRLMR is selenodiglutathione (GS-Se-SG), where zerovalent selenium nanoparticles are formed in the presence of NADPH. Error prone polymerase chain reaction was used to create a library of ~100,000 GRLMR variants. The library was expressed in *Escherichia coli* with 50 mM SeO_3^{2-} to select a GRLMR variant with 2 mutations. One mutation (a D to E) appears to be silent, whereas the other (L to H) resides within 5Å of the active site. Compared to the GRLMR parent enzyme, the evolved enzyme became less capable of reducing reduced glutathione (GSSG) and GS-Se-SG in favor of SeO_3^{2-}. The evolved enzyme also gained an ability to reduce SeO_4^{2-}. We have described this enzyme as a selenium reductase (SeR). This is the first known instance of the substrate specificity profile of a metal(loid) reductase changing as a result of directed evolution.

In the fourth chapter, the cNP concept is discussed in greater detail. The cNP synthesis paradigm is loosely defined as a system of ligands, reductants, and inorganic cations – where ligands are peptides, reductants are enzyme-cofactor pairs, and inorganic cations are dietary or supplemented metal(loid) ions. This modular platform is adaptable to a wide variety of metal(loid)/enzyme/peptide systems. The story of the creation of a cloneable Se nanoparticle (cSeNP) is also retraced. Briefly, a bacterial endophyte *Pseudomonas moraviensis* subsp. Stanleyae was found to be capable of efficient selenium reduction under aerobic conditions. Continued characterization led to the discovery of GRLMR which unraveled the cellular mechanism for reducing SeO_3^{2-}. The enzyme can endow host cells with selenium resistance through nanoparticle formation when cloned. GRLMR was further modified through the fusion of a selenium nanoparticle-binding peptide which improved overall kinetic rates, nanoparticle retention, and nanoparticle uniformity.

In the fifth chapter, preliminary work is described which may enable further development of the next generation of cNPs through reduced enzyme mass/mericity and 'multicolored' nanoparticles. Work is described which investigates the plasticity of GRLMR towards reducing other metals such as bismuth. Fluorescence assisted cell sorting (FACS) was used to determine if the relative quantity of intracellular metal(loid) nanoparticles can be differentiated, which is hypothesized to correlate to relative metal(loid) reductase activity. Whereas selenium content could be discerned between active and inactive GRLMR-expressing bacteria, relative bismuth content has yet to be analogously discerned. On the other hand, work was done towards rationally designing a monomeric GRLMR; there are ongoing efforts to use machine learning to graft the active site of GRLMR into a different monomeric template. Finally, a *Muchor racemosus* cytochrome b5 reductase (Cb5R) was identified in the literature which may serve as an ideal candidate to develop more minimalistic cSeNPs. Initial work has revealed that the enzyme is particularly resistant to soluble expression, which may hinder its ability to function as a clonable contrast agent. However, ongoing work is being done to 'supercharge' the enzyme to enable more facile expression.

Manuscript text adapted for dissertation submission[1–3]*. (1) Author contributions:* ***ARH*** *(lead author), BG (2nd author), RC, GE, TT (co-authors), and CJA (principal investigator) wrote initial draft and edited. KMB (co-author) edited. (2) Author contributions: ZJB (lead author) and* ***ARH*** *(2nd author) conducted experiments, wrote initial draft, and edited. KMB (co-author) conducted experiments. CJA (principal investigator) edited. (3) Author contributions:* ***ARH*** *(lead author) and RC (2nd author) conducted experiments, wrote initial draft, and edited. GE, TT, BG, and AA (co-authors) conducted experiments and wrote initial draft. CJA (principal investigator) wrote initial draft edited. CS (co-principal investigator) edited.*

AKNOWLEDGEMENTS

My path to getting a PhD only became reality through contributions of the many incredible mentors, peers, and friends I've met along the way. Acknowledging some here in text is but an insignificant demonstration of my gratitude.

First and foremost, my sincerest thanks towards Prof. Chris Ackerson who advised me through (most of) the PhD program. Working under your guidance, I learned as much about living life in a positive and meaningful way as I did about science and research. You generously provided the environment and encouragement for me to consider and pursue what I *really* want to do with the rest of my life. Should I achieve my greatest dreams, it will be a testament to the unique privilege I've had being mentored by you. Your lab's culture is something truly special and reflects the kind and thoughtful way you treat people. Should there ever be an instance where I might be capable of assisting in any way, I hope that you will not hesitate to ask.

Scott Compel - Throughout the time that we've known each other, you've fulfilled roles as a close friend, a colleague, a mentor, and an employer. Thank you for helping me navigate graduate school and for being so generous with your time and resources. I'm looking forward to seeing what happens with AEMS Corp., along with all the other phenomenal colleagues that have assembled.

James Armstrong, Ryan Riskowski, Marcus Tofanelli, Zach Butz, Phillip Window, Ian Anderson, Collin Perry, Bradley Guilliams, and the long list of other Ackerson Lab alumni who have helped me through some of my worst moments in graduate school and have created some of my most enjoyable memories - I'm lucky to have been surrounded by such exemplary and entertaining colleagues. And even luckier yet that so many of you have become lifelong friends.

To the younger students of the Ackerson Lab – it's been great seeing you all readily propagating the positive work culture and bringing your own unique blend. The future of our alumni association is in

your hands – be sure to carry a legacy of excellence and pass it along to the following generations. I'm looking forward to hearing about the exciting research you undertake in the coming years. Don't hesitate to reach out for anything I can assist with!

Jenn Bjerke and Patrick Beardslee - thank you for taking me under your wing in my first few months in Colorado. Looking back, each of you had such a profound impact on my life in such a short amount of time. I'm glad we went through those tough times together, and that we've been able to stay so close in the aftermath.

Prof. Rick Wagner, and other members of the Wagner Lab who prepared me for graduate school. Rick - I distinctly remember you saying you'd "be willing to take a risk" on me working in your lab as an undergrad (after reviewing my professional and academic background at the time). To think of how far I've come since then, and where else I might be now if not for that risk…

Prof. Sidath Kumarapperuma - I still hear your voice in my head when setting up experiments or thinking about results. I wasn't ready for many of your lessons back then, but they stuck with me, and I realized how profound they were many years later. You were right – confidence was the biggest thing I lacked back when we worked together. If my skills as a mentor (and patience) reach a fraction of what you are capable of, then I'll consider myself to be very successful teacher.

Prof. Will Pomerantz – your class was one of the few chemistry classes I enjoyed as an undergraduate student. If not for the enthusiasm we shared for biological chemistry, I probably never would have considered applying for graduate school.

Jay Scovil – one of my high school English teachers. You pulled me out of the classroom once (I thought I was in trouble) to specifically compliment my writing projects. Writing intensive courses were my only saving grace through all the dark years in college – I attribute that to the confidence you helped me build in myself.

CSU peers and faculty - Nancy Levinger, Debbie Crans, Chris Snow, Jean Chung, and other professors of the CSU chemistry department who have made themselves invaluable resources to my education. Julius Stewart - my one lone chemical biology compatriot in the department who I could bounce research ideas around. And everyone who helped make the Biological Chemistry Initiative Group a reality. Science is always more fun when it can be shared with others.

To Kyle Pingeon, Andrew Walsh, Nikki Andresen, Chirag Patel, Eli Watson, Joey Glapa, Rob Tuttle, Amy Fleshman, Ryan Terry, Steve Shields, Ryan Rickert, and so many of the 'Colorado Adventurers' - friends who built me up, kept my ego in check, and generally made life enjoyable. If not for your friendships I wonder if I could have persevered through all the emotional hardships of graduate school.

My uncle Randy – thanks for going out of your way to introduce me to Fort Collins and all the help with moving across the country.

To my girlfriend, Chelsea Ducote – who has made life so much more interesting and enjoyable.

And to my mother, Yukari Hendricks - who has never ceased to show support.

A sincere thanks to you all!

TABLE OF CONTENTS

ABSTRACT ii

ACKNOWLEDGEMENTS vi

CHAPTER 1: BACKGROUND AND SIGNIFICANCE

1.1 INTRODUCTION 1

1.2 IMAGING AT CELLULAR LEVELS 2

1.3 MODERN BIOLOGICAL EM IS POWERFUL, BUT LIMITED 3

1.4 A PHYSICAL BASIS FOR RELATIVE CONTRAST 4

1.5 THE CONTRAST PROBLEM 4

1.6 CHEMICAL CONTRAST AGENTS 6

1.7 ANTIBODY BASED CHEMICAL CONTRAST AGENTS 7

1.8 CLONEABLE CONTRAST AGENTS 8

1.9 CLONEABLE NANOPARTICLES ARE PROPOSED AS MORE EFFECTIVE CONEABLE CONTRAST TAGS 10

CHAPTER 2: IDENTIFICATION OF A TeO_3^{2-} REDUCTASE/MYCOTHIONE REDUCTASE FROM RHODOCOCCUS ERYTHROPOLIS PR4

2.1 INTRODUCTION 12

2.2 RESULTS AND DISCUSSION 13

2.2.1 IDENTIFICATION AND SELECTIVITY OF A TE-REDUCTASE 13

2.2.2 KINETICS STUDY OF TE-REDUCING MTR 16

2.2.3 A STRUCTURAL BASIS FOR TE SELECTIVITY 19

2.2.4 MTR MEDIATED TE-NANOSTRUCTURES 21

2.3 SUMMARY AND CONCLUSION 22

2.4 MATERIALS AND METHODS 22

2.4.1 METAL SCREENING OF LYSATES 23

2.4.2 LC-MS/MS SAMPLES PREPARATION 23
2.4.3 LC-MS/MS MASS SPECTROMETRY ANALYSIS 24
2.4.4 LC-MS/MS DATA ANALYSIS 24
2.4.5 PLASMID CONSTRUCTION 25
2.4.6 MYCOTHIONE REDUCTASE ISOLATION 26
2.4.7 KINETICS STUDIES 26
2.4.8 SCANNING ELECTRON MICROSCOPY 27
2.4.9 ICP-MS 27
2.4.10 SELECTIVITY ASSAY 27
CHAPTER 3: LABORATORY EVOLUTION OF METALLOID REDUCTASE SUBSTRATE RECOGNITION AND NANOPARTICLE PRODUCT SIZE
3.1 INTRODUCTION 28
3.2 RESULTS AND DISCUSSION 31
3.2.1 ENZYME KINETICS 31
3.2.2 ENZYME SUBSTRATE SELECTIVITY 33
3.2.3 TELLURIUM SUBSTRATES 33
3.2.4 STRUCTURAL BASIS FOR CHALCOGENIDE OXYANION SELECTION 34
3.2.5 SER AND GRLMR SENP PRODUCT CHARACTERIZATION 38
3.2.6 GRLMR VARIANT LIBRARY CREATION 41
3.2.7 LIBRARY SELECTION STRATEGY 41
3.2.8 INACTIVATING GRLMR WITH C42A AND C47A MUTATIONS 42
3.2.9 C42, C47 MUTANTS TO GRLMR DO NOT REDUCE SELENITE 43
3.2.10 DEVELOPMENT OF LIVE/DEAD SELECTION SYSTEM 44
3.2.11 SELECTION FOR IMPROVED SE REDUCTION 44
CHAPTER 4: CLONEABLE INORGANIC NANOPARTICLES
4.1 INTRODUCTION 47
4.1.1 THE CNP SYNTHESIS PARADIGM 49

4.1.2 CNP COMPOSITION PARAMETERS 50

4.1.3 CLONEABLE CONTRAST 53

4.2 PAPER SUMMARIES 56

4.2.1 PSEUDOMONAS MORAVIENSIS SUBS. STANLEYAE, A BACTERIAL ENDOPHYTE HYPERACCUMULATOR STANLEYA PINNATA, IS CAPABLE OF EFFICIENT SELENITE REDUCTION TO ELEMENTAL SELENIUM UNDER AEROBIC CONDITIONS 56

4.2.2 PROGRESS TOWARDS CLONABLE INORGANIC NANOPARTICLES 59

4.2.3 METALLOID REDUCTASE OF PSEUDOMONAS MORAVIENSIS STANLEYAE CONVEYS NANOPARTICLE MEDIATED METALLOID TOLERANCE 64

4.2.4 METALLOID REDUCTASE ACTIVITY MODIFIED BY A FUSED SE BINDING PEPTIDE 67

4.2.5 MOTIVATION FOR 'MULTI-COLOR' CNPS 72

4.2.6 IDENTIFICATION OF A TEO3 2- REDUCTASE/MYCOTHIONE REDUCTASE FROM RHODOCOCCUS ERYTHROPOLIS PR4 73

4.2.7 ENZYME-CATALYZED IN SITU SYNTHESIS OF TEMPORALLY AND SPATIALLY DISTINCT CDSE QUANTUM DOTS IN BIOLOGICAL BACKGROUNDS 77

4.2.8 OTHER APPROACHES TO CLONEABLE CONTRAST IN EM 78

4.2.9 METALLOTHIONEIN AS A CLONEABLE TAG FOR PROTEIN LOCALIZATION BY ELECTRON MICROSCOPY OF CELLS 79

4.2.10 DPS AS A CLONEABLE TAG 83

4.3 OUTLOOKS AND FUTURE DIRECTIONS FOR CNPS 85

4.4 CONCLUSIONS 87

CHAPTER 5: ENGINEERING THE NEXT GENERATION OF CLONEABLE NANOPARTICLES

5.1 INTRODUCTION 89

5.2 EVOLVING 'MULTICOLOR' CNPS 92

5.2.1 PRELIMINARY EXPERIMENTS WITH GRLMR 93

5.2.2 SORTING DATA - SELENITE 94

5.2.3 BISMUTH-GLUTATHIONE AND BISMUTH-CYSTEINE SYNTHESES 95

5.2.4 CONCLUSIONS AND FUTURE DIRECTIONS 96

5.3 MINIMALIZATION OF CNP ENZYMES 97

5.3.1 MONOMERIZATION OF GRLMR (M-GRLMR) 97

5.3.2 EXPERIMENTAL APPROACH AND DESIGN 98

5.3.3 MOLECULAR CLONING AND PROTEIN EXPRESSION 99

5.3.4 MOLECULAR DYNAMICS SIMULATIONS 100

5.3.5 M-GRLMR CONCLUSIONS AND FUTURE DIRECTIONS 100

5.3.6 MUCHOR RACEMOSUS CYTOCHROME B5 REDUCTASE 101

5.3.7 CB5R – RESULTS AND DISCUSSION 101

5.3.8 CB5R – CONCLUSIONS AND FUTURE DIRECTIONS 102

5.4 CONCLUSIONS AND FUTURE DIRECTIONS 103

5.5 MATERIALS AND METHODS 104

5.5.1 MOLECULAR CLONING 105

5.5.2 PROTEIN EXPRESSION 106

5.5.3 NATIVE-PAGE AND SDS-PAGE 106

5.5.4 FACS EXPERIMENTS 107

REFERENCES 108

APPENDIX A – SUPPLEMENTAL TO CHAPTER 2 125

APPENDIX B – SUPPLEMENTAL TO CHAPTER 3 132

CHAPTER 1: BACKGROUND AND SIGNIFICANCE

1.1 Introduction

A greater understanding of biological systems necessitates visualizing constituent parts in their respective contexts with high resolution and contrast. For instance, visually mapping the course of viral infections in microscopic cells or in macroscale tissues can inform better means of prevention and treatment[4–7]. Alternatively, observing intricate developmental patterns of neurons throughout the lifetime of model organisms can offer deeper insights into the nature of our own consciousness[8–10]. Imaging of biological materials is nevertheless a complex process in its own right, and the scope of questions that can be asked and answered is limited by the extent of capabilities offered by existing technologies.

There is no 'one-size-fits-all' imaging modality (i.e., method of imaging) when it comes to comprehensively visualizing biological systems, the components of which can range in size from small biomolecules (nanometer-scale) to comparatively gargantuan organisms (meter-scale). One of the primary reasons no such modality exists is because there are intricate trade-offs between different aspects of image quality; for instance, higher resolutions (i.e., the degree of detail in an image) are often associated with diminished imaging depths[11] . Distinct imaging modalities are therefore more or less appropriate in given contexts according to their inherent strengths and weaknesses (**Figure 1.1**). As an example, positron emission tomography (PET) penetrates through several meters of tissue but is unable to resolve constituents below 4-5 mm[12]; ultrasound can comparatively resolve below 1 mm but has a tissue penetration limit of about 30 cm[11]. Analogous trade-offs in image quality also exist within the scope of each respective modality: e.g., ultrasound is less resolved when imaging at greater tissue depths. Although there are continual efforts to address these limitations and others within each respective focus

area, it is unlikely that a paragon imaging method which encapsulates the totality of known biology will be developed within a foreseeable future.

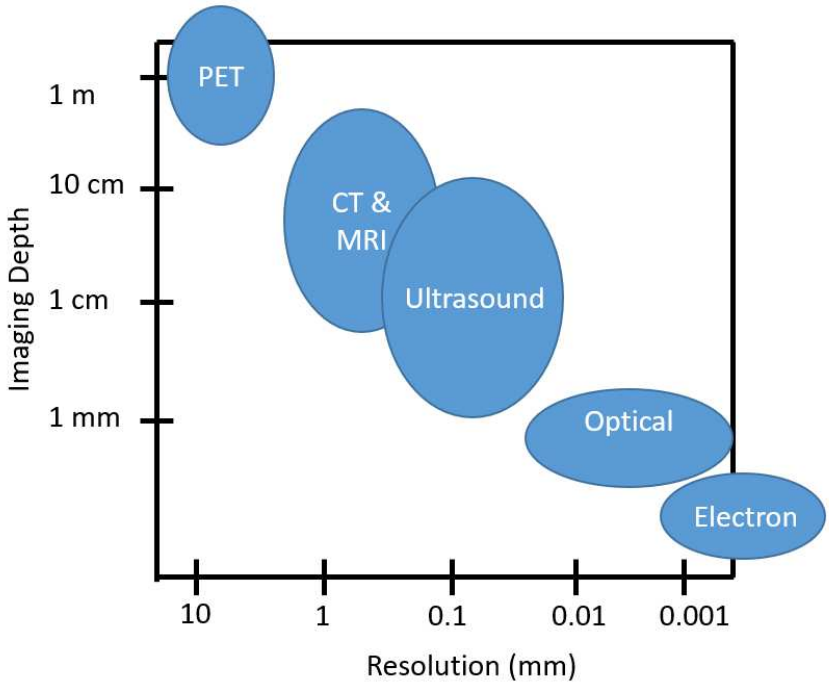

Figure 1.1: Rough comparisons of mainstream bio-imaging modalities, with respect to relative imaging depth (Y-axis) and resolution (X-axis)

1.2 Imaging at cellular levels

When it comes to imaging within the ballpark of cellular-level systems (which encompass the nanometer to micrometer size scale), optical fluorescence microscopy (FM) and electron microscopy (EM) are widely recognized as the prevailing players. Relatively high magnifications can also be attained by using other short wavelength energy sources such ultraviolet[13], neutrons[14], or X-ray microscopy[15]; however, these techniques are underdeveloped for small-scale biological imaging, largely in part due to key drawbacks such as rapid sample destruction, a lack of sufficient baseline contrast, or limitations in the current array of available instrumentation (respectively).

Mainstream FM techniques are among the most favorable for their relatively low cost, ease of sample preparation, and indispensable ability to track temporally dynamic processes such as those found

in living cells[16]. On the other hand, FM is resolution-limited by Abbe's diffraction limit which roughly translates to one-half the wavelength of light (e.g., 500 nm green light can be limited to approximately 250 nm resolution). This resolution limit is a significant hindrance when considering the size profile of viruses (~100s of nm), proteins (~10s of nm), and other smaller biomolecules.

While relatively recent advancements in super-resolution FM techniques have overcome Abbe's diffraction limit in certain instances (in some cases to nearly 5-10 nm resolution), they can present additional caveats such as extended laser exposure times and high excitation energies which may adversely affect living specimens[17–19]. Super-resolution moreover only resolves the few molecules that are labeled with fluorophores to high resolution; everything else in the cell that is not fluorophore labeled (typically 99% of cellular constituents) is imaged at wavelength-limited resolutions.

The ever-increasing demands of scientific inquiry require greater depths of information than what FM alone can provide. Although it is expected that the field of FM will find continual advancements, the inherent nature of how incident imaging energies (in this case, photons) physically interact with sample material dictates what information can be obtained by microscopists: photons can only shed light on systems that are responsive to photons. In this sense, FM delivers an insightful yet inherently incomplete perspective on the highly complex milieux of available (but yet unrevealed) information within cells.

1.3 Modern biological EM is powerful, but limited

With the use of electrons, EM can comparatively achieve wide-field atomic-level (sub-nanometer) resolution while obtaining alternative information such as elemental composition (e.g., through electron energy-loss spectroscopy[20]) and crystallinity. While the past several decades-worth of major scientific discoveries in subcellular systems have been primarily through FM, recent technological advancements have ushered a renaissance in biological EM[21]. Cryogenic EM (Cryo-EM) is perhaps among the most important recent advancements[22,23]: it is now currently possible to preserve cellular structures much

closer to their native states in preparation for imaging by rapidly freezing cells in amorphous ice, as opposed to resin-embedding and sectioning which has been known to introduce many imaging artifacts[24].

The implementation of EM nevertheless comes with several caveats of its own, a primary reason being that the available toolbox of chemical 'contrast agents' (i.e., chemical imaging tools which enhance differences in contrast) are relatively underdeveloped in comparison to FM and other bio-imaging modalities. Indeed, all biological imaging modalities face inherent problems associated with relative contrast, which is colloquially described in This Thesis as "The Contrast Problem[25]." *It is proposed that cNPs can alleviate The Contrast Problem in several imaging modalities - but most prominently EM*.

1.4 A physical basis for relative contrast

Contrast is the state of being strikingly different, and in images it derives from how detectors monitor differing interactions between incident energies (e.g., photons, neutrons, electrons, sound waves, etc.) and the sample regions they are bombarding. One can imagine how a relatively 'transparent' object might disrupt or absorb incident energy less than a comparatively 'opaque' object. If two objects in this context have sufficiently different transparency (and thus interact with incident energy differently at a physical level), then they may visually contrast from one-another enough to be strikingly distinct to an observer. On the other hand, objects with identical transparency levels which interact with incident energies similarly can be difficult or even impossible to distinguish from one another (**Figure 1.2**). This analogy can be extended to the building blocks of biological materials at tissue, cellular, molecular, and atomic scales.

1.5 The Contrast Problem

Biological building blocks are predominantly composed of relatively 'electron-light' (as opposed to 'electron-dense') atoms with low Z-numbers - namely carbon (C), hydrogen (H), nitrogen (N), and oxygen (O). Such low-Z atoms with minimal electron density are less likely to perturb incoming electrons

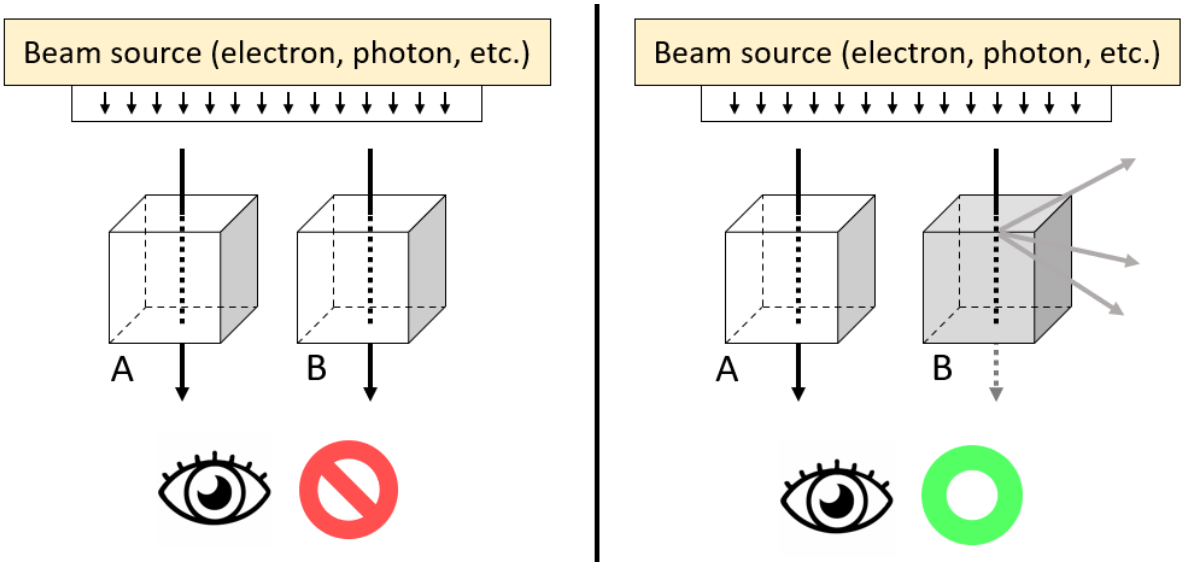

Figure 1.2: Depiction of how object (e.g., proteins) interactions with incident energy (e.g., electrons) dictates relative contrast. **Left panel**) A and B interact with incident energy similarly and are indistinguishable. **Right panel**) B deflects incident energy greater than A, and thus appears differently.

than high-Z elements, and the perturbed electrons are less likely to be done so with high magnitude. A major consequence of these physical interactions is that biological samples produce a low incidence rate of low-contrast events. Biological samples therefore have inherently low contrast under an electron microscope and thus require higher exposure times to achieve contrast that is meaningful for interpretation; extended exposures in parallel can condemn samples to degradation from high-energy electron bombardment within the timeframes they are subject to imaging[26].

To further exacerbate these issues, biological building blocks are relatively homogeneous in their atomic compositions; one protein will have a similar ratio of C, H, N, and O when compared to another and so forth among other classes of building blocks such as polynucleotides or lipids. Incident electrons thus interact with building blocks in a manner that is relatively similar across the near-infinite landscape of available atomic configurations, resulting in data outputs that are near-identical from one constituent (e.g., protein) to another. This results in the 'gears and levers' of intracellular machinery being essentially indistinguishable from another while also being nearly invisible within a complex cellular environment.

Thus, in order to have a better understanding of what is occurring at subcellular levels (such as visualizing how an individual protein can affect the structure of its surrounding environment), specialized chemical tools must be implemented to extend the limitations of what is observable given what instrumentation is available.

1.6 Chemical contrast agents

As opposed to the predominant biological atoms (namely C, H, O, and N), metals and metalloids possess atomic characteristics that are, generally speaking, comparatively denser in their electrical composition. From the viewpoint of an electron microscope, heavier metal(loid) atoms deflect and absorb electrons at significantly greater magnitudes than the low-Z atoms which comprise the greater makeup of biological matter. With such a sufficient difference in physical interaction, metal(loids) can heavily contrast from a surrounding environment of biological matter.

One may thus imagine how such highly contrasting metal(loid) elements can be advantageously used to selectively highlight certain regions within a cell which might otherwise be indistinguishable and simultaneously invisible[27,28]. Osmium tetroxide for instance, which preferentially adsorbs to nonpolar areas such as fatty membranes, is routinely used to 'stain' the lipid boundaries of cells and organelles such as mitochondria or nuclei[29]. On the other hand, uranyl acetate can bind sialic acid carboxyl groups such as those found in glycoproteins or nucleic acid phosphates. Chemicals such as these allow certain components of cellular ultrastructure to be 'stained' in manners that is modestly preferential; membranes, organelles, filamentous proteins, and other major structural features can be visualized, allowing their observation and interpretation.

As imaging technologies have progressed through time, more attention has been directed towards reductionist approaches of understanding cellular machinery. A growing number of modern microscopists wonder at how they can better understand the role of a single constituent (such as an individual protein) within its greater context. To better understand biological systems (e.g., single to multi

protein systems) at smaller and more discrete scales, improved contrasting 'markers' can be deposited with much greater proximal accuracy than non-, region- or tissue-specific stains such as osmium tetroxide or uranyl acetate.

1.7 Antibody based chemical contrast agents

Antibodies are large (100-150 kDa) proteins most commonly known for their binding activities towards specific antigens, which are generally small molecules or protein epitopes (but can encompass any chemical entity that is recognizable through protein interfaces found on antibodies). This relationship between antibodies and their specific antigens can be used advantageously to deliver 'pinpoint' contrast markers to targets-of-interest in a specific manner. Contrasting tags (such as commonly used colloidal gold nanoparticles in EM[30,31] or fluorophores in FM) can be tethered to antibodies that have specific binding activity towards antigens-of-interest, resulting in proximal correlations of contrast agents to respective instances of target antigens (which in an imaging context are components that are being studied directly or are otherwise related to systems of interest.) The end result is that relatively indistinguishable and invisible subcellular components such as individual proteins can effectively be 'highlighted' in comparison to their background[32].

While immune labels remain ubiquitous in modern biological EM studies, their limitations are widely recognized and are a persistent source of adversity for cellular microscopists[33]. To better understand these limitations, one must consider the different workflows of preparation for cellular samples.

Given the low depth that EM can penetrate through tissue (and its destructivity), cellular samples have historically been sectioned into ultrathin layers (~100 nm depth) using a microtome. To avoid introducing artifacts in the sectioning process from shear forces, cells may first be chemically fixed then embedded into organic resins. Labeling with antibodies occurs before or after the fixation and embedding processes. Pre-fixation labeling of intramembranous (i.e., intracellular or within organelles) targets

requires highly perturbing pore formation along membranes to allow the passage of large (5-10 nm diameter) antibodies, which greatly disrupts native structure. On the other hand, antibodies are diffusion-limited in post-fixed and resin-embedded sectioned microtomes, thus biasing their labeling recognition to epitopes that are exposed along microtome surface edges. The delivery issue is more profound in Cryo-EM, where samples are not usually sectioned or perforated prior to imaging. The generally implemented use of primary and secondary antibody systems moreover positions contrasting markers distally (up to 10 nm) to targets of interest, diminishing the theoretical advantages of high resolution offered by EM. Finally, antibodies can bind off-target antigens, may have limited storage stability, and can otherwise be inconsistent from batch-to-batch due to post-translational modifications[34].

1.8 Cloneable contrast agents

A solution to the delivery problem of interaction-based contrast enhancers (such as antibodies) towards proteins-of-interest (and potentially other biomolecules) can be found through 'cloneable tags' (**Figure 1.3**). Cloneable tags are elements of DNA whose expression results in an instance of a contrast marker. As the resulting contrast tags are encoded in genetic material, they are cloneable in the same way as any other gene and therefore need not be exogenously delivered into the cell, a process which significantly disrupts cellular architecture. To specifically label a protein of interest (POI), one can append the DNA of a cloneable tag directly to the DNA of the POI. Thus, excellent preservation of cellular structure can be attained along with near-perfect labeling efficiency, as there is no need to permeabilize membranes or diffuse antibodies through resin.

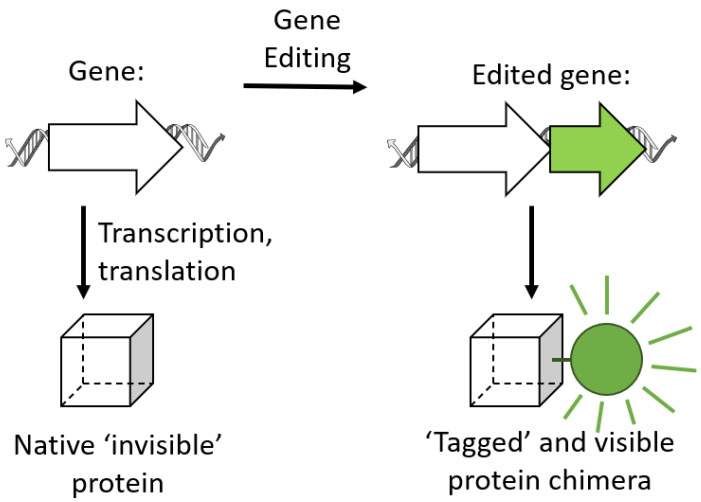

Figure 1.3 – Cloneable contrast agents: DNA encoding a gene whose expression encodes a contrasting protein signal (e.g., fluorescence or electron density) is appended to an otherwise invisible gene of interest.

Nevertheless, there is still a gap in developing protein tags that can generate sufficient electron density at the tag site to allow its detection in EM, as the density of a protein alone is not sufficient to unambiguously identify within a complex cellular environment. In recent years, there have been attempts to address this gap and generate cellular EM genetic tags. The most established forms of cloneable tags in EM are enzymes that can locally deposit osmiophilic diaminobenzidine (DAB), such as mini singlet-oxygen generator[35] (miniSOG) and engineered ascorbate peroxidase[36] (APEX2). While highly sensitive, DAB-based contrast is also highly diffuse, with contrasting markers diffusing distally (dozens to hundreds of nm) away from their points of origination. Other approaches include using metallothioneins[37] which are small (~7 kDa) thiol-rich proteins that can stoichiometrically bind ~20 metal atoms, or ferritins which are massive (~0.4 MDa) multi-proteins systems within which several thousand iron atoms can be sequestered[38]. Metallothioneins are difficult to visualize due to their low amount of metal atoms (and thus low contrast), whereas ferritins are excessively large (thus hindering POI diffusion/function) and cast shadow over their background context. These methods and their strengths and weaknesses will be discussed in greater detail in Chapter 4.

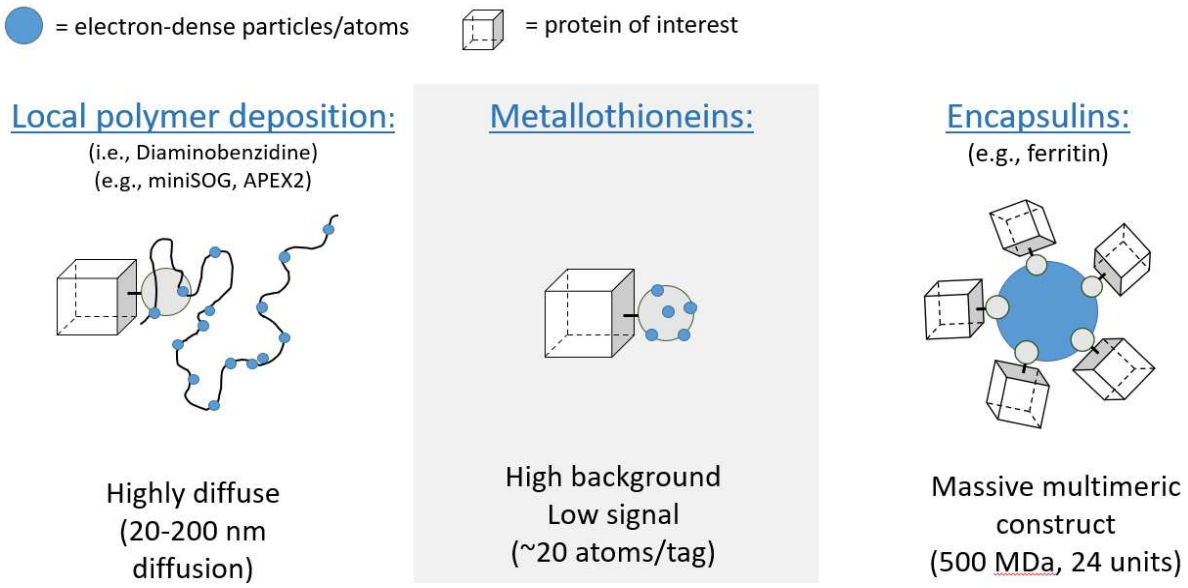

Figure 1.4: Current cloneable EM contrast agents being explored. **Left)** DAB polymerizers diffuse distally to the point of origin, **Middle)** Metallothioneins provide minimal contrast with stoichiometric quantities of metal atoms, **Right)** Encapsulins are massive multimeric constructs which convolute imaging studies.

1.9 Cloneable Nanoparticles are proposed as more effective cloneable contrast tags

Cloneable Nanoparticles (cNPs) represent a cloneable method of replicating inorganic nanoparticles, much in the same way that a protein can be cloned into other organisms (Figure 1.5). In the context of the Ackerson Research Group, our work on cNPs predominantly focuses on their implementation towards addressing The Contrast Problem in biological imaging[25]. We hypothesize that cNPs will overcome the inherent limitations of other cloneable contrast agents used in EM, and that cNPs equivalently can be implemented in other imaging modalities such as computer tomography.

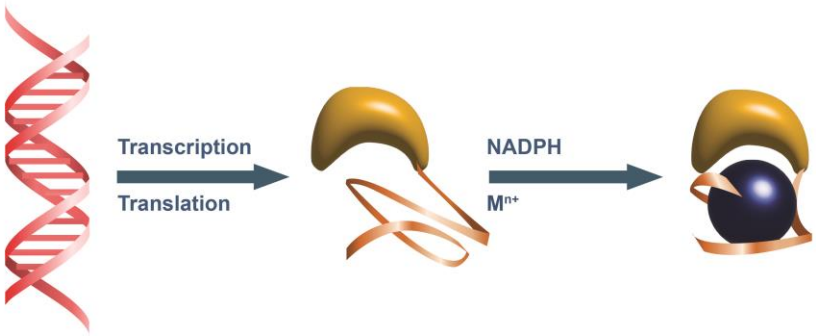

Figure 1.5 Scheme depicting a cloneable nanoparticle. DNA is transcribed into RNA, then translated into enzyme. The enzyme then generates and retains a size-controlled inorganic nanoparticle. *Adapted with permission from Charleston Ducote*.

CHAPTER 2: IDENTIFICATION OF A TeO_3^{2-} REDUCTASE/MYCOTHIONE REDUCTASE FROM *RHODOCOCCUS ERYTHROPOLIS PR4*

2.1 Introduction

Cellular resistance to toxic metal ions manifests through several pathways typically involving ion sequestration, the conversion of biologically active soluble species to less active insoluble materials, volatilization or adaptive regulation of ion transportation[39–47]. These pathways typically operate through multiple protein cascades wherein toxins are processed in a stepwise manner. However, in several instances discrete enzymes have demonstrated independent activity towards metals leading to improved cell survivability in challenged environments. Cysteine-rich metallothioneins have been identified for their role in metal sequestration[48–53]. Cystathionine- γ -lyase is capable of extracting a sulfur group from cysteine which is capable of binding and precipitating Cd^{2+}[54,55]. Mercuric Reductase (MerA) has been identified in the reduction of Hg(II) to elemental Hg which rapidly volatilizes[56–58]. Dihydrolipoamide dehydrogenase, nitrate reductase and catalase have demonstrated reducing activity towards selenite, selenate, tellurite and tellurate to form less toxic inorganic precipitates[59–62]. Chromate reductase is responsible for the reduction of labile and toxic Cr(VI) to less bio-active Cr(III), although no precipitate is formed in this instance[63]. In current literature there are more documented examples of organisms and specific enzymes capable of performing Se-reduction with respect to other metal and metalloid species[42,64–66].

Tellurium specialized microorganisms have been previously described. In general, zerovalent tellurium is much less toxic than tellurite, so reduction of tellurite is a common strategy for tellurite tolerance[67]. Several organisms have been described that reduce tellurite, with intracellular Te nanorods observed in *Rhodococcus aetherivorans* and *Rhodobacter capsulatus*[68,69]. Three distinct tellurite reductases have been identified from three different species[70–73]. While some enzymes are observed for

preferring tellurite substrates over selenite substrates, the molecular mechanism for distinguishing among substrates is obscure.

The identification of additional enzymes and enzymatic pathways for metal oxidation and reduction is of both fundamental and applied interest. Fundamentally, the metabolism of metals is incompletely understood, especially those metals that are non-essential and even toxic. The enzymes and enzymatic pathways revealed in fundamental studies may be subsequently adapted for bio-remediation of areas of metal contamination, and also possibly as reporter genes, producing nanoparticles that impart contrast in imaging modalities such as electron microscopy and x-ray imaging[68].

Herein, we report the identification and characterization of a mycothione reductase specialized for Tellurite reduction. This enzyme is found in an environmental isolate identified as *Rhodococcus erythropolis* PR4 that was cultured from mine site seepage in the Colorado Mining Belt. Cultured *R. erythropolis* PR4 showed high resistance to several metal ion species, including typically toxic concentrations of Fe(II), Cu(II), AsO3 2−, SeO_3^{2-}, TeO_3^{2-}, Cd(II) and Zn(II). Upon screening of lysate from *R. erythropolis* PR4, a mycothione reductase homolog was isolated possessing selective NADPH-dependent reductase activity towards TeO_3^{2-} to form Te^0 nanoparticulate. The isolated mycothione reductase homolog (Mtr) showed high reduction specificity towards Te-based substrates compared to Se-based substrates. This is a surprising finding on the basis of reduction potentials for the two substrates. The standard reduction of potential for the reaction TeO_3^{2-} + 3 H_2O + $4e^-$ ← → Te + 6 OH^- is −0.57 V vs Hydrogen. The corresponding reduction of SeO_3^{2-} is −0.366 V. Thus, SeO_3^{2-} is the preferred substrate for reduction in the absence of a mechanism for substrate selectivity.

2.2 Results and Discussion

2.2.1 *Identification and selectivity of a Te-reductase*

The Mtr enzyme was isolated from an environmental *R. erythropolis* isolate. The bacterium was found in multiple metal contaminated mine runoff in Clear Creek County, Colorado. This is a county in the

Colorado Mineral Belt that contains over 1500 abandoned mine sites dating to the 1851 Colorado Gold Rush. More information on this can be found in the Supplemental Information. *Rhodococcus erythopolis* PR4 was of interest because of its tolerance to ordinarily lethal concentrations of Fe(II), Cu(II), AsO_3^{2-}, SeO_3^{2-}, TeO_3^{2-}, Cd(II) and Zn(II). Full data on the metal tolerance of this isolate, including minimum inhibitory concentrations (MIC) can be found in Figure S1 and Table S1 (Supporting Information). Of note, the MIC for TeO_3^{2-} was found as 4.5mM.

Initial identification of Mtr as a TeO_3^{2-} reducing enzyme was in a previously reported in-situ screen developed for identifying metal-reducing enzymes[68]. Briefly, in a non-denaturing-PAGE, all soluble lysate proteins from *R. erythropolis* PR4 were fractionated. The gel was then incubated in metal salts and enzyme cofactors. Visible bands in the gel are attributed to enzymatic reduction of metal salts to nanoparticulate form. Since *R. erythropolis* PR4 exhibits tolerance to several metal salts, we opted to vertically section native-PAGE gels and expose them to 5 mM concentrations of K_2TeO_3, $HNaSeO_3$, $CuCl_2$, $ZnCl_2$ and $FeCl_2$. Each in-situ reaction was supplemented with either NADPH or NADH, since many known metal oxidoreductases depend on these biological electron sources.

We observed a single band develop when incubated in TeO_3^{2-} and NADPH (**Figure 2.1A**). This was surprising given that no band developed with SeO_3^{2-}, a chemically similar chalcogen oxyanion that has a redox potential 0.2 V more positive[74]. Another band was observed when a gel was incubated with TeO_3^{2-} and NADH although to a far lesser extent indicating the enzyme was preferential to NADPH as the cofactor. Bands were not observed when cofactors were omitted from the assay.

Excision of the bands, followed by proteolytic digestion and LC-MS/MS, led to identification of 13 proteins which are listed in **Figure 2.1B**. Of those 13 identified proteins, five possessed NAD(P)H binding domains. We focused initial characterization on the mycothione reductase identified in this screen, due to its functional homology (metalloid reduction) to a Glutathione Reductase-like Metalloid Reductase

A.

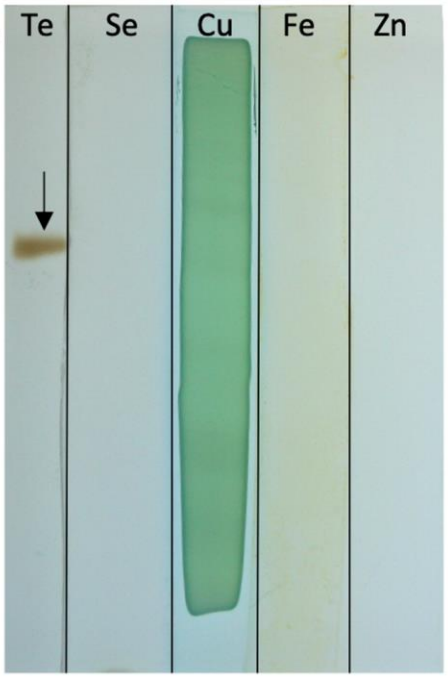

B.

MS Identified Proteins	M_W
Putrescine Oxidase	*49 kDa*
β-ketoadipyl-CoA Thiolase	42 kDa
Mycothione Reductase	*49 kDa*
Malate Dehydrogenase	*41 kDa*
Aminopeptidase N	91 kDa
Superoxide Dismutase	23 kDa
Enoyl-CoA Hydratase	27 kDa
Thioredoxin Reductase	*35 kDa*
3-hydroxyisobutyrate Dehydrogenase	*30 kDa*
RNA Polymerase Subunit α	38 kDa
Zinc-Dependent Metalloprotease	50 kDa
Metallo-hydrolase	48 kDa
Phosphoenolpyruvate Carboxykinase	67 kDa

Figure 2.1. (**A**) Native-PAGE gel sections incubated in indicated metal/loid ions and NADPH. The arrow indicates reduced insoluble Te^0 particulate. Cu(II) was precipitated in gel with and without protein. (**B**) Proteins associated with the excised Te^0 by LC-MS/MS. Entries in italics indicate the presence of an NAD(P)H binding domain.

(GRLMR) we previously identified from the most Se tolerant organism described to date[25,75].

Mtr was initially amplified by PCR from the genome of *R. erythropolis* PR4. Primers were based upon the known genomic sequence of *R. erythropolis* PR4, which was initially isolated south of Okinawa Island, Japan in the Pacific Ocean[76,77]. The gene was then inserted into an expression vector from ATUM, p-D441CH plasmid possessing a C-terminal His tag and Kanamycin resistance. Mtr was expressed in T7 Express *E. coli* (C2566I) from New England Biolabs (NEB). Expression was confirmed in the soluble lysate after induction for several hours using SDS-PAGE. Mtr was then isolated using a 5 mL HisTrap Fast Flow column and further purified on a 5 mL HiTrap DEAE Fast Flow column. Purity of Mtr was determined on SDS-PAGE, shown in Appendix A.

Specificity of Mtr for TeO_3^{2-} reduction over SeO_3^{2-} reduction was established by assaying the elemental ratio of Te: Se in the reaction product of reactions performed in mixtures of TeO_3^{2-} and SeO_3^{2-}.

Experiments with equimolar amounts of TeO_3^{2-} and SeO_3^{2-} were tested, as well as 5- and 10-fold excesses of SeO_3^{2-}. The ratio of Te to Se in each insoluble reaction product was established by ICP-MS. **Figure 2.2** illustrates that Te content dominates enzymatic products when both TeO_3^{2-} and SeO_3^{2-} are simultaneously available as reactants. At equimolar reactant concentrations, over 6 times more Te than Se is found in the enzymatic product. When Se is present in a 5-fold molar excess, Te is still found in the enzymatic product at 2.5-fold excess to Se. Even when Se is in 10-fold excess to Te, the resulting insoluble fraction still possessed more Te. Combined, these experiments show Mtr exhibits a strong substrate preference for TeO_3^{2-} over SeO_3^{2-}.

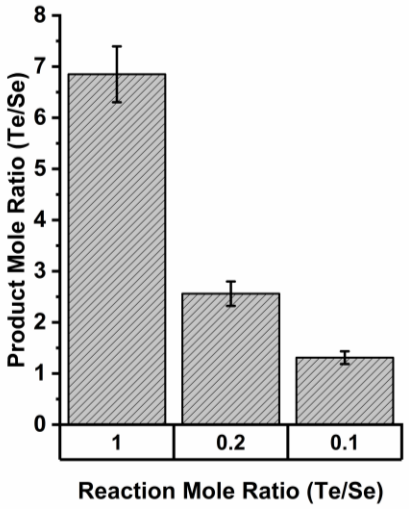

Figure 2.2. Elemental composition of precipitates resulting from enzymatic reactions in indicated ratios of TeO_3^{2-} and SeO_3^{2-}, as determined by ICP-MS. All reactions were performed with 500 µM NADPH.

2.2.2 *Kinetics study of Te-reducing Mtr*

The enzyme was further characterized for its kinetic rate with substrates TeO_3^{2-} and SeO_3^{2-}. Reduction experiments were performed in PBS, 20 mM TEA, and 20 mM HEPES pHs 6–9 to test effects of varying buffers and pH ranges with respect to enzyme kinetics. The enzyme kinetics were established by monitoring the loss of the NADPH substrate spectrophotometrically. This substrate absorbs distinctly at 340 nm, and the corresponding product (NADP+) does not. Substrates tested were 2 mM starting

concentrations of SeO_3^{2-}, TeO_3^{2-} and initial velocities were determined through monitoring the degradation of 200 µM NADPH at 340 nm.

Initial kinetic rates of the enzyme toward each reactant in PBS, HEPES and Triethyl Amine (TEA) buffers, with pH adjusted to values in between 6 and 9. Initial kinetic rates were essentially buffer-independent; The initial rates of reaction in PBS for each substrate at varying pH values are shown in **Figure 2.3**. This pH screen shows that the reduction of TeO_3^{2-} is substantially faster than the reduction of SeO_3^{2-}, independent of pH. Results for HEPES and Triethylamine (TEA) buffers are shown in Appendix A.

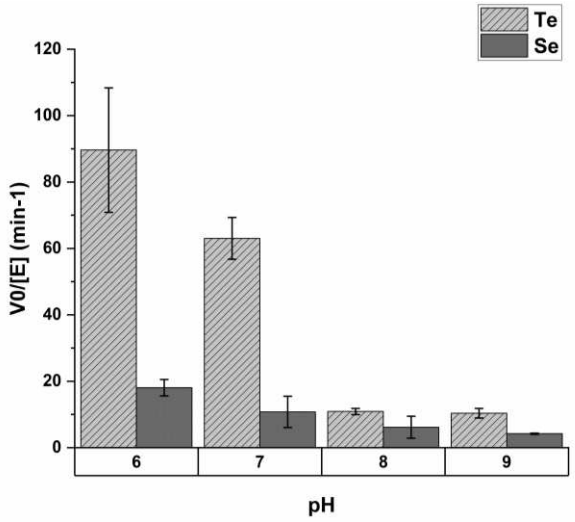

Figure 2.3. A screen for how reaction pH effects Mtr substrate selectivity, using PBS buffer. The y-axis indicates initial velocities for Mtr with substrates TeO_3^{2-} and SeO_3^{2-}. Each substrate was present at 2 mM. The pH screen suggests that selectivity decreases as pH increases.

The K_m and k_{cat} of Mtr were also calculated using initial velocities of Mtr with a range of 0.5– 10 mM of either TeO_3^{2-} or SeO_3^{2-} in PBS (pH 7.4), 20 mM TEA-HCl (pH 7.6) and 20 mM HEPES (pH 7.0). Plots of the V_0 at varying substrate concentrations for HEPES buffered reactions are shown in **Figure 2.4** and the calculated values shown in **Table 2.1**. In all buffers tested, Mtr possessed a more favorable K_m for TeO_3^{2-} compared to SeO_3^{2-}. The catalytic efficiency (k_{cat}/K_m) is 10-fold higher for TeO_3^{2-} over SeO_3^{2-}. We note that we did not find a substrate concentration of SeO_3^{2-} that achieves a steady-state reaction

(**Figure 2.4**), allowing an accurate determination of enzymatic Vmax for this substrate. This may impact the accuracy of the Michaelis–Menten kinetic fit. However, this difficulty in observing Vmax for SeO_3^{2-} substrates is a further indication of the adaptation of this enzyme for TeO_3^{2-}. Indeed, the highest concentrations of SeO_3^{2-} tested (40mM) are decidedly nonphysiological. To emphasize this point, we found an MIC of 2.5mM SeO_3^{2-} for this microbe.

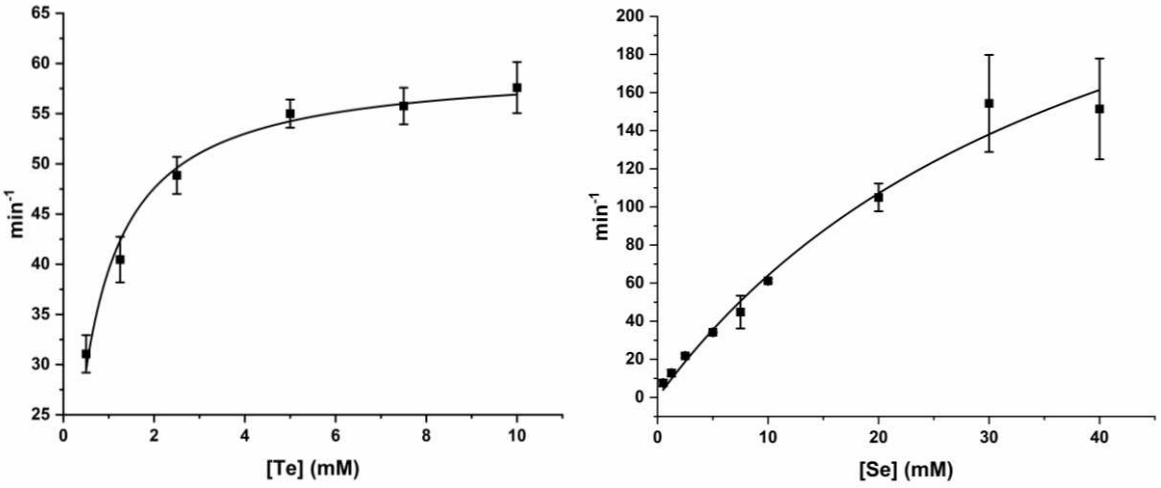

Figure 2.4. Plots of enzymatic rate (min^{-1}) v. substrate concentration (mM) for Mtr. Solutions were buffered in HEPES, pH 7.4, Substrates were either TeO_3^{2-} or SeO_3^{2-}, as indicated on each plot.

When examining the activity of the enzyme toward different substrates, we calculate that that the activity of the enzyme is higher for TeO_3^{2-} than SeO_3^{2-} for all substrate concentrations tested that were 5 mM or less. For instance, in HEPES buffer at 5 mM substrate concentration, we calculate the activity of the enzyme as 1095.8 ± 34.6 µmol NADPH consumed per minute per mg of enzyme (µmol in g)

Table 2.1. Kinetics data for Mtr.

	20 mM HEPES, pH 7		20 mM TEA-HCl, pH 7.6		PBS, pH 7.4	
	TeO_3^{2-}	SeO_3^{2-}	TeO_3^{2-}	SeO_3^{2-}	TeO_3^{2-}	SeO_3^{2-}
K_m (mM)	0.517 ± 0.005	41.41 ± 11.69	0.779 ± 0.050	35.23 ± 4.51	0.413 ± 0.141	43.9 ± 14.7
k_{cat} (min^{-1})	59.8 ± 1.07	327.4 ± 56.7	88.6 ± 5.40	497.1 ± 36.9	11.9 ± 0.68	215.8 ± 44.9
k_{cat}/K_m	16 ± 11.4	7.9 ± 2.65	14 ± 10.4	14.1 ± 2.09	28.9 ± 9.99	4.9 ± 1.94

for TeO_3^{2-}, whereas this value is calculated as 680.7 ± 6.50 µmol NADPH /mn /m of enzyme for SeO_3^{2-}.

Initial kinetics studies (**Figure 2.3**) suggested that selectivity for Te over Se may diminish at higher pH. Because this observation has implications for the mechanism of selectivity, we compared relative amounts of Mtr reduction product when equimolar concentrations of TeO_3^{2-} and SeO_3^{2-} were present as equimolar reactants. **Figure 2.5** depicts the relative molar product ratios of Te and Se as determined by ICP-MS. This experiment confirms that selectivity of the enzyme for TeO_3^{2-} over SeO_3^{2-} diminishes as pH increases. This diminishment of selectivity at higher pH implicates the protonation state of residues near the active site in substrate selectivity.

2.2.3 *A structural basis for Te selectivity*

A homology model for the structures of Mtr and GRLMR were generated with Phyre2[78]. The most similar empirical structure used in the homology model is the mycothione reductase from Mycobacterium tuberculosis which is 65.64% similar[79–81]. 3D structural alignment to GRLMR in in Pymol[78] was used to identify the putative active site of Mtr. The active site of GRLMR and related glutathione reductases can be defined by a pair of redox-active putatively catalytic cysteine residues.

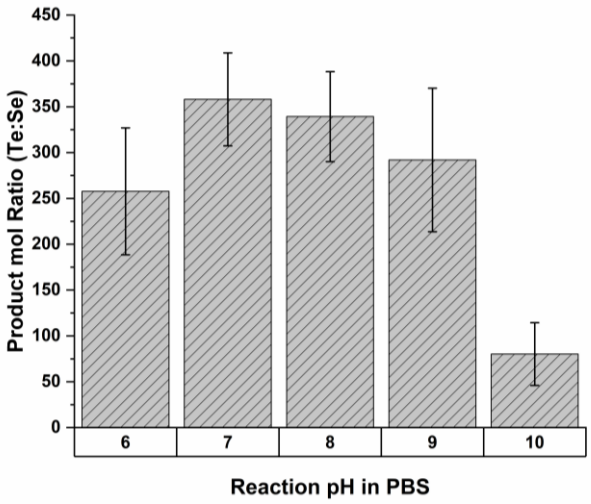

Figure 2.5. Ratio of Te: Se in enzymatic products, as determined by ICP-MS for reactions performed at pH values between 6 and 9.

An examination of both structures reveals several mutations near the active site. These are T259V, T339A, G203H, Y175F K49T, R305Y, P310H and V434I, **Figure 2.6** shows the active site of both the Selenite selective GRLMR and the Tellurite selective Mtr. What is apparent in examining these active sites is the abundance of aromatic residues in Mtr that are absent in GRLMR. For Mtr, these residues include Y307, H311, F178 and H206. In contrast, GRLMR contains no aromatic residues in or near its active site. Indeed the aromatic residues and the larger size (to accommodate a larger substrate) in Mtr are the chief differences between the two active sites.

Within the chalcogens, π-interaction potential decreases going towards heavier elements, S > Se > Te[82]. The residues H206 and Y307 are predicted as pointing towards the opening and could be involved in substrate interactions that are more favorable for TeO_3^{2-} as compared to SeO_3^{2-}, due to the more favorable π-interactions with Te. The pH dependence of selectivity further implicates H206 and possibly H311 in selectivity for Te over Se, as these residues are protonated at lower pH and deprotonated at higher pH.

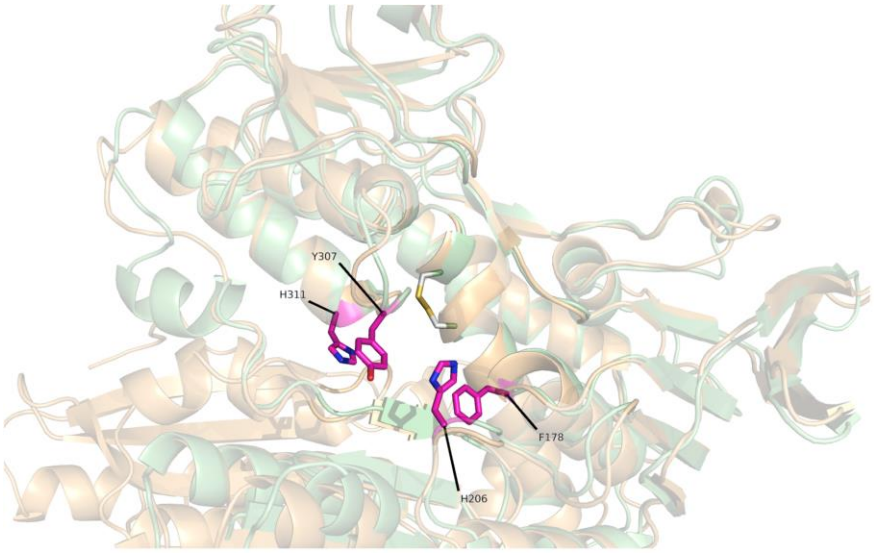

Figure 2.6. Homology models of Mtr and GRLMR shown as an overlay of each structure. The active-site cysteine residues are shown in brown (carbon) and yellow (cysteine). Aromatic residues in the active site cavity and within 15 A of the active ˚ site that are present in Mtr but not in GRLMR are shown in Magenta.

2.2.4 *Mtr mediated Te-nanostructures*

The Mtr reaction product from TeO_3^{2-} substrates is solid-phase Te^0. Examination of the Te^0 by electron microscopy (EM) reveals nanoparticles and nanostructures of distinct morphology. The size and shape of these Te nanoparticles or nanostructured Te depends sensitively on the concentration of TeO_3^{2-} substrate. Concentrations of 1, 3, and 7 mM of K_2TeO_3 with excess of NADPH were reduced in the presence of 15 µg of Mtr. Reactions proceeded for 16 h and the resulting Te^0 nanostructures were imaged by Scanning Electron Microscopy (SEM). In 1 mM TeO_3^{2-} reactions, the product is a prolate ellipsoid of approximately 50 nm in the axial dimension (**Figure 2.7A**). In 5 mM TeO_3^{2-}, the reaction products resemble bundled Te nanowires (**Figure 2.7B**). In 7 mM TeO_3^{2-}, the resulting nanostructure appears as a fractal-like deposit composed of large aggregates of fused nanowire bundles (**Figure 2.7C**). Te-nanostructures observed in vitro also corresponded well with the structures observed in *R. erythropolis* PR4 when incubated with K_2TeO_3 (Figure S2, Supporting Information).

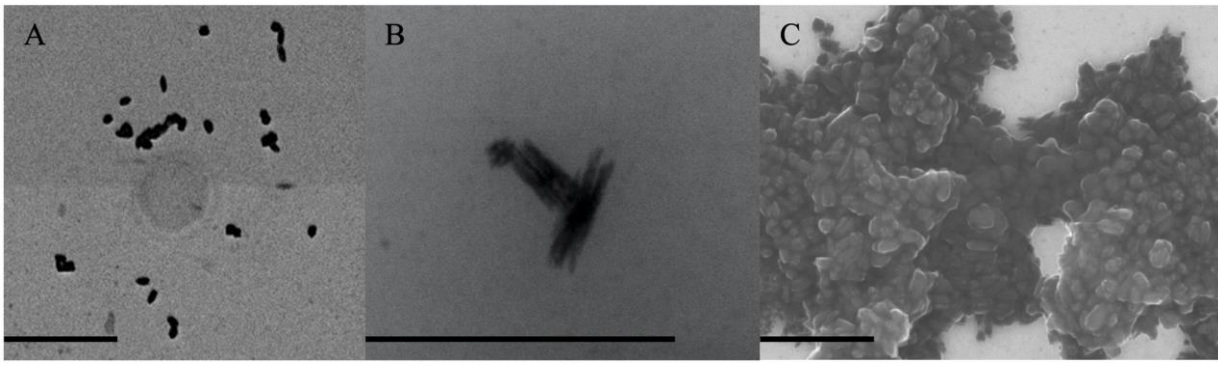

Figure 2.7. Scanning electron micrographs of Te-nanostructures produced by Mtr with substrate concentrations of (**A**) 1 mM, (**B**) 3 mM and (**C**) 7 mM K_2TeO_3. Scale bar in each image is 500 nm.

The growth of Te nanowires from amorphous Te, as we observe in this work, is previously described by others in abiotic synthesis. The formation of nanowires from amorphous Te results from the high surface energy of amorphous Te, which rearranges spontaneously to trigonal Te nanorods. The conversion from amorphous to trigonal Te is slow at room temperature. The trigonal Te nanorods then grow perpendicular to the [001] plane[83–85].

2.3 Summary and Conclusion

Microorganisms isolated from metal contaminated mine runoff in the Colorado Mining Belt have provided several opportunities to study enzymes that enable cell survival in a wide range of toxic metal salts. Screening of cell lysates identified a Te reducing mycothione reductase identified from *R. erythropolis* PR4. Mtr has notable selectivity for tellurite reduction over selenite reduction, which we attribute to the presence of aromatic residues near the active site.

2.4 Materials and Methods

Materials PCR and ligation components, restriction enzymes and T7 Expression lysY/Iq Competent E. coli cells (Cat # C3013I) were purchased from New England Biolabs, Inc. (Ipswitch, MA) Primers were purchased from Integrated DNA Technologies (Coralville, IA). The expression vector pD441-CH was originally purchased from ATUM (DNA Twopointo Inc., Newark, CA). Antibiotics were purchased from GoldBio (St. Louis, MO). Na_2SeO_3, $HNaSeO_3$ and K_2TeO_3 were purchased from Alfa Aesar (Stoughton,

MA). NADPH was purchased from BioVision (Milpitas, CA) and Coomassie Plus Bradford Reagent from Thermo Scientific (Coon Rapids, MN). GTP was purchased from Chem-Impex Int'l Inc. (Wood Dale, IL) GeneJet Plasmid Miniprep Kit (Cat# K0503) and PCR Cleanup Kit (Cat# K0702) were purchased from ThermoFisher Scientific (Waltham, MA).

2.4.1 *Metal Screening of Lysates*

Lysate metal screens were then conducted to try and identify specific enzymes responsible for the reduction of the metals tested. A total of 25 mL cultures of the environmental isolates were grown to density, cells were collected and lysed using intense agitation with glass beads. Lysate was collected and run in a native-PAGE gel for crude separation of the lysate. The PAGE gel was then cut into vertical strips and incubated in 50 mM HEPES buffer with 5 mM of a metal salt and either NADPH or NADH as a cofactor. Reactions were run in an inert atmosphere and the next day, gels were observed for possible metal band development, indicating metal salt reduction. Corresponding bands in the gel were then excised and sent for LC-MS/MS.

2.4.2 *LC-MS/MS Sample Preparation*

Gel fragments were subjected to in-gel trypsin digestion and LC-MS/MS as previously described[86]. Briefly, the gel pieces were washed with 200 µL of LC-MS Grade Water (Optima LC-MS, Fisher Scientific, Pittsburgh, PA) for 30 s and destained with 2 × 200 µL of 50% Acetonitrile (ACN; Optima LCMS Grade)/50 mM Ammonium bicarbonate at 60◦C, with intermittent mixing. The pieces were dehydrated with 100% ACN and allowed to air dry. Proteins were reduced and alkylated, in-gel with 25 mM DTT in 50 mM ammonium bicarbonate (60◦C for 20 min) and 55 mM IAA or IAH in 50 mM ammonium bicarbonate at room temperature in the dark for 20 min. Gel pieces were then washed with Optima water and dried. The dried gel pieces were rehydrated in 20 µL 12 ng/µL MS-grade Trypsin (ThermoPierce, San Jose, CA)/0.01% ProteaseMAX surfactant/50 mM ammonium bicarbonate mixture for 10 min at room temperature, overlaid with 30 µL 0.01% ProteaseMAX surfactant/50 mM ammonium bicarbonate and incubated at 50◦C

for 1 h. Extracted peptides were transferred and the digestion halted by addition of 10% trifluoro-acetic acid to a final concentration of 0.5%. Peptide extracts were dehydrated then resuspended in 5% ACN/0.1% formic acid. Once resolubilized, absorbance at 205 nm was measured on a NanoDrop (ThermoScientific, Coon Rapids, MN) and total peptide concentration was subsequently calculated using an extinction coefficient of 31[87].

2.4.3 *LC-MS/MS mass spectrometry analysis*

A total of 1 µg of peptides were purified and concentrated using an on-line enrichment column (Thermo Scientific 5 µm, 100 µm ID x 2 cm C18 column). Subsequent chromatographic separation was performed on a reverse phase nanospray column (Thermo Scientific EASYnano-LC, 3 µm, 75 µm ID x 100 mm C18 column) using a 30-min linear gradient from 5 to 30% buffer B (100% ACN, 0.1% formic acid) at a flow rate of 400 nL/min. Peptides were eluted directly into the mass spectrometer (Orbitrap Velos, Thermo Scientific) equipped with a Nanospray Flex ion source (Thermo Scientific) and spectra were collected over a m/z range of 400–2000, positive mode ionization, using a dynamic exclusion limit of 2 MS/MS spectra of a given m/z value for 30 s (exclusion duration of 90 s). The instrument was operated in FT mode for MS detection (resolution of 60 000) and ion trap mode for MS/MS detection with a normalized collision energy set to 35%. Compound lists of the resulting spectra were generated using Xcalibur 3.0 software (Thermo Scientific) with a S/N threshold of 1.5 and 1 scan/group.

2.4.4 *LC-MS/MS data analysis*

Tandem mass spectra were extracted, charge state deconvoluted and deisotoped by ProteoWizard MsConvert (version 3.0). Spectra from all samples were searched using Mascot (Matrix Science, London, UK; version 2.3.01) against the customized Uniprot Ecoli rev 08 2416 database (unknown version, 8630 entries) assuming the digestion enzyme trypsin. Mascot was searched with a fragment ion mass tolerance of 0.80 Da and a parent ion tolerance of 20 PPM. Oxidation of methionine, carbamidomethyl of cysteine and carboxymethyl of cysteine were specified in Mascot as variable

modifications. Search results from all samples were imported and combined using the probabilistic protein identification algorithms implemented in the Scaffold software[88,89] (version Scaffold 4.5.1, Proteome Software Inc., Portland, OR). The peptide threshold (95%) was set such that a peptide FDR of 0.0% was achieved based on hits to the reverse database[90]. Protein identifications were accepted if they could be established at greater than 95.0% probability and contained at least two identified peptides. Protein probabilities were assigned by the Protein Prophet algorithm[91]. Proteins that contained similar peptides and could not be differentiated based on MS/MS analysis alone were grouped to satisfy the principles of parsimony.

2.4.5 *Plasmid construction*

Colony PCR (cPCR) was used to amplify the gene for all the NADPH-dependent proteins that resulted from LC-MS/MS. Briefly, gene sequences were identified using an amino acid sequence BLAST against the genome and three plasmids of *R. erythropolis* PR4. Sequences then directed the design of primers that would be used for gene amplification. PCR reactions were then set up as follows, 100 nM final concentration of each primer, 200 µM dNTPs, 10 µL of Q5 buffer, 10 µL of GC Enhancer, 1U of NEB's Q5 High-Fidelity Polymerase were brought up to 50 µL with milli-Q water. To each PCR reaction tube, an aliquot of *R. erythropolis* was added to provide a genomic template for the reaction. Denaturing of the template occurred at 98◦C for 2 min followed by 37 cycles of a 10 s denaturing at 98◦C, 65◦C for 20 s and extension at 72◦C for 2 min and 45 s. A final 2 min extension at 72◦C to finish any incomplete extensions. PCR product was cleaned using the Thermo Gene-jet PCR purification kit and eluted with 50 µL of milli-Q water for future digestion and ligation. 1 µg of PCR product was then digested at 50◦C for at least 1 h using 10 U of corresponding restriction enzyme, 5 µL corresponding NEB Buffer and a final volume of 50 µL using milliQ water. The restriction digestion was again cleaned using the Thermo purification kit and eluted using 40 µL of milli-Q water. Insertion of the genes into the expression vector pD441-CH with a C-terminal

His-tag purchased originally from ATUM were performed using T4 Ligase and resulting plasmids were transformed into BL21(DE3) cells for protein isolation. Gene insertion was confirmed through sequencing.

2.4.6 *Mycothione reductase Isolation*

A started culture of BL21(DE3) containing Mtr with a C-terminal His tag was grown overnight at 37◦C and 225 RPM. The next day a 1.2 L LB growth flask supplemented with chloramphenicol and kanamycin was inoculated with the starter culture and grown until an OD600 ∼0.5 at which time the culture was induced using 500 µM IPTG and grown at ∼30◦C overnight in aerobic conditions. The next day cells were collected, resuspended in 20 mM TEA-HCl, pH 7.6 and lysed on ice using sonication. Insoluble material was removed through centrifugation and the resulting lysate, which was red in color due to the presence of concentrated Mtr. Fast Protein Liquid Chromatography (FPLC) was then used for initial isolation of Mtr using a Ni-NTA column. Briefly, a HisTrap FF column was equilibrated with TEA-HCl, pH 7.6, 2.5 mM imidazole. Lysate was then loaded on the column for 30 min mL/min. Once lysate was loaded onto the column a gradient from 2.5 mM imidazole to 150 mM imidazole over 60 min at 5 mL/min. Fractions were collected every minute and the presence of Mtr was indicated by a bright yellow color. These fractions were then combined and run on a HiTrap DEAE FF column to further isolate Mtr using a gradient from 0 to 500 mM NaCl over 60 min. Mtr, an enzyme with a pI of 5.1 was eluted from the DEAE column above 400 mM NaCl. Protein purification was checked using PAGE gel analysis.

2.4.7 *Kinetics studies*

Reduction reactions were performed using 15 µg of Mtr in either 20 mM HEPES pH 7.0, 20 mM TEA-HCl pH 7.6, or PBS pH 7.4. Alternatively, pH of each buffered solution was adjusted to pH 6.0, 7.0, 8.0 or 9.0 with HCl or NaOH as appropriate. Varying concentrations of K_2TeO_3, or $HNaSeO_3$, were added to the reaction and final volumes were brought to 1.0 mL. Reactions were then initiated by the addition of 200 µM NADPH. The oxidation of NADPH corresponding with the decrease in absorbance at 340 nm was correlated to the activity of the enzyme reaction velocity. At pH 6 and 7, the solubility of TeO_3^{2-} diminished

(insoluble precipitates formed), although this does not appear to impact enzyme function. Kinetic data was fit with the Michaelis–Menten model in Origin (Northampton, MA, originlab.com).

2.4.8 *Scanning electron microscopy*

Samples for SEM were prepared by the following: 15 µg of Mtr and 1.0, 3.0 or 7.0 mM K_2TeO_3 brought to 1 mL PBS pH 7.4. Reactions initiated with an excess amount of NADPH and run overnight at room temperature. The next day, aliquots (4 µL) were deposited on C-coated Cu TEM grids and imaged using a JEOL JSM-6500-F Scanning Electron Microscope at an accelerating voltage of 15 kV.

2.4.9 *ICP-MS*

Mtr (50 µg), 1 mM K_2TeO_3 and either 1, 5 or 10 mM $HNaSeO_3$ were combined in PBS pH 7.4. Reactions were initiated with 500 µM of NADPH and brought to a final volume of 1 mL. Reactions were run overnight at room temperature. The next day, reactions were centrifuged to collect the particulate formed during the reduction. Particulate was washed with 4 × 1 mL milliQ water before the particulate was dissolved in 70% HNO_3. The solution was then diluted using 2% HNO_3 until concentrations of Te and Se fell within predetermined standardized curves.

2.4.10 *Selectivity assay*

Mtr (15 ug), 2 mM K_2TeO_3 and 2 mM $HNaSeO_3$ were combined in PBS pHs 6.0, 7.0, 8.0, 9.0 or 10.0 in triplicate. Reactions were initiated with the addition of 500 uM NADPH, brought to a final volume of 1.0 mL and run overnight at room temperature. Samples were centrifuged at 15 000 g for 10 min to collect particulate formed during the reduction, washed 4x with 1 mL milliQ water, then dried. Samples were then delivered to the Science Exchange, Inc. Biophysics and Spectroscopy Core at the University of Nebraska, Lincoln for ICP-MS and prepared with 450 uL 2% nitric acid and 50 ppb Ga.

Manuscript adapted for dissertation submission[2]*. Author contributions: ZJB (lead author) and* ***ARH*** *(2nd author) conducted experiments, wrote initial draft, and edited. KMB (co-author) conducted experiments. CJA (principal investigator) edited.*

CHAPTER 3: LABORATORY EVOLUTION OF METALLOID REDUCTASE SUBSTRATE RECOGNITION AND NANOPARTICLE PRODUCT SIZE

3.1 Introduction

Biocatalysts accomplish a staggering variety of chemical reactions at physiological (mild) temperatures, pH, and aqueous conditions. Directed evolution methods expand the sequence space frontiers for biocatalysis[92,93]. Diverse examples of evolved enzymes include those that facilitate enantioselective synthesis of active pharmaceutical ingredients[94–96], the design of more environmentally conscious and greener reaction conditions[97–100], and the further development of chemical tools which can be used to study complex biological systems[35,101–103].

Enzymes developed using directed evolution, such as those in the cytochrome p450 family, now facilitate reactions that were previously unavailable or otherwise practiced with less efficiency, enantioselectivity, or yield[104–106]. Flavin-dependent halogenases such as RebH have been evolved to halogenate an array of small molecules with high site-specificity[107–109]. Notably, a few well-placed mutations can provoke dramatic changes in both enzyme substrate specificity and the reaction catalyzed (e.g., hydroxylation vs. dealkylation). Thus, significant precedent exists for engineering enzymes toward novel biocatalyzed reactions. There are nevertheless many un- and under explored biocatalyzed reactions.

One relatively unexplored area is in enzymes that synthesize inorganic nanomaterials. Naturally occurring examples of such enzymes are common. For example, multimeric iron-storing ferritin and ferritin-like proteins oxidize soluble and highly bioavailable Fe^{2+} into uniform ferric nanoparticles as a means of promoting cellular Fe^{2+} homeomostasis[38,110,111]. Multicopper oxidases such as manganese oxidase are thought to play primary roles in the bacterial formation of geological manganese oxide materials[112–114]. Enzymes involved in the metabolization/release of sulfur compounds such as cystathionine-y-lyase are implicated in several biosynthetic routes to quantum dots (QDs), the compositions of which include cadmium sulfides[55,115–117]. In our previous work, a glutathione reductase-

like metalloid reductase (GRLMR) discovered in selenium tolerant microorganisms generated amorphous selenium nanoparticles in the presence of ionic selenium precursors such as SeO_3^{2-} (selenite) and selenodiglutathione (GS-Se-SG)[25,118–120].

Enzymes that produce inorganic materials have not yet been substantially subject to directed evolution methods; such experiments might modify the elements (bio-coordination complexes) that are preferred by the enzyme (substrate selectivity).

We are aware of only two prior efforts at directed evolution of inorganic oxidoreductases: In one instance, a chromate reductase was evolved using a 96-well plate NAD(P)H assay to increase reduction kinetics for Cr(IV) and U(VI)[121]. In a second example, ferritin was evolved to exhibit improved physical attraction to magnets through altered biomineralization of iron[122]. Notably, these examples did not change substrate selectivity. Rather these studies altered enzyme kinetics toward existing substrates or altered the physicochemical nature of the product. Therefore, to the extent of our knowledge, there are no known examples where metal(loid) reductase substrate specificities are altered through laboratory directed evolution.

It is expected that modification of metal(loid) reductase enzyme substrate specificities will benefit several academic and industrial applications. Biomining and bioremediation of metals are nascent fields which currently rely on intact microbes to extract metals from heterogeneous mixtures[123–127]. Molecular mechanisms underlying the microbial extractions are scarcely characterized[66,128]. Identification, improvement, or alteration of enzymatic processes underlying biomining may facilitate use of 'greener' approaches to metal(loid) mining.

Our motivation for altering metal(loid) reductase substrate specificity is driven by our interest in producing cloneable nanoparticles of distinct size/shape/elemental composition[129]. A cloneable inorganic nanoparticle is synthesized in physiological conditions, has well-defined elemental composition, size,

shape, and crystal structure. Because the protein determines these nanoparticle properties, and proteins are encoded in DNA, the properties of the nanoparticle are encoded in DNA.

Our cloneable nanoparticle approach relies on a combination of NADPH-dependent metal(loid) reducing enzymes (e.g., GRLMR[119], mercuric reductase[130,131], etc.) combined with metal nanoparticle binding peptides[132,133]. In this context, the elemental composition of the resulting nanoparticles is determined by the preferred enzymatic bio-coordination complex (i.e., substrate). Altering the substrate selectivity of a metal-reducing enzyme, therefore, can alter the elemental composition of a cloneable nanoparticle in which the enzyme is a component.

Herein we report the first directed evolution of a metal(loid) reductase that changes its substrate specificity. We began with GRLMR, whose preferred substrate is selenodiglutathione. A library of DNA mutants encoding the enzyme was created by error prone polymerase chain reaction (PCR). The library was expressed in *E. coli* and screened for isolates that survive in otherwise lethal concentrations of SeO_3^2. An evolved enzyme was isolated, in which the substrate selectivity for SeO_3^{2-} was greatly increased as measured by catalytic efficiency (k_{cat}/K_m). There was a corresponding decrease in the catalytic efficiency of GS-Se-SG reduction. In addition, the parent enzyme had no measurable activity towards SeO_4^{2-} (selenate), while the evolved enzyme could reduce selenate. Overall, this suggests that substrate selectivity of metal-reducing enzymes can be altered using laboratory directed evolution methods. Notably the enzyme now acts on Se in 3 different coordination environments (GS-Se-SG, SeO_3^{2-}, and SeO_4^2). In light of the findings that metal(loid) reductases can be evolved to act on a diverse range of metal(loid) coordination complexes (as opposed to free ions), the door is opened towards developing enzymes capable of acting on more dramatic ranges of inorganic coordination compound substrates – such as those with different metal(loid) centers.

3.2 Results and Discussion

3.2.1 *Enzyme kinetics*

The evolved enzyme contains two mutations: L314H and D408E. The evolved enzyme and its parent homologue (GRLMR) were evaluated with the substrates oxidized glutathione (GSSG), selenodiglutathione, and selenite. Enzymatic reactions were started by addition of NADPH to a final concentration of 200 µM. Enzyme activity was quantified spectrophotometrically by observing depletion of the characteristic NADPH absorption maximum at 340 nm. The enzyme reactions were terminated upon observation of steady state reaction kinetics.

Plots of initial enzyme velocity vs. concentration for both GRLMR and SeR with all 3 substrates are shown in Figure 3.1. The data was fitted with the Michaelis-Menten enzyme kinetic model in Origin[134]. Table 3.1 gives the K_m, V_{max} and k_{cat}/K_m values derived from for each enzyme/substrate pair. Because the evolved enzyme has a dramatically increased catalytic efficiency toward Selenite and Selenate, coupled with substantially decreased activities toward GSSG and GS-Se-SG, we name the evolved enzyme Selenium Reductase (SeR).

Table 3.1. Kinetics values K_m (mM), Vmax ($\frac{\mu M}{\min * \mu g \text{ enzyme}}$), and K_{cat}/K_m ($M^{-1}s^{-1}$) for GRLMR and SeR. Algorithmic fits to Michaelis-Menten models failed for some datasets due to marked product inhibition. Values marked with † were estimated from plots in figure 3.1. Examples of failed algorithmic fits may be found in figures S1 and S2.

Substrate	GRLMR K_m	SeR K_m	GRLMR V_{max}	SeR V_{max}	GRLMR K_{cat}/K_m	SeR K_{cat}/K_m
SeO_3^{2-}	16.9 ± 3	4.09 ± 0.8	0.0298 ± 0.004	0.102 ± 0.009	$8.82 \times 10^4 \pm 2 \times 10^4$	$1.25 \times 10^6 \pm 3 \times 10^5$
GSSG	0.411 ± 0.3	1.08 ± 0.8	0.257 ± 0.08	0.14†	$3.13 \times 10^7 \pm 3 \times 10^7$	$6.48 \times 10^6 \pm 6 \times 10^6$
GS-Se-SG	0.233 ± 0.03	0.934 ± 0.166	0.265 ± 0.0157	0.05†	$5.69 \times 10^7 \pm 9 \times 10^6$	$2.68 \times 10^6 \pm 9 \times 10^5$
TeO_3^{2-}	12†	12†	0.007†	0.025†	2.92×10^4	1.04×10^5
GS-Te-SG	0.1†	0.22†	0.015†	0.01†	7.5×10^6	$2.3 \times 10^6 \pm 3 \times 10^6$
SeO_4^{2-}	-	6.36 ± 2	-	0.005†	-	$3.93 \times 10^4 \pm 1 \times 10^4$

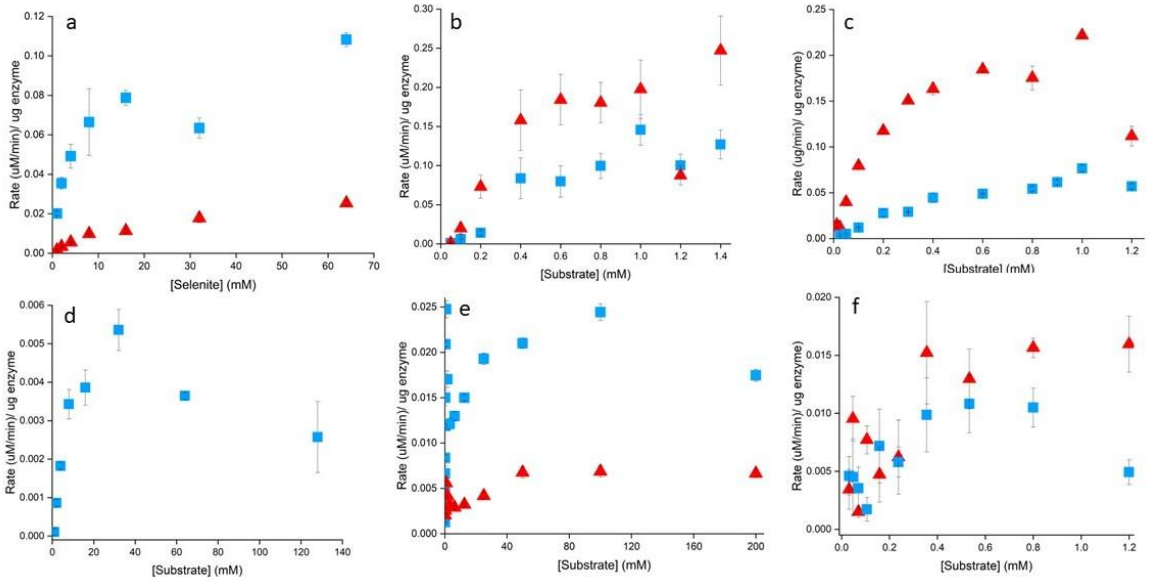

Figure 3.1. Enzyme rate plotted against substrate concentration of GRLMR (red triangles) and SeR (blue squares) comparing (A) $SeO3^{2-}$, (B) GSSG, (C) GS-Se-SG, (D) $SeO4^{2-}$, (E) $TeO3^{2-}$, and (F) GS-Te-SG

GRLMR and SeR, like glutathione reductase (GSHR), do not conform perfectly to Michaelis-Menten enzyme kinetics. The main deviation from classic Michaelis-Menten kinetics is substrate inhibition of the enzyme at higher substrate concentrations. This leads to some uncertainty in V_{max} determination. In some cases (noted with † in table 3.1), the algorithmic fits to Michaelis-Menten models were clearly flawed due to substrate inhibition resulting in artifactually low V_{max} values. These nonlinear regression fits are shown in figures A2.1 and A2.2, accompanied by explanation for which V_{max} values were estimated.

This uncertainty in Michaelis-Menten modeling – arising from product inhibition, is systematic – applying to both enzymes. Therefore, the comparative values are robust, but the absolute V_{max} values(and subsequent k_{cat} and k_{cat}/K_m interpretations) have some uncertainty that we cannot quantify. In addition, the experimental variability measured for the GSSG substrate is significantly larger than for the other substrates. This may be consistent with a ping-pong/branching mechanism suggested previously for this enzyme/substrate pair[135]. Notably, reduced experimental variability among other substrates suggests the putative mechanism of reduction for GSSG may change for other enzyme/substrate pairs.

3.2.2 *Enzyme substrate selectivity*

Catalytic efficiency (k_{cat} / K_m) of an enzyme for any substrate can allow comparison of substrate preference. Table 3.1 shows the k_{cat}/K_m values for both GRLMR and SeR for the substrates GS-Se-SG, GSSG, selenite, and selenate. The parent enzyme (GRLMR) has catalytic efficiency for the 4 substrates that follows the trend GS-Se-SG > GSSG >> SeO_3^{2-}. In comparison, SeR is much more promiscuous in substrate catalytic efficiency. For SeR, considering quantifiable experimental error, the k_{cat}/K_m are indistinguishable (GSSG = GS-Se-SG = SeO_3^{2-} >> SeO_4^{2-}).

This increase in promiscuity arises from a ~50% decrease in V_{max} for GSH based substrates, along with a ~300% increase in K_m for GS-Se-SG. Combined the k_{cat}/K_m for the GSH based substrates becomes less favorable by a factor of ~20 for GS-Se-SG and a factor of ~5 for GSSG. In contrast the V_{max} for SeO_3^{2-} increases by a factor of ~5 and the K_m decreases by a factor of 4. The overall catalytic efficiency of SeR increases from 8.82 x 10^4 to 1.25x10^6 $M^{-1}s^{-1}$ for SeO_3^{2-}. Overall, the catalytic efficiency of SeR is similar for the GSSG, GS-Se-SG, and SeO_3^{2-} substrates. Superficially, the overall effect of the enzyme evolution appears to broaden Se substrate specialization (given that all 3 substrates show similar catalytic efficiency).

Combined, this analysis shows the enzyme evolving towards a broad capacity to use selenium as a preferred substrate, instead of GS-Se-SG which is preferred by the parent enzyme[136]. This could imply that at very high concentrations of selenite (50mM in liquid culture), intracellular concentrations of selenite may exceed the usual form of intracellular selenium (GS-Se-SG), resulting in selective pressure for enzymes preferring SeO_3^{2-} over GS-Se-SG.

3.2.3 *Tellurium Substrates*

In addition to Se-based substrates, GRLMR can reduce (with less efficiency) Te based substrates such as GS-Te-SG, and TeO32-. To gain further insight into how substrate selectivity evolved with the two mutations found in SeR, we determined enzymatic constants (Km, Vmax, kcat/Km) for the known

tellurium substrates. Figure 3.1, panels e and f, give plots of initial reaction rate vs substrate concentration for GRLMR and SeR with tellurite and GS-Te-SG substrates.

Michaelis-Menten analysis was performed on these enzyme/substrate pairs. Table 3.1 lists the Km, Vmax and kcat/Km of each. Overall, catalytic efficiency for Te reduction is notably less than for Se reduction, indicating that the SeR is specialized for Se reduction. Among the Te species, catalytic efficiency for TeO32- improves by a factor of ~4, whereas catalytic efficiency for GS-Te-SG is unchanged within experimental error. Overall, the evolution of catalytic efficiency from favoring oxidized glutathione substrates to increasingly favor chalcogenide oxyanion substrates is consistent for both Se and Te based substrates.

3.2.4 *Structural Basis for Chalcogenide Oxyanion Selection*

Structural predictions for SeR and GRLMR homodimers were generated through AlphaFold2-multimer[137,138] (AF2). LocalColabFold[139] was used in conjunction with the MMseqs[140] server to rapidly prepare a multiple sequence alignment. Remaining calculations were performed on local machinery. With respect to calculation configuration, Template and Amber modes were selected to supply AF2 with template structural models to aid in prediction[141,142] (PDB entries 3DJJ, 3DK9, 4GRT, 5VDN, 5V36, 6DU7, 6N7F, 6N7F, 2R9Z, 6B4O, 1GEU, 2RAB, 2EQ6, 2EQ8, 2X8C, 7B02, 3QFA, 3EAN, and 4KPR). Final predicted structures were subjected to a molecular mechanics energy minimization step with Amber to refine bond geometry.

AF2 assesses its confidence in each amino acid prediction by the “predicted local-distance difference test” (pLDDT). The pLDDT metric ranges from 0 to 100, with higher values reflecting greater confidence in predicted structures. Typically, pLDDT values above 90 indicate a reliable prediction. Correctness of domain alignments for GRLMR and SeR were also assessed with the “predicted aligned error” (PAE) metric, which is standard practice for multimeric proteins. Low PAE values, indicating relatively high prediction correctness among alignment positions, are ideally within the 0-10 Å range (blue

in Figure A2.3). On the other hand, higher values above 15 Å (red in Figure A2.3) would indicate low inter-domain sequence quality.

Five structure prediction models for both GRLMR and SeR were generated; the average pLDDT value for each structure was above 96 (Table A2.1), indicating a high prediction reliability. The predicted dimer alignment was also of very high confidence, with average PAE scores of 4.61 and 4.72 for GRLMR and SeR, respectively (Figure A2.3, table A2.1).

Because of the possibility that the template structures used in the AF2 modeling could bias the resulting models, we also generated structures without homology templates. The template-free models resulted in structures with similar pLDDT values compared to those generated with templates; without templates, the highest confidence models maintained average pLDDT values greater than 95 – as compared to above 96 when templates were used (Tables A2.1, A2.2). Structural alignment of the template-free models showed both templated and non-templated models were very similar. We compared the templated and non-templated models by calculating the root-mean-square-deviation of α-carbon positions ($RMSD_{C\alpha}$) of the top ranked structures made with and without templates. For GRLMR and SeR the $RMSD_{C\alpha}$ difference between template and without template was 1.357Å and 0.933Å respectively. These small $RMSD_{C\alpha}$ values indicate that use of templates did not bias the resulting models. For downstream analysis, we selected the GRLMR and SeR models with the most favorable pLDDT and PAE metrics from the AlphaFold2 calculations (generated with homology templates).

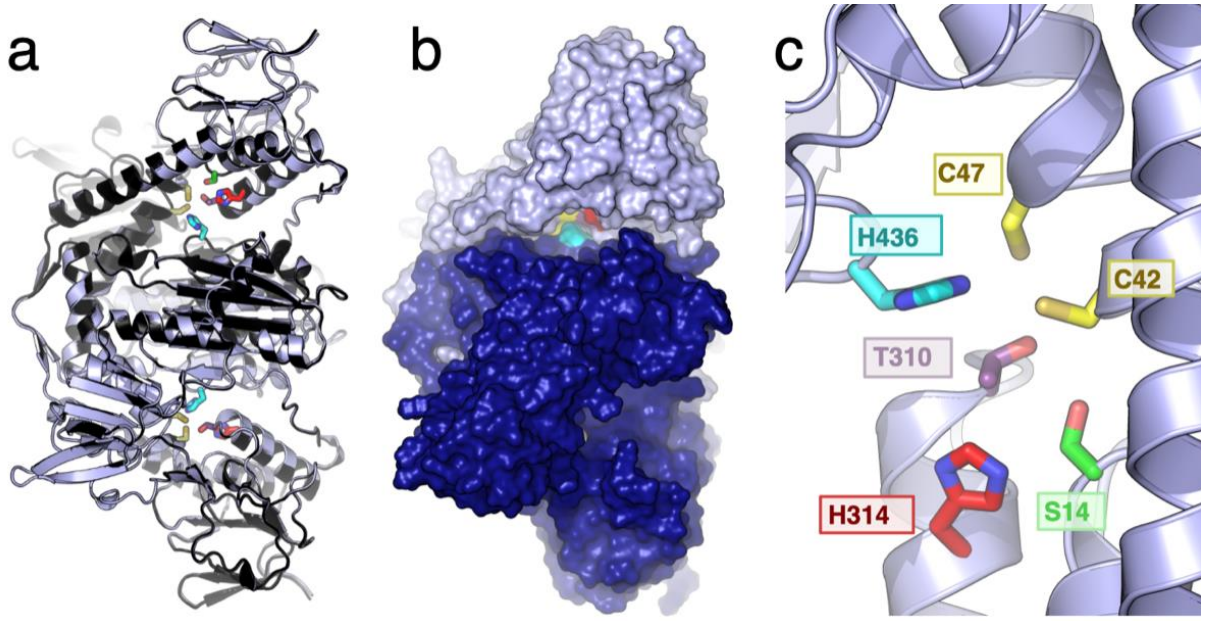

Figure 3.2: AlphaFold2 models of SeR and GRLMR homodimers. a) a 3D superposition of SeR (light blue) and GRLMR (black). Active site residues are shown in sticks: H314 (red), S14 (green), C42 (yellow), C47 (yellow), T310 (purple) and H436 (cyan). This color scheme is used to highlight these residues in all panels. b) a surface rendering of the SeR homodimer, reveals the putative substrate entry channel into the active site, with H436 (cyan) provided by chain B (dark blue). c) active site close-up rendering with residues labels.

GRLMR and SeR models were aligned in PyMOL[143] to assess their similarity. The $RMSD_{C\alpha}$ between models was calculated to be 0.963 Å, indicating very high structural homology as shown visually in figure 3.2a. The main differences between GRLMR and SeR result from two amino acid mutations: L314H and D408E. The D408E mutation sits at the homodimer interface and is 16 Å away from the closest catalytic cysteine residue (C45). The chemical change is small (aspartic acid being replaced by glutamic acid) and there is no obvious change between the GRLMR and SeR models at this position. Combined this analysis suggests that the D408E mutation is functionally a silent mutation.

Conversely, the L314H mutation sits in a position that has large implications for enzyme function. Residue 314 sits in a likely substrate entry channel in the enzyme (figure 3.2b, red patch) and is just 5 Å from the disulfide active site of the enzyme (figure 3.2c). The leucine to histidine mutation significantly alters the chemistry of this residue – from hydrophobic to an acid-base active aromatic residue. We

therefore hypothesize that enzyme activity alterations can be attributed to the L314H mutation, and we focus our analysis on this mutation.

As shown in Figure 3.2, the L314H mutation of SeR positions the histidine sidechain in the substrate entry channel. The Histidine sidechain is oriented toward the enzyme's putative disulfide active site. Only 3 other residues (T310, H236, and S14) are closer to the active side disulfide, at distances of 3.5 Å, 3.8 Å, and 4.8 Å respectively. All 3 of these residues bear functional groups implicated in enzymatic catalysis.

To assess the role of these 4 active-site proximal residues – T310, H236, S14 and H314 – we examined their homology in related enzymes in the Type-I pyridine nucleotide-disulfide oxidoreductase family. An analysis of 13 GSHRs, GRLMR, Mercuric Reductase, and Tellurite reductase shows that the disulfide is universally conserved, as expected for a catalytic active site. Similarly, S14 is conserved in all analyzed enzymes except for mercuric reductase where it is Alanine. T310 is conserved in all considered enzymes except for mercuric reductase and tellurite reductase, where it is V and K respectively. The highly conserved nature of S14 and T310 implicates these residues in catalysis.

Interestingly, the closest residue to the active site, H236, is not conserved among these enzymes. In fact, the only enzymes in which residue 236 is histidine are GRLMR and SeR -- the two Se specialized reductases present in this analysis. This implicates H236 in selectivity of chalcogenide substrates – both glutathione ligated and oxyanions -- where GRLMR out-performs GSHR in terms of catalytic efficiency for the metal(loid) reduction. Similar to residue 236, the mutation in the SeR variant – L314H also occurs at a non-conserved amino acid position. Sequence alignments for these enzymes can be found in the Supporting Information.

This analysis reveals that SeR, interestingly, positions 2 histidine residues within 5Å of the enzyme active site (H236, H314). This location of two histidine residues proximal to the enzyme active site is likely to be significant for catalytic efficiency toward Se substrates. Histidine is an aromatic residue that is well-

known to interact with metal cations (e.g., sequential His residues form the basis for immobilized metal affinity chromatography[144]). As an aromatic residue it participates in π-π interactions; addition of a nearby aromatic residue in SeR, coupled with the H236 already present in GRLMR (and retained in SeR) facilitates π-π interactions between Se substrates and the enzyme. The two active-site proximal histidine residues may help to position the SeO_3^{2-} and other Se substrates through π-Se interactions in a way that makes both K_m (substrate binding) and k_{cat} (substrate->product rate) significantly more favorable[82]. Furthermore, the size increase in a mutation of leucine to histidine may disfavor the active-site approach of GSSG and GS-Se-SG, which are significantly larger substrates than selenite. This 'steric bulk' hypothesis is supported by the enzyme kinetic analysis, where changes in K_m are significant in the evolved enzyme for GS-Se-SG and GSSG, whereas the changes in k_{cat} for these substrates are antagonistic but small. Combined the L314H mutation appears to underlie all of the observed changes in SeR catalytic efficiency relative to SeO_3^{2-}, GSSG and GS-Se-SG.

Histidine is known to interact with chalcogen with diminishing preference correlated to relative atomic size, i.e., S > Se > Te[82]. This is corroborated by our experimental results, as the mutated histidine drastically increased selenite preference and modestly increased tellurite preference.

3.2.5 *SeR and GRLMR SeNP product characterization*

Enzymatic products can change when enzymes evolve[122]. To determine if the enzymatic product had changed in any substantial way, we compared the GRLMR and SeR enzymatic products produced with SeO_3^{2-} substrates. GRLMR is known to produce approximately spherical red Se nanoparticles (SeNPs) whose size depends upon the initial concentration of SeO_3^{2-}. Modifying GRLMR could potentially change product size, morphology, and allotrope of the resulting SeNPs.

Both enzymes produce a red solution upon NADPH dependent reduction of SeO_3^{2-}, indicating that both enzymes produce the red allotrope of Se – which is amorphous, as compared to the crystalline black allotrope. The red solutions were drop cast on carbon-coated transmission electron microscopy (TEM)

grids and examined by TEM (Figure 3.3). This showed that SeR produced approximately spherical SeNPs of diameter 14.5 ± 7.4 nm and 11.2 ± 5.5 nm at 5 mM, and 50 mM SeO_3^{2-} respectively. In contrast GRLMR produced spherical SeNPs of diameter 26.8 ± 7.2 nm and 24.1 ± 7.4 nm at 5 mM and 50 mM SeO_3^{2-} respectively. SeNP aggregation was more commonly observed with SeR but was seen with both SeR and GRLMR synthesized particles at 50 mM SeO_3^{2-}.

This trend in size can also be observed by dynamic light scattering measurements (DLS). The particle sizes determined by DLS are significantly larger than those observed by TEM. We attribute this larger particle size to the inclusion of nanoparticle-associated enzymes in the DLS diameter measurement. The smaller size of SeNPs produced by SeR compared to GRLMR can be rationalized by classical nucleation theory. Here, we hypothesize that SeO_3^{2-} is reduced to either Se^{2-} or Se^0 by the enzymes. Se^{2-} is rapidly oxidized to Se^0 by dissolved oxygen[145]. The Se^0 species is essentially insoluble in water, so it has a very high propensity to nucleate and grow into SeNPs[145]. In classical nucleation theory, the critical nucleus size describes the size of a particle at which growth becomes favored over dissolution. Particles larger than the critical nucleus size tend to grow while particles smaller than the critical nucleus size tend to shrink. The critical nucleus size depends on how saturated a solution is with a given solute; for a saturated solution, the critical nucleus size becomes zero.

Because the V_{max} (k_{cat}) of SeR is improved for SeO_3^{2-} relative to GRLMR, we suggest that local concentrations of Se^0 enzymatic product are higher for SeR than for GRLMR. This makes the solutions produced by SeR locally more 'saturated', shrinking the critical nucleus size of the resulting SeNPs. The smaller SeNPs observed for SeR enzymatic products can therefore be rationalized by the higher SeR k_{cat} resulting in a smaller critical nucleus size. Increased number of nuclei leads to increased competition for growth, leading to a larger number of smaller nanoparticles.

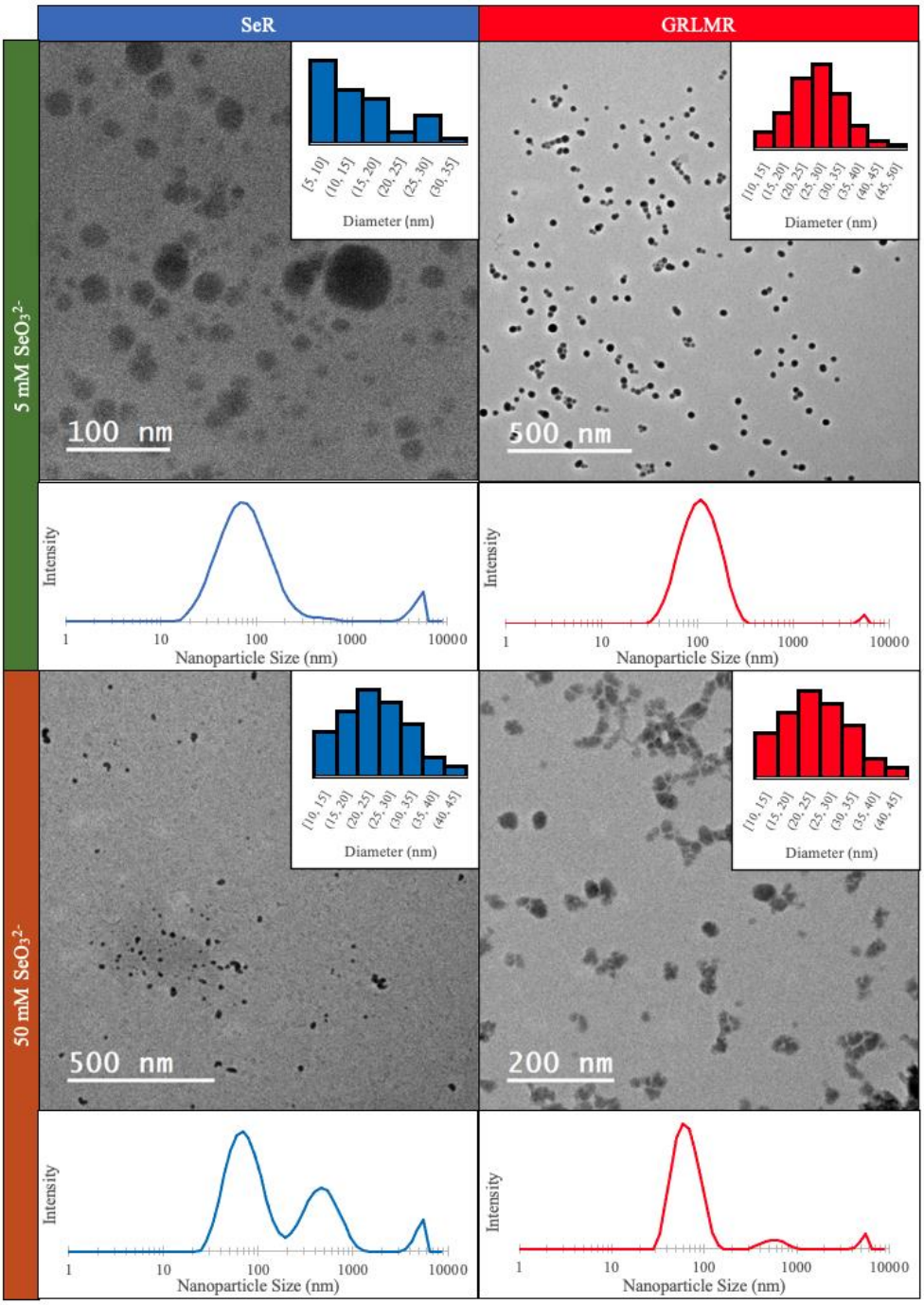

Figure 3.3. Transmission electron microscopy images of amorphous selenium nanoparticles produced by SeR (left column) and GRLMR (right column) at 5 mM SeO_3^{2-} (top row) and 50 mM SeO_3^{2-} (bottom row). DLS intensity graphs of amorphous selenium nanoparticles produced by SeR (left column) and GRLMR (right column) at 5 mM SeO_3^{2-} (top row) and 50 mM SeO_3^{2-} (bottom row). The major nanoscale peaks for each, reading from left to right, characterize the particle sizes at 90.49 nm, 114.20 nm, 76.29 nm, and 66.60 nm respectively.

3.2.6 *GRLMR Variant library creation*

Error-prone polymerase chain reaction (EP-PCR) was used to create a library of approximately 10,000 GRLMR variants. EP-PCR is a widely adopted and relatively straightforward means of introducing random mutations into defined gene segments[146]. Genes of interest ranging from hundreds to thousands of base pairs can be replicated into diversified libraries through this technique.

We used the commercially available Genemorph II Random Mutagenesis Kit (Agilent Technologies #200550) setting error-prone replication parameters to generate approximately 3-5 nucleotide mutations per 1000 bp. The resulting EP-PCR library product was ligated into pET20b. The ligation product was purified on a 1% agarose gel.

Electrocompetent E. coli cells (New England BioLabs #c3020K) were transformed with the EP-PCR library of GRLMR mutants. The library was subsequently transformed into T7 Express lysY (New England BioLabs #C3010I) for downstream selection experiments. To validate the mutational load of our WT-GRLMR DNA library, we picked 5 random colonies from the transformed library for sequencing. Of the randomly picked colonies, each displayed 3-9 point mutations within the ~1,400 bp gene sequence of GRLMR confirming our expected mutational load.

3.2.7 *Library Selection Strategy*

Enzymatic reduction of ionic metal(loids) into lower redox states (and in many instances zero-valent nanoparticulate form) is a documented detoxification mechanism for cells. While selenium is an essential nutrient, it is also toxic at higher concentrations[136,147]

Previous work has demonstrated that transformation of GRLMR into laboratory expression cells increases tolerance to selenite supplementation in the culture by nearly 10-fold, as judged by IC90 values[119]. We therefore reasoned that a selection environment could be developed wherein the survivability and proliferation of host cells could be directly correlated to the kinetic profile of mutated GRLMR.

Under this hypothesis, GRLMR variants with altered substrate specificity (e.g., altered catalytic efficiency) could be isolated by challenging host E. coli cells with toxic concentrations of substrate. The hypothesis is that cells expressing GRLMR variants with improved catalytic efficiency toward toxic Se will out-compete cells expressing variants with unchanged or decreased catalytic efficiency.

In the particular selection described here, we hypothesized that we could improve GRMLR reduction of the intracellular form of Selenium, GS-Se-SG, by challenging the cells with 50mM selenite in liquid culture. The basis for this selection is to find GRLMR variants that reduce more bio-active intracellular Se (4+) into less available Se (0) at a greater rate, promoting a competitive advantage and thus generating selective pressure in favor of the host cell. As shown above, however, this initial hypothesis was not entirely correct, as we instead unexpectedly evolved an enzyme with decreased activity toward GS-Se-SG and improved activity toward SeO_3^{2-}.

A previous study demonstrated evolution of chromate reductase in a 96-well plate format to become a catalytically more efficient enzyme toward chromate[121]. We opted to develop the selection method described here because it can accommodate much larger library sizes, with higher throughput and reduced labor. We additionally rationalized that a free-floating culture (as opposed to solid media) would prevent cells from depleting their local exterior selenite concentration, placing more selection emphasis on intracellular chemistry.

3.2.8 *Inactivating GRLMR with C42A and C47A mutations*

As a first step in library screening, we found an SeO_3^{2-} culture concentration in which cells expressing WT-GRMLR could consistently outcompete cells expressing a disabled GRLMR enzyme. Like its highly characterized parent analogue GSHR, GRLMR contains a cysteine-based disulfide which is described as the putative active site. In GRLMR, SeR, and GSHR, among others, the active site sequence motif is CXXXXC. In GRLMR, the active site cysteine residues are C42 and C47.

We used site directed mutagenesis to make C42A and C47A mutations. While the exact mechanism of metal(loid) reduction by GRLMR is currently unknown, we hypothesized that the C42A and C47A mutations would abolish GRLMR catalytic activity, with minimal perturbations to expression strength, intracellular solubility, or other factors that might confound experimental / control paired experiments.

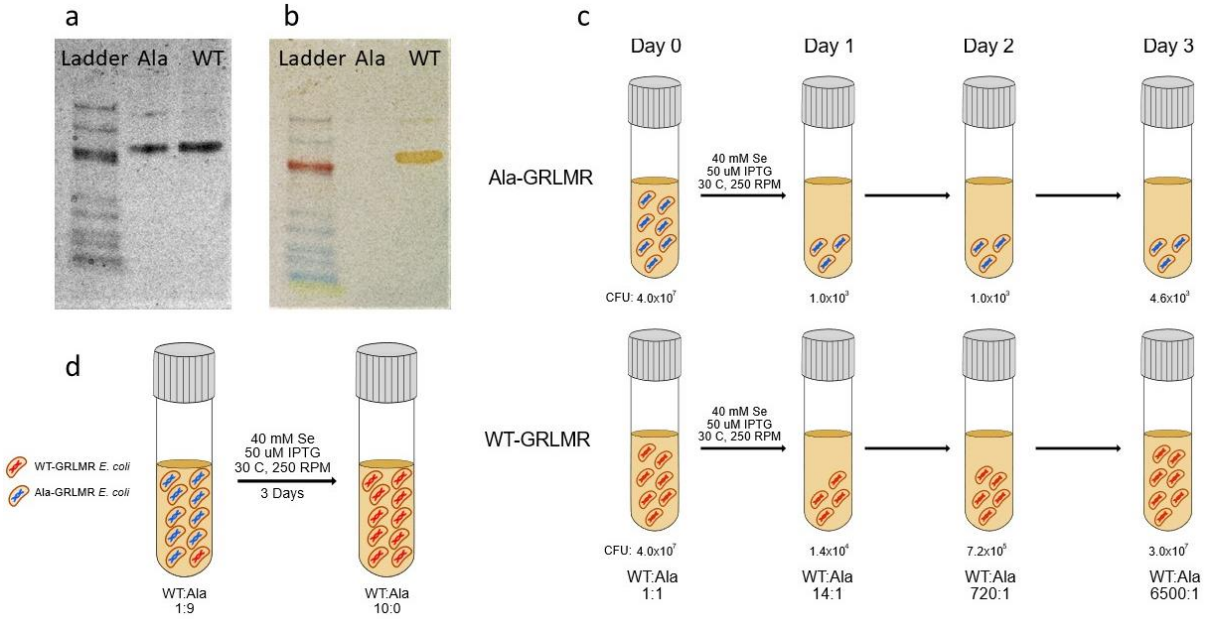

Figure 3.4. (A) Native PAGE of wild-type GRLMR and an inactivated enzyme variant (Ala-GRLMR) stained with selenite and NADPH, (B) Native-PAGE of WT-GRLMR and Ala-GRLMR stained with Coomassie, (C) Scheme depicting growth of Ala-GRLMR and WT-GRLMR in 40 mM Se, (D) Scheme depicting enrichment of WT-GRLMR from a population of Ala-GRLMR in 40 mM Se.

3.2.9 *C42, C47 mutants to GRLMR do not reduce selenite*

Figure 3.4A shows a Coomassie stained Native-PAGE gel of purified the GRLMR-C42A-C47A (Ala-GRLMR) and GRLMR side-by-side. To assay activity of the C42A, C47A mutant, we used an *in situ* assay of SeO_3^{2-} reduction capability. In this assay, a non-denaturing gel containing SeO_3^{2-} reducing enzymes is stained with a combination of SeO_3^{2-} and NADPH. The result of this assay is shown in Figure 3.4B. The assay shows a band comprised of selenium precipitates in the GRLMR lane, whereas there is no evidence

of selenium precipitates in for the Ala-GRLMR mutant. This comprises strong evidence that the mutant GRLMR is catalytically inactive.

3.2.10 *Development of live/dead selection system*

We proceeded to determine a level of SeO_3^{2-} supplementation where intracellularly expressed GRLMR endows survival and proliferation of host cells in comparison to cells expressing inactivated GRLMR.

As illustrated in Fig 3.4C, liquid cultures of WT-GRLMR and Ala-GRLMR were each inoculated and induced with an initial concentration of $4x10^7$ colony forming units (CFUs) in 2.5 mL of LB with 40 mM $HNaSeO_3$ and 50 µM IPTG. The cultures were incubated at 30 C° for 3 days. At regular intervals, the cell population was assessed in each culture. This was done by determining the number of CFUs as measured by serial dilution of 10 µL culture samples. For robustness, this experiment was done in triplicate. Cells expressing inactivated GRLMR lost population, resulting in only 400 CFU/mL by day 3. In contrast GRLMR expressing cells comparatively declined on day 1 and rebounded to the initial CFU value by day 3, resulting in a WT:Ala ratio of 6,500:1.

We subsequently tested our selection conditions by mixing a subpopulation of GRLMR expressing cells into a culture containing 10-fold more cells expressing inactivated GRLMR, as shown in Fig 3.4D. At day 3, a portion of the culture was plated on LB-Agar. From the LB-Agar, 10 colonies were grown in liquid culture, from which plasmids were purified and sequenced. This sequencing revealed that all 10 isolates contained only active GRLMR sequence. This shows that in the selection condition (40mM SeO_3^{2-}), GRLMR expressing cells outcompete those cells that express inactivated GRLMR. This condition, then, is expected to put selective pressure on cells containing a GRLMR mutant library, favoring those cells with more effective Se-reducing GRLMR variants.

3.2.11 *Selection for improved Se reduction*

Because supplementation of liquid culture with 40mM sodium selenite creates a condition where GRLMR expressing cells proliferate whereas inactivated GRLMR cells do not, we attempted selections of the EP-PCR library at 50mM sodium selenite concentration (10 mM higher than in the proof-of-concept experiments), under the hypothesis that GRLMR mutants with improved activity will out-compete WT-GRLMR in these conditions in the same way that WT-GRLMR outcompeted Ala-GRLMR.

The EP-PCR library was transformed into BL21 *E. coli* cells, and library expression was induced with 50 µM IPTG. To determine the number of cells that survived the 50mM selenite challenge, serial dilutions of 10 µL in triplicate were plated on LB-agar at 24 h intervals allowing determination of the CFU count of the culture. Similarly to earlier experiments, CFU count of the library decreased several orders of magnitude through the first day of selection, followed by rebound growth in the following days. As is shown in Figure 5A, we infer that an initial drop in CFU correlates to a loss in the overall library diversity. Subsequent cell proliferation therefore occurs from a 'fitter' subsection of the initial library, which forms the basis of evolutionary selection.

After allowing the library three days to repopulate, we inoculated 50 µL of the selection culture into 2.5 mL fresh LB/carb in preparation for a second round of selection. The outgrowth was subsequently grown to an OD of 0.5, then a 100 µL aliquot was inoculated into 2.5 mL LB/carb containing 50 mM selenite and 50 uM IPTG. The 50 mM selenite concentration was maintained in the second round to directly compare growth rates and assess if selection had occurred in the first round – under the hypothesis that a fitter population would better withstand an equal challenge.

As shown in Figure 3.5B, the cell population in this second round of selection grew to become several orders of magnitude larger than observed in the first round of selection at the same time interval and Se concentration. This much faster growth during the second round of selection implied that we had

enriched the presence of GRLMR variants that had improved Se reduction capability – therefore endowing host cells with an improved ability to survive/proliferate in 50 mM selenite.

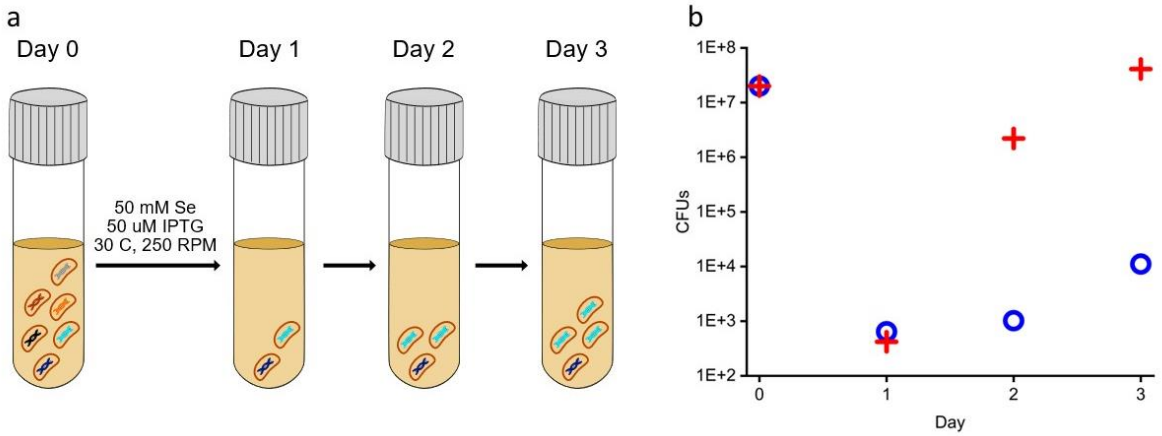

Figure 3.5. (A) Initial EP-PCR GRLMR library loses population members through the first day of Se challenge. High performing variants repopulate the overall culture over the following days. (B) Library culture CFUs over two rounds of selection; first round marked by blue circles; second round marked by red cross symbols.

A total of 10 individual plasmid preparations from the second-round selection were sequenced. All 10 sequences of the encoded GRLMR mutants were identical, containing the two-point mutations (L314H and D408E) that were characterized above. We thus reasoned that GRLMR variants had converged to the most fit variant throughout the two rounds of selection. This GRLMR variant (SeR) was fully characterized as described above.

Manuscript submission in progress: adapted for dissertation submission[3]*. Author contributions:* ***ARH*** *(lead author) and RC (2nd author) conducted experiments, wrote initial draft, and edited. GE, TT, BG, and AA (co-authors) conducted experiments and wrote initial draft. CJA (principal investigator) wrote initial draft edited. CS (co-principal investigator) edited.*

CHAPTER 4: CLONEABLE INORGANIC NANOPARTICLES

4.1 Introduction

When physicochemical properties of an inorganic nanoparticle (iNP), such as elemental composition, size, shape, crystal-structure, allotrope, optical properties, and magnetism, are encoded in DNA, the iNP is a "cloneable NP" (cNP). These cNPs are synthesized by proteins, usually inside cells. Protein sequence, and therefore structure and function, are genetically encoded. Therefore, nanoparticles whose physicochemical properties are controlled by proteins during synthesis have their properties encoded in DNA. This framing implies that the DNA encoding any cNP can be recombinantly transferred into any organism, endowing that organism with the ability to make the cNP.

cNPs as defined in this article, are made in living cells. cNPs *do* occur naturally. Magnetosomes[148,149], ferritins[38,150,151], and DNA-binding protein from starved cells (Dps)[152,153] are examples of naturally occurring cNPs. Each of these examples makes an iron oxide nanoparticle of defined size, shape, elemental composition, and magnetism.

cNPs represent a sub-type of biogenic inorganic nanoparticle (bNP); all cloneable NPs are biogenic, but not all biogenic NPs are cloneable. Inorganic bNPs may be made by cells, cell-extracts, or purified biomolecules[66,126,154,155]. Because bNPs need not be synthesized by live cells, their synthesis occurs in broader "chemical space" than the strict cellular space in which cNPs are made.

Both cNPs and bNPs are synthesized in aqueous conditions, at physiological pH and mild temperature. Many of the iNP products made with biomolecules would otherwise require high temperatures, organic solvents, and/or extreme pH if made using *in vitro* methods.

Whereas cNPs employ protein(s) for well-defined control of NP properties, the broader class of bNPs can be synthesized with small biomolecules, such as sugars[156], amino acids[157], nucleotides[158], library isolated peptides[159], proteins and yet to be defined biomolecules present in cell extracts[160]. It is possible

that cNPs could be found that are made with genetic molecules that are not proteins; however, there are currently no known instances. bNP products also tend to be less well defined than cNPs.

cNPs require metal(loids) that are at least transitively stable inside cells (e.g., not easily reduced by ubiquitous reducing molecules such as sugars and aromatic or thiol-containing amino acids). Such metal(loid)s include essential elements such as Fe, Co, Zn, Se and Mo. Generally regarded as nontoxic elements, such as Bi (a pharmaceutical component in Pepto Bismol) can also form the basis for a cNP. In contrast, bNPs can be made *in vitro* or *in vivo* and any element from the periodic table could in principle be added as a coordination complex or oxyanion to an *in vitro* reaction, representing a more flexible synthetic space.

bNPs (and therefore cNPs) attract interest for a diverse array of applications. Our primary interest in cNP engineering is to make cloneable contrast in images of biological systems generated with X-rays, electrons, light and/or magnets (i.e., electron microscopes, CT-scanners, optical microscopes, and MRI imagers). Our secondary interest is using cNPs for environmental bioremediation of metal(loid) contaminations.

Others are developing bNPs for uses involving but not limited to catalysis[161], solar photoconversion[162], antimicrobial therapy[163,164], and theranostic (i.e., combined therapeutics and diagnostics) agents[165,166]. Biogenesis can simply be a greener means of obtaining the necessary iNPs in many of these instances. On the other hand, biogenesis can also offer improved methods of tuning iNP biocompatibility and function within cellular contexts. In all bNP applications, it is probable that the cNP approach may represent a more engineerable, directable platform compared to less well-defined bNPs.

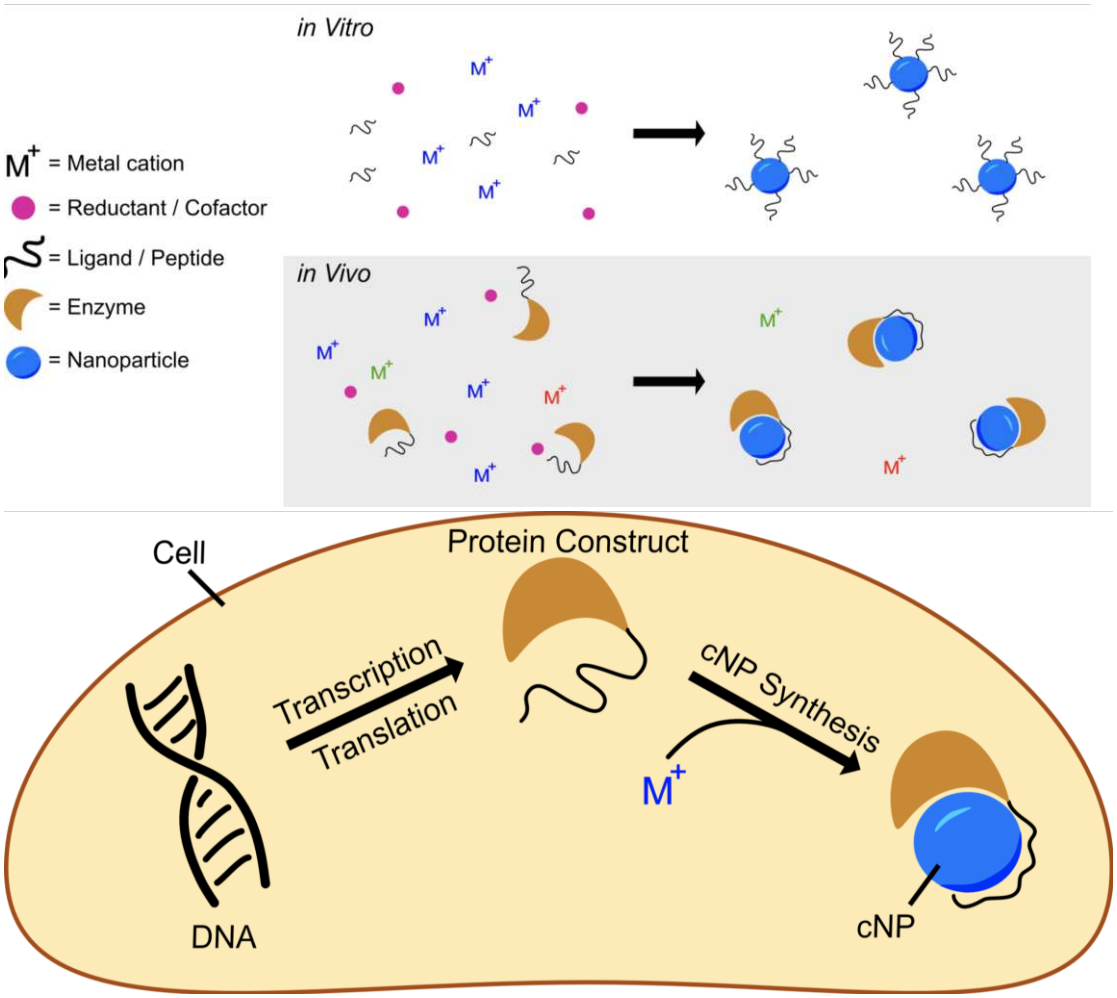

Figure 4.1. Schematics showing reductive nanoparticle synthesis approaches in vitro (top panel) and in vivo (bottom panel).

4.1.1 *The cNP synthesis paradigm*

We have developed a modular cNP platform that links genotype (DNA) to phenotype (cNP composition). This platform adapts *in vitro* NP synthesis (Figure 4.1, top panel) approaches to use cellularly available reactants (Figure 4.1, bottom panel).

In vitro reductive iNP synthesis usually begins with three chemical components: inorganic cations, reductants, and ligands. In this synthetic approach, reductants change the oxidation states of cations from soluble (e.g., aqueous) to insoluble (particulate, solid) states. Very often, the reduced particulate oxidation

state is zerovalent. Ligands present during synthesis cap growing inorganic solids at nanoparticulate size, suppressing growth into macroscopic bulk solid[167] and directing particle size, shape, fluorescence, etc.

In adapting this paradigm to cellular environments, we similarly use three distinct chemical components, with the additional use of inorganic ion oxidoreductases. In this context, bioavailable metal(loid) cations or coordination complexes act as the metal(loid) source. Inorganic ion oxidoreductases select the 'desired' ion from a background that contains all essential elements (Se, Zn, Fe, etc). Enzyme cofactors (NADH, NADPH, glutaredoxin, etc.) act in concert with enzymes as the reductant. Peptides or proteins that bind to and/or control iNP properties can be concatenated to or coexpressed with the oxidoreductase and act as ligands in cNP synthesis; in this role, they offer the prospect of size, shape, and crystal structure definition. The combination of oxidoreductases and iNP binding peptides/proteins results in synthetic control of cNP synthesis inside cells that can rival the synthetic control that is possible with well-developed *in vitro* methods.

4.1.2 *cNP composition parameters*

Many intracellular metal ions are glutathione-ligated, in part due to the ~mM concentration of glutathione (GSH) inside most cells, combined with the high affinity of thiols for many metal(loids)[168]. Many metal(loid) oxidoreductases are thus unsurprisingly related to glutathione reductase (GSHR). GSHR[169,170], mercuric reductase[56], tellurite reductase[2], and GRLMR[75] all belong to the class I FAD dependent oxidoreductase enzyme family. Functional differences among enzymes in this family mainly comprise substrate selection—where substrates are different metal(loids) ligated by GSH.

As a class of enzymes, inorganic ion oxidoreductases include mercuric reductase, arsenate reductase[171], chromate reductase[172], GRLMR, Tellurite reductase, and ferredoxin[151]. Many times, these enzymes are isolated from organisms adapted to environments with high concentrations of metal(loids)[173]. Here the enzymes represent components of detoxification mechanisms for otherwise toxic concentrations of metal(loids).

Enzymatic metal(loid) ion reduction is a relatively common cellular feature. Many enzymatic systems are therefore potentially on the verge of being engineered into viable cNPs; however, most lack an integrated means of enforcing size and shape control. A great deal of iNP binding peptides have, in contrast, been described for their ability to exert strong influence on NP shape and size yet lack intrinsic means of reducing metal(loid) cations. Thus, the combination of iNP-binding peptides with metal(loid) ion reductases represents a platform or paradigm for cNP synthesis.

iNP binding dodecapeptides were first isolated from phage display libraries[132]. So-far, peptides that bind to a about 100 iNPs of differing size/shape/elemental composition are now described in the literature. A subset of iNP binding peptides can also assist in the synthesis of iNPs. For instance, A3 peptide in the presence of Au^{3+} salts and a reductant (which can include the buffer HEPES serving as reductant) makes 10nm AuNPs. The Ge8 peptide, in the presence of $AgNO_3$ and H_2O_2, makes chiral, curved silver nanowires[174].

These synthesis-assisting peptides do not constitute cNPs on their own; while they are encoded in DNA, they do not change the oxidation states of the ions (and therefore solubility). Thus, they do not represent a self-contained cNP system. Notably, some of the early literature on iNP binding peptides confuses this issue, as early papers did not recognize that buffer salts can donate electrons to and reduce many metal ions[175,176].

Naturally occurring iNP binding peptides/proteins may also function as ligands in cNP synthesis. A peptide isolated from the magnetosome formation machinery, mms6, can template the formation of magnetic FeO particles[177,178]. Attempts to reconstitute the magnetosome machinery recombinantly in model cell systems results in intracellular membrane encapsulated magnetite minerals[179]. Naturally occurring magnetosomes are membrane invaginations[180]; it is presently unclear why recombinant magnetosome reconstitution results in membrane encapsulation. The toxicity of Fe^{n+} ions (in Fenton chemistry[181]) may underlie the observation that all Fe_nO_m particles observed in healthy cells are

encapsulated either by proteins or membranes. While Fe_nO_m NPs are attractive as contrast agents, the observed encapsulation aspect makes them less appealing as cNPs for high resolution electron microscopy (EM) contrast generation.

Many proteins have also been identified that bind to inorganic nanoparticles and might therefore similarly control their shape and size during synthesis. Broadly speaking, there is existing literature on proteins that form a 'corona' around iNPs[182,183]. For selenium nanoparticle(s) (SeNPs) a proteomic study identified about 50 proteins that are found in the SeNP corona,[184] for SeNPs made in cells or exposed to cell extracts. Generally, proteomic mass-spectrometry methods are effective at identifying proteins from biological matrices that bind to iNPs.

Purification of iNPs from biological matrices, followed by proteomic MS on those particles, identifies proteins that purposefully or serendipitously bind to iNPs of particular elemental composition/size/shape. Research on whether such proteins can influence bNP/cNP size/shape during synthesis remains at a preliminary stage. Proteomic mass spectrometry studies do not identify aspects such as affinity abundance or inorganic crystal facet-specific binding of peptides. The translation of proteomic MS identification of proteins to chemical information on how or why such proteins associate with iNPs is in its infancy.

By analogy to what is now known about library isolated peptides in the context of bNP synthesis, we expect that some naturally occurring proteins can also direct bNP/cNP size and shape. That suite of proteins may include those that confer an adaptive advantage to their host (in the context of metal toxicity) and those that evolved for other functional endpoints but serendipitously control bNP/cNP size/shape.

Above we outlined cellular equivalents of reductants and ligands that can synthesize well-defined cNPs. This combination cellular reductants and ligands can be encoded in a single chimeric DNA construct. This results in a chimeric protein that incorporates all chemical activities required to make a cNP.

Because a single protein (polypeptide chain) controls all functions, mutations to the DNA that encode the protein can subsequently 'mutate' or change the properties of the cNP that the protein synthesizes. This allows the adaptation of recently developed and powerful directed evolution methods for the purpose of cellular nanoparticle synthesis[93].

4.1.3 *Cloneable contrast*

Our primary motivation in developing the cNP platform is to develop cloneable imaging contrast. Cloneable contrast imaging agents, such as green fluorescent protein (GFP), were first described and adopted for fluorescence microscopy[185,186]. What makes GFP useful in imaging is that the DNA encoding GFP can be easily 'cloned' or concatenated to the DNA encoding any protein of interest. The protein of interest now 'lights up' in fluorescence microscopy and is distinctly visible against the cellular background, where nothing else fluoresces notably at the GFP emission wavelength of 509nm. Meanwhile, the available toolbox of fluorescent proteins has grown to the extent that multi-color (multiplexed imaging) studies are routine—e.g., dynamic protein interactions with several players can be observed[187].

Cloneable contrast agents that function in electron, magnet and X-ray-based imaging modalities are extensively explored, but not yet widely adopted by biologists using these imaging methods. Such modalities are nevertheless important, as they allow tissue imaging in magnification and penetration domains outside what visible-light microscopy is capable of. Cloneable contrast, as outlined below, may or may not use approaches that create cNPs. Approaches that use ferritin, singlet-oxygen generation proteins, and phytochelatins—such as metallothionein—are outlined below.

Ferritin is a ~400 kDa protein constituted from 24 polypeptide units. Under iron-rich conditions, ferritins can store up to ~4500 iron atoms as a highly regulated mineral core, which can be easily observable in certain imaging contexts such as EM or correlative light and electron microscopy (CLEM)[38,150].

Many proteins can be used to locally deposit diaminobenzidine (DAB) polymer, such as mini singlet oxygen generator[35] (miniSOG) and engineered ascorbate peroxidase[188] (APEX2). In these cases, proteins produce radical oxygen through various means, which subsequently polymerize DAB to form osmiophilic polymers. These polymers then absorb electron dense osmium stains proximal to the point of polymer origination. Proteins, such as horseradish peroxidase, have also been used extensively in the past—before the advent of cloneable contrast tags.

Metallothioneins are small (0.5-14 kDa) cysteine-rich proteins which stoichiometrically bind metal atoms. Previous works have demonstrated that metallothionein can bind a wide array of metal atoms, including Au, Pt, Ag, Pb, Cd, and As. Metallothioneins have been implemented as cloneable contrast tags.[189]

GFP represents a 'benchmark' for cloneable imaging contrast. The properties of GFP that make it so useful are: (1) it works in both live and fixed cells; (2) it is entirely self-contained in a single DNA segment—requiring nothing further (such as exogenous building blocks or upstream cellular engineering) (3) There is 1 GFP for each protein that it is concatenated to. This allows straightforward quantification of protein copy number through quantification of fluorescence signal.

So far, no cloneable contrast approach for EM is widely used because there are severe limitations associated with each method proposed to date:

Ferritin presents two substantial challenges for widespread use as a cNP. First, its multimericity can heavily convolute labelling strategies. Second, its excessively large mass can shadow-cast surrounding tissue areas, heavily influencing diffusion kinetics of concatemerized protein(s) of interest (POIs) and in turn biasing intracellular processes.

While osmiophilic DAB polymers can be a highly sensitive method of enhancing contrast, they diffuse up to 200 nm away from their point of origination, substantially reducing the resolution at which interpretations of images (collected at much higher resolution) can be made. DAB polymerization is

moreover infeasible in living cells or in frozen-hydrated cells, requiring fixation which introduces imaging artefacts.

Metallothioneins bind approximately 20 metal atoms per protein unit, which is barely visible above the background in electron micrographs. This is also exacerbated by competition from natively expressed metallothionein, which upregulates in the presence of high intracellular metal concentration.

Cloneable contrast approaches in X-ray and Magnetic imaging are in their infancy[190] . The advent of cloneable contrast agents, which overcome the limitations of current systems and can simultaneously be used in several imaging modalities (EM, X-ray, MRI), is therefore expected to find rapid adoption in the biological imaging community.

Inorganic nanoparticles are known to have properties that can produce contrast in EM, visible-light, X-ray, and magnetic imaging modalities. An appropriately formulated cNP may therefore be able to produce contrast in each of these imaging modalities simultaneously.

This feature article outlines our development of a cNP platform, with some applications highlighted. The most 'mature cNP' in our lab is comprised of ~5 nm Selenium NPs—making it a cloneable selenium nanoparticle (cSeNP.)

We summarize a set of 4 papers from our group, which in concert describe the development of this cSeNP platform. The reductase is Glutathione Reductase-Like Metalloid Reductase (GRLMR), which was isolated from *Pseudomonas moraviensis* subspecies stanleyae—among the most Se tolerant microorganisms ever described. This species may show promise for bioremediation of selenium contamination—an area where previous work has been done collecting biogenically produced Se(0) from wastewater[118,126].

Transmission electron microscopy (TEM) and electron tomography of the *P. moraviensis* stanleyae shows ~50 nm diameter intracellular SeNPs. There is no apparent membrane or protein structure

surrounding these SeNPs. GRLMR can be transferred among species, endowing other species with enhanced Se tolerance.

GRLMR alone does not control SeNP size. To introduce size control, we isolated a peptide that binds to SeNPs from a phage display library. Concatenation of this peptide to GRLMR at the DNA level results in a construct that consistently makes 35nm diameter SeNPs *in vitro* and ~5 nm diameter SeNPs *in vivo*. Furthermore, we show that inclusion of transition metals such as Cadmium in the cell cultures that make cSeNPs allows instead the production of CdSe semiconductor quantum dots.

There are 'less mature' cNPs in the pipeline in our lab. For instance, we have isolated a tellurium reductase from environmental isolates, and this may form the basis for a cloneable tellurium nanoparticle in future work.

While not a cNP, we have examined metallothionein as a cloneable contrast agent, concluding that it must be present in high copy number to be visible in EM.

We have also made some substantial and unpublished investigation of the capsule-forming and Fe-concentrating protein Dps. Here we will outline our approach and the shortcomings of that approach that made us unenthusiastic about further exploration.

4.2 Paper Summaries

4.2.1 *Pseudomonas moraviensis subsp. stanleyae, a bacterial endophyte of hyperaccumulator Stanleya pinnata, is capable of efficient selenite reduction to elemental selenium under aerobic conditions*[118]

Our work on the cSeNP began with isolation and characterization of a bacterium specialized for high Se conditions[118]. In this paper, we report *Pseudomonas moraviensis* subspecies stanleyae, a bacterial endophyte that was isolated from the root tissue of Se hyperaccumulator *Stanleyae pinnata* (colloquial name Prince's Plume) found growing in the naturally seleniferous soil in the Pine Ridge Natural area of Colorado, USA.

The bacterium was characterized phylogenetically by fatty acid methyl ester analysis and multi locus sequence analysis. The sequence analysis showed 97.3% nucleotide identity to *P. moraviensis*. This subspecies was therefore dubbed *Pseudomonas moraviensis* stanleyae, taking the name of the plant in which it was found.

Because *P. moraviensis* stanleyae was found as an endophyte in a selenium hyperaccumulating plant, it was hypothesized that the bacterium is a selenium specialist (possibly working in symbiosis with the plant in which it lives).

The bacterial strain was grown in various concentrations of SeO_4^{2-} (selenate) and SeO_3^{2-} (selenite). When grown on selenite supplemented LB-agar, the bacterial colonies appeared bright red—consistent with production of red-allotrope SeNPs (Figure 2, panel A). When examined by TEM, rod shaped bacteria coated with SeNPs were apparent (Figure 2, panel B.) Overall, we observed that the bacterium could tolerate up to 120 mM of selenite and 150 mM selenate, making this the most selenium tolerant organism so-far described.

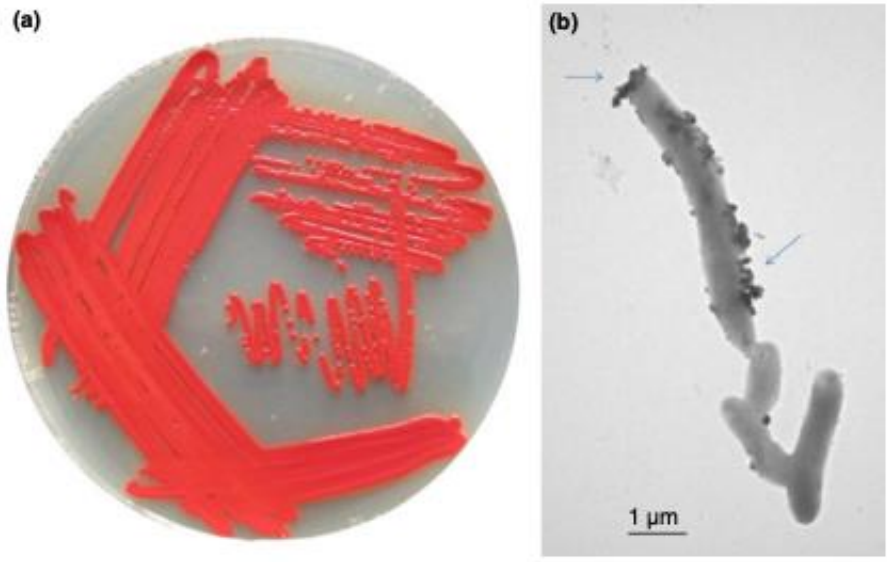

Figure 4.2. Panel a shows *P. moraviensis* stanleyae growing on SeO_3^{2-} supplemented agar. The red color is indicative of red Se(0) formation as a result of selenite reduction. Panel b shows a TEM image of *P. moraviensis* stanleyae grown in the presence of selenite. The bacteria appear coated with SeNPs.

Growth kinetics in the presence of high concentrations of Se oxyanions showed that the growth of *P. moraviensis* stanleyae was not significantly impeded by 10 mM selenate—but no red Se(0) was observed with selenate. In the presence of selenite, growth was somewhat slower, and red selenite appeared after about 10 hours (Figure 4.3).

The observation that *P. moraviensis* stanleyae converted SeO_3^{2-} to Se(0) while SeO_4^{2-} was not reduced was also made by observing the aerobic reduction of each selenium oxyanion. Figure 4.4 shows the concentration of SeO_3^{2-} and SeO_4^{2-} as determined by a microchip capillary electrophoresis method that we developed for this purpose (cite the Anal Chem article). This figure shows that SeO_4^{2-} concentrations persisted near their original 10 mM concentrations in the culture for as long as they were measured (up to 50 hours). SeO_3^{2-} concentration, however, diminished over time due to its reduction to red Se(0). Combined, these observations suggest that the mechanism for SeO_3^{2-} tolerance involves conversion of SeO_3^{2-} to Se(0), whereas SeO_4^{2-} tolerance must be due to other mechanisms that do not reduce selenium oxyanions (such as efflux pumping). Overall, this paper identifies the most Se tolerant organism described to date, capable of surviving in liquid culture supplemented with up to 150 mM SeO_4^{2-}. Subsequent work determines the molecular mechanism of SeO_3^{2-} reduction.

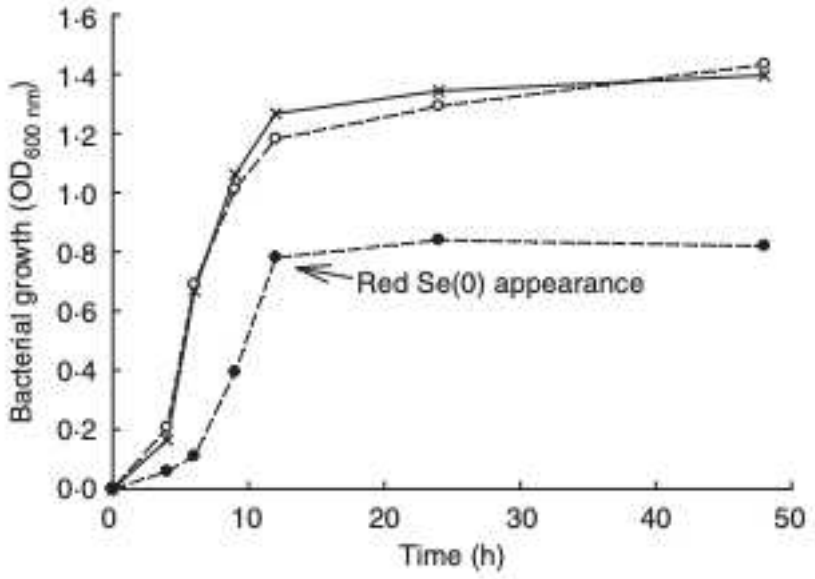

Figure 4.3. Aerobic growth of *P. moraviensis* stanleyae in Luria Broth media without Se oxyanions (x), and in the presence of 10mM selenite (solid circles) and 10mM $SeO_4$2- (open circles).

4.2.2 *Progress toward cloneable inorganic nanoparticles*[25]

We continued the characterization of *P. moraviensis* stanleyae in *Nanoscale*, 2015, 7, 17320-17327[25]. This paper focuses on electron microscopy characterization of *P. moraviensis* stanleyae and unraveling the mechanism of SeO_3^{2-} reduction.

The initial EM imaging of *P. moraviensis* stanleyae () left several microscopic aspects of the system ambiguous. From these images, it is unclear whether SeNPs are present inside cells as well as outside cells. This initial data also lacks elemental imaging, which could confirm that the punctate inclusions are in fact comprised of Se, as inferred.

In the present paper, *P. moraviensis* stanleyae cells were grown in the presence of SeO_3^{2-} and cells were then imaged by scanning electron microscopy (SEM) as glutaraldehyde-fixed dehydrated cells. The SEM based imaging allows energy dispersive X-ray spectroscopy (EDS) elemental analysis of the cells.

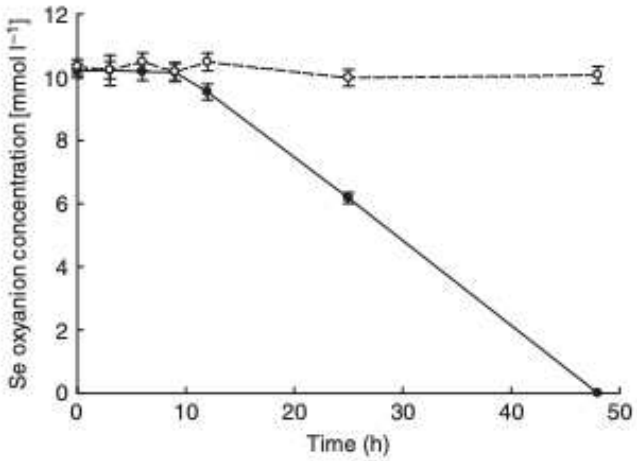

Figure 4.4. Aerobic reduction of $SeO_4$2- (open circles) and $SeO_3$2- (closed circles) by *P. moraviensis* stanleyae as a function of time.

SEM imaging revealed capsule-shaped cells, most of which contained one or more dark inclusions. EDS mapping showed that these inclusions were Se rich, suggesting that these are SeNPs. The putative SeNPs were circular with an average diameter of 107 ± 35 nm (for 50 observations). These dark inclusions were not observed in control experiments where *P. moraviensis* stanleyae was grown in the absence of Se supplementation.

To this point, it was unclear if SeNPs were present inside or outside of the observed cells. Electron tomography is an imaging modality that allows 3D reconstructions of cells, which can resolve questions about particle location. *P. moraviensis* stanleyae was again grown with selenite supplementation and was preserved for electron tomographic image acquisition by freeze substitution. In this method, cells are vitrified by high pressure freezing, then the water in the cells is substituted for acetone. Following acetone substitution, the cells can be fixed and plastic embedded. This approach is recognized as providing the highest fidelity preservation of cellular ultrastructure outside of imaging of cells that are vitrified and imaged as frozen-hydrated samples (which is technically difficult to do for cells that are as thick as *P. moraviensis* stanleyae.)

The results of electron tomographic reconstruction of *P. moraviensis* stanleyae are shown in Figure 4.5. Figure 4.5 panel A shows a 2D image of a *P. moraviensis* stanleyae cell, which contains two very clear large inclusions, assumed to be SeNPs. Panels B and C show a 3D reconstruction of the cell. The reconstruction is segmented so that the membrane is shown in green and putative SeNPs are shown in red. The reconstruction reveals 3 additional particles that were not apparent in the 2D image (possibly because they were distant from the focal plane and/or too small to be visible in the 2D image. It is common for 3D reconstructions to reveal details that are not visible in any of the 2D images used to perform the reconstruction.

Panels B and C of Figure 4.5 show unambiguously that the putative SeNPs are present intracellularly. Furthermore, there is no evidence for membrane encapsulation, which is observed for other inorganic intracellular NPs, such as magnetite within membrane encapsulated magnetosomes[178]. Panels D and E of Figure 4.5 show 2 of the SeNPs at greater magnification. The individual particles are irregular in shape, although overall they are approximately spherical. The irregularity in shape suggests that there is no structured protein coat surrounding these particles, as is the case with other intracellular NPs such as ferritin and Dps.

Most inorganic clusters and nanoparticles require an organic ligand shell to be stable; in the absence of a ligand shell, inorganic nanoparticles fuse, ultimately forming macroscopic

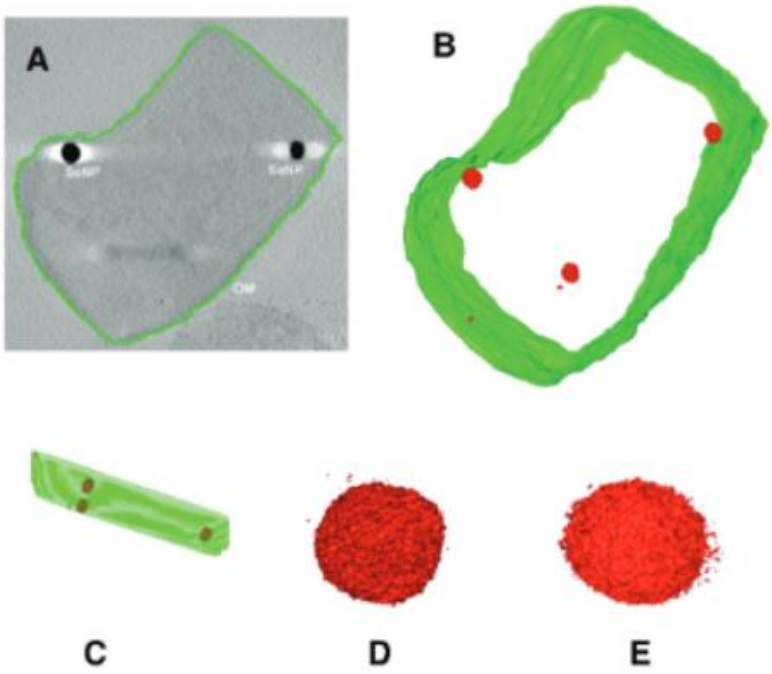

Figure 4.5. Electron tomographic reconstruction of *P. moraviensis* stanleyae grown in SeO_3^{2-} media. The reconstruction was segmented to reveal the outer membrane and SeNPs (panels A-C). Panels D and E show two of the SeNPs at higher magnification.

material. Selenium, however, is one of a handful of elements for which 'naked' or un-ligated clusters and nanoparticles are stable. The reasoning for this is that Se (as well as As, Bi and Sb, among others) can self-satisfy its valence bonding conditions by bonding to other Se atoms[191]. This aspect of Se chemistry suggests that the SeNPs inside *P. moraviensis* stanleyae might not have or need a well-defined biological coating, such as those found around iron oxides. It is probable that the SeNPs do maintain a so-called 'protein corona,' but that this forms as a result of direct exposure of the surface of SeNPs to bacterial cytoplasm.

To gain insight into the mechanism of intracellular SeNP formation, we assayed all soluble proteins of *P. moraviensis* stanleyae for SeO_3^{2-} reduction capability. This assay involved fractionating all the soluble proteins from *P. moraviensis* stanleyae on a non-denaturing gel, which is expected to leave enzyme function intact. Non-denaturing gels containing all soluble proteins were incubated with SeO_3^{2-} salts and various enzyme cofactors, including NADH and NADPH. With the combination of NADPH and SeO_3^{2-}, we

observed a set of red bands in the gel, presumably comprised of Se(0) precipitates made by NADPH dependent enzymatic reduction of SeO_3^{2-} (Figure 4.6). The bands did not appear in the absence of NADPH and appeared very faintly in the presence of NADH.

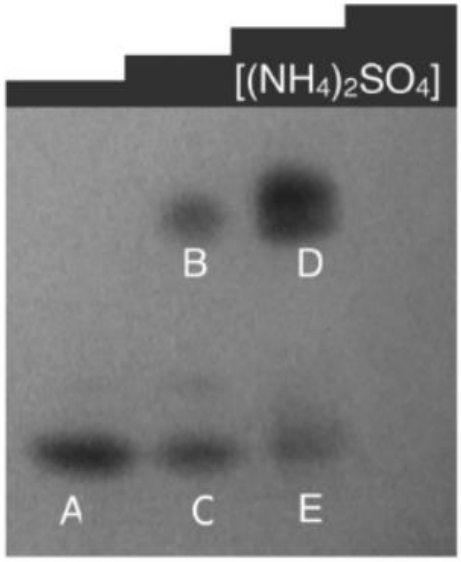

Figure 4.6. Non-denaturing gel of soluble proteins from *P. moraviensis* stanleyae, stained with NADPH and SeO_3^{2-}. The lanes correspond to fractions eluted from a hydrophobic interaction column at various concentrations of ammonium sulfate. Bands appear where NADPH dependent SeO_3^{2-} activity is spatially localized.

To identify the NADPH dependent enzyme(s) responsible for SeO_3^{2-} precipitation, we excised each band from the gel and subjected it to proteomic mass spectrometry analysis. This analysis revealed a total of 7 NADPH dependent enzymes out of 113 total proteins present in the combination of all 5 lanes. The NADPH dependent enzymes were Nitrite and sulfite reductase, isocitrate dehydrogenase, glutathione reductase, Methylenetetrahydrofolate reductase, ketoacyl-ACP reductase, Thiol peroxidase and 4-Aminobutyrate aminotransferase.

Of these enzymes, we hypothesized that a glutathione reductase-like enzyme was primarily responsible for SeNP particle formation, because glutathione reductase (GSHR) belongs to the same enzyme family as mercuric reductase, and GSHR has also been shown to reduce Au^{3+} ions[192]. To address this hypothesis, we acquired commercially produced GSHR from Sigma-Aldrich, and tested it for SeO_3^{2-}

reductase activity. We observed that GSHR produced spherical SeNPs of an average diameter of 61±37 nm *in vitro,* when both SeO_3^{2-} and NADPH were present. Notably, we also observed that GSHR reduced TeO_3^{2-} as well.

Combined, this paper shows that GSHR can reduce SeO_3^{2-} intracellularly in an NADPH dependent process. The enzymatic product is SeNPs, of relatively high polydispersity. The SeNPs are thought to be 'naked' or stable without a defined and monolayer-like ligand shell. Overall, this paper postulates that GSHR or similar inorganic ion reductases form a promising basis for cNPs as enzymes that make electron dense intracellular nanoparticles from essential elements. A full adaptation of such reductases should include better SeNP size control, retention of the SeNP at the enzyme, and enzymes that reduce their metal substrates faster and more effectively than 'background' reduction by, for example, native GSHR.

4.2.3 *Metalloid Reductase of Pseudomonas moraviensis Stanleyae Conveys Nanoparticle Mediated Metalloid Tolerance*[75]

Under the hypothesis that the GSHR from *P. moraviensis* stanleyae is specialized for Se reduction, we proceeded with study of the *P. moraviensis* stanleyae GSHR. In the paper, we began by sequencing the genome of *P. moraviensis* stanleyae. From the whole genome sequence, we identified the DNA encoding the most closely related enzyme to GSHR from this organism. This sequence was cloned into a protein expression vector, and the GSHR-like protein from *P. moraviensis* stanleyae was expressed recombinantly in *Escherichia coli*.

The substrate selectivity of the *P. moraviensis* stanleyae GSHR-like protein was determined for oxidized glutathione (GSSG), selenite, and selenodiglutathione (GS-Se-SG). For comparison, commercially obtained baker's yeast GSHR was analyzed with the same substrates.

Enzyme assays for the GSHR-like enzyme and GSHR are shown in Figure 4.7. Michaelis-Menten analysis of this data revealed that the *P. moraviensis* stanleyae GSHR-like enzyme prefers GS-Se-SG as a substrate over GS-SG; the K_M for GSSG was determined to be 8.22 mM for GSSG and 336 μM for GS-Se-

SG. For baker's yeast GSHR, the K_M values for each substrate were similar (103 µM and 133 µM for GSSG and GS-Se-SG respectively)—showing a slightly greater affinity for GSSG substrates. Other investigations of substrate selectivity for baker's yeast GSHR found similar K_M values[193].

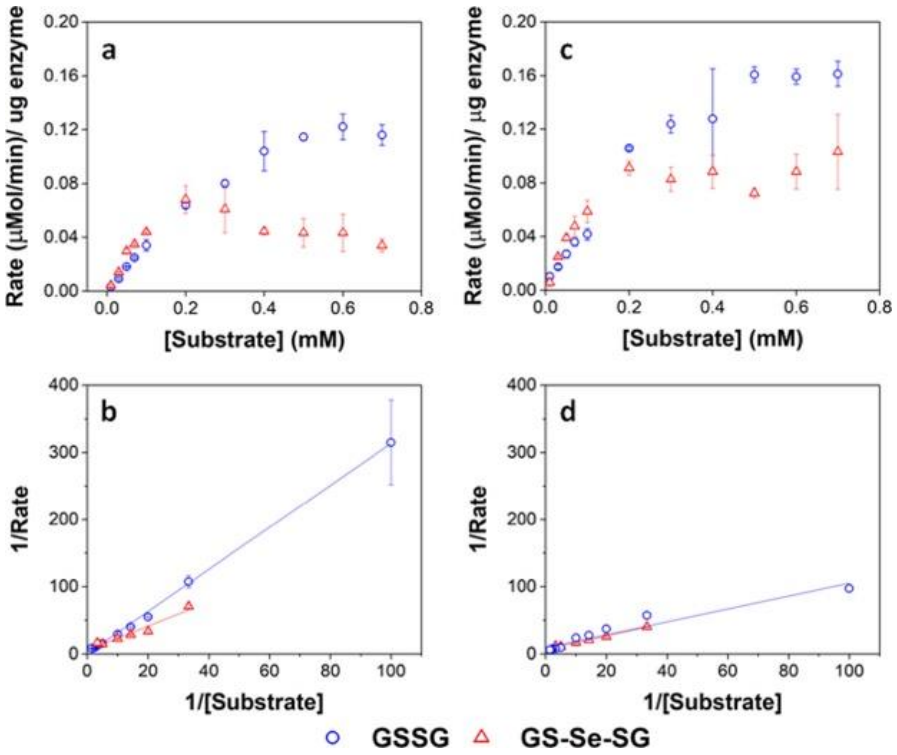

Figure 4.7. Enzyme kinetic assays for GRLMR (panel a) and GSHR (panel c). Lineweaver-Burke plots for GRLMR (panel b) and GSHR (panel d). The drop in rate at high concentrations of GS-Se-SG is attributed to SeNP formation interfering with the optical assay.

The 25-fold difference in K_M values for the enzyme from P. moraviensis stanleyae suggests that the enzyme is adapted for reducing GS-Se-SG. Therefore, we named this enzyme "Glutathione Reductase-Like Metalloid Reductase" (GRLMR) due to its substrate preference.

Another difference between GRLMR and GSHR enzymes is the lack of a substrate binding pocket cysteine or methionine residue on GRLMR that might serve as a locus for glutathionylation. Baker's yeast GSHR, a canonical GSHR enzyme, can be glutathionated at C239, resulting in inhibition of the enzyme[194]. Similarly, E. coli and Homo sapiens GSHR contain a methionine residue in this position, which might also be glutathionylated. This is thought to be a regulatory mechanism. In

GRLMR, homology models show that this residue is a serine residue, which cannot be glutathionylated (Figure 4.8). The absence of GSH based inhibition of GRLMR also suggests that this enzyme is distinct from canonical GSHR enzymes.

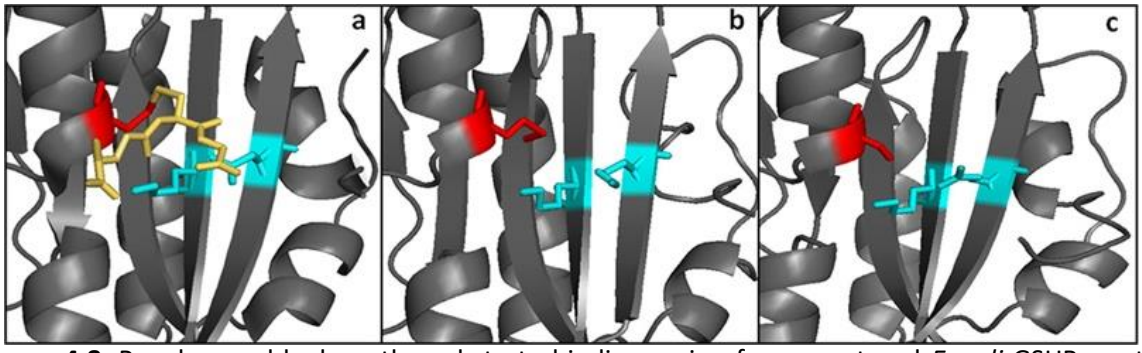

Figure 4.8. Panels a and b show the substrate binding region from yeast and *E. coli* GSHR crystal structures. Panel c shows the same region for a homology model of GRLMR. The residue shown in red is glutathionylated in panel a. In panel c, the red-colored residue is not capable of being glutathionylated.

Expression of GRLMR in E. coli confers selenium recombinant selenium tolerance to its host species. In the presence of mM concentrations of selenite, GRLMR creates nanoparticles to impart selenium tolerance for the cells (Figure 4.9). In our testing, we defined selenium tolerance as the amount of selenium required to inhibit 90% of cell growth (IC90). By testing for the IC90 of SeO_3^{2-} in laboratory strains of Escherichia coli, cells with the GRLMR gene had an IC90 of 21.3±9.8 mM, whereas without GRLMR, the IC90 was 1.89±0.46 mM. We observed a similar increase in Se tolerance for the SS320 strain of E. coli. The ten-fold higher Se tolerance when GRLMR was expressed was interpreted as imparting Se tolerance. Notably, GRLMR expressing cells grew poorly unless they were supplemented with 1 µM selenite. This was interpreted as GRLMR scavenging Se to the point that cells were Se deficient.

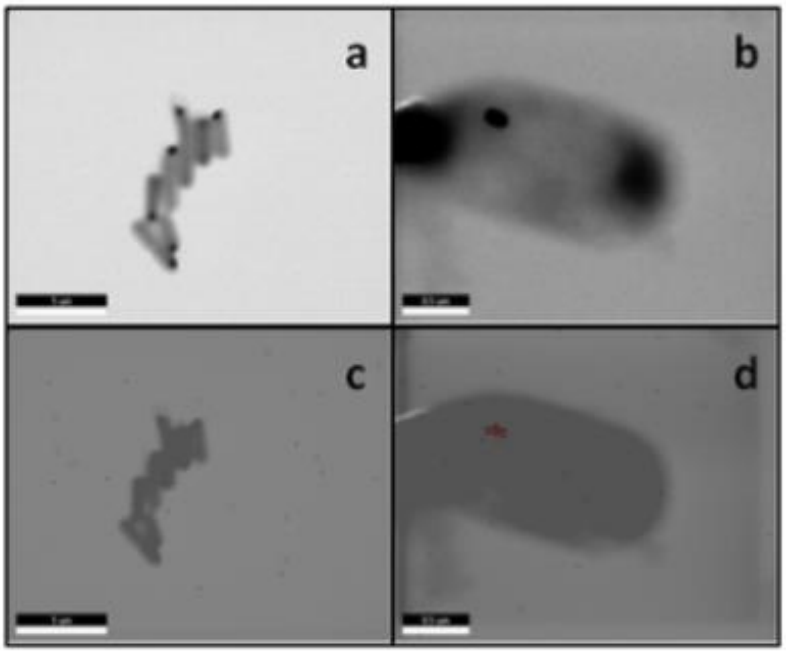

Figure 4.9. Panels a-d show SEM images of fixed BL21 E. coli. Panels a and c show cells without the GRLMR plasmid, whereas panels b and d show cells that include the plasmids that are expressing GRLMR. Panels c and d show EDS overlay, where areas that are mapped to Se are colored red.

For our ultimate goal of creating cNPs useful in EM imaging of cells, it is critical that the enzyme that synthesizes the SeNP also bind to the SeNP that it has made. We observe that about 10% of GRLMR enzymes are associated with SeNPs in pull-down assays (where the mass of the SeNP allows SeNPs and associated proteins to be collected by centrifugation). This small association makes sense—an efficient enzyme is likely to turn over its product and not be associated with the product. In fact, we observe that ~20% of baker's yeast GSHR is SeNP associated after SeNP synthesis. The smaller fraction of GRLMR associated with SeNPs is additional evidence for the specialization of this enzyme for SeNP production.

Overall, the GRLMR enzyme accomplishes reduction of a cellularly ubiquitous and essential element, Selenium. However, the SeNPs are quite polydisperse in size and do not remain attached to the enzyme that made them. To make a cSeNP, the GRLMR enzyme needs modification.

4.2.4 *Metalloid Reductase Activity Modified by a Fused Se^0 Binding Peptide*[120]

In the paper, we describe the isolation and activity of a SeNP binding peptide. When concatenated to GRLMR, this peptide changes the activity of the enzyme so that it controls SeNP size and SeNPs remain largely associated with the enzyme.

A SeNP binding peptide (SeBP) was isolated from the New England Biolabs Ph.D. 12-mer phage display library (NEB Ph.D. Kit) after three rounds of selection versus 8.4±2.7 nm SeNPs, whose size was confirmed via TEM. Following three rounds of selection, the output phage peptide library was found to be dominated by two sequences (Table 4.1). The sequence that appeared at the highest frequency (LTPHKHHKHLHA) was designated as SeBP and was used for future experiments.

Table 4.1. Sequences identified after three rounds of selection versus GRLMR-synthesized SeNPs. Sequences are described by population frequency, isoelectric point, and the amount of phage expressing the peptide sequence that bound to the three negative screen conditions (BSA, unreacted GRLMR, and SiNPs). Each titer began with an initial phage titer of 1010 pfu.

	Pep. Seq.	Frequency	pI	Polystyrene	GRLMR	SiNP
	Wild Type	N/A	N/A	$3.9x10^4$	$1.5x10^5$	$1.8x10^6$
SeBP	LTPHKHHKHLHA	19/33	9.37	$3.7x10^4$	$2.6x10^5$	$3.0x10^5$
SeBP2	GPHHMHHHRTHH	7/33	10.47	$1.1x10^6$	$2.1x10^5$	$7.9x10^6$
SeBP3	WPRHHNHTNYMP	1/33	11.15	$2.3x10^6$	$3.9x10^6$	$1.3x10^6$
SeBP4	GMRSPRAHWRVK	1/33	10.61	$4.3x10^4$	$3.3x10^5$	$3.7x10^5$
SeBP5	THYNPLRINPIT	1/33	9.95	$9.8x10^5$	$6.8x10^5$	$1.8x10^6$
SeBP6	KVHIMHPHHHSL	1/33	9.08	N/A	N/A	N/A
SeBP7	HSWSTIKRIETM	1/33	9.07	N/A	N/A	N/A
SeBP8	WPHLQHHEATSR	1/33	10.61	N/A	N/A	N/A
SeBP9	HDRMTKSSPSPP	1/33	9.07	N/A	N/A	N/A

Subsequent experiments explored the effect of concatenating SeBP to GRLMR (GRLMR-SeBP) versus GRLMR alone in terms of nanoparticle size, enzyme-nanoparticle binding, and enzyme activity. It was discovered that GRLMR-SeBP exerted control over the size of nanoparticles formed. SEM images of nanoparticles formed using 40 mM, 1 mM, 5 mM, and 10 mM SeO32- revealed that GRLMR-SeBP formed smaller and less polydisperse sized particles (Figure 4.10). For GRLMR, particle size varied with SeO32- concentrations such that at low concentrations SeNPs were smaller, and at high concentrations particles

were larger. However, the GRLMR-SeBP construct synthesized ~35 nm diameter particles independent of SeO32- concentration at the physiologically relevant SeO_3^{2-} concentrations of 40 mM to 5 mM. This demonstrates that the SeBP exerts remarkable control over SeNP size.

To compare the abilities of GRLMR-SeBP versus GRLMR to bind SeNPs, two different centrifugation assays were performed. In the first centrifugation assay, SeNPs were enzymatically synthesized, and centrifugation was then used to remove SeNPs from solution along with any associated enzyme. The percentage of bound enzyme was determined by measuring the protein concentration in the soluble fraction after precipitation. It was found that 83.1±1.0% of GRLMR-SeBP was bound to SeNPs, while 14.4±2.6% of GRLMR was bound to SeNPs (Figure 4.11). This demonstrates that concatenation of SeBP to GRLMR improves nanoparticle binding affinity.

In the second centrifugation assay, SeNPs were abiotically synthesized using $NaBH_4$ reduction; the percentage of bound enzyme was again determined by measuring the protein concentration in the soluble fraction after precipitation. GRLMR-SeBP preferentially binds smaller

SeNPs (30 nm or 50 nm) compared to larger SeNPs (125 nm or 900 nm). This indicates that there is an intrinsic preference of GRLMR-SeBP to bind SeNPs that are close to the typical SeNP size formed by enzymatic reduction. These results demonstrate that GRLMR-SeBP forms smaller and more monodisperse SeNPs than GRLMR. The results also demonstrate that concatenating SeBP to GRLMR improves the binding affinity for smaller SeNPs.

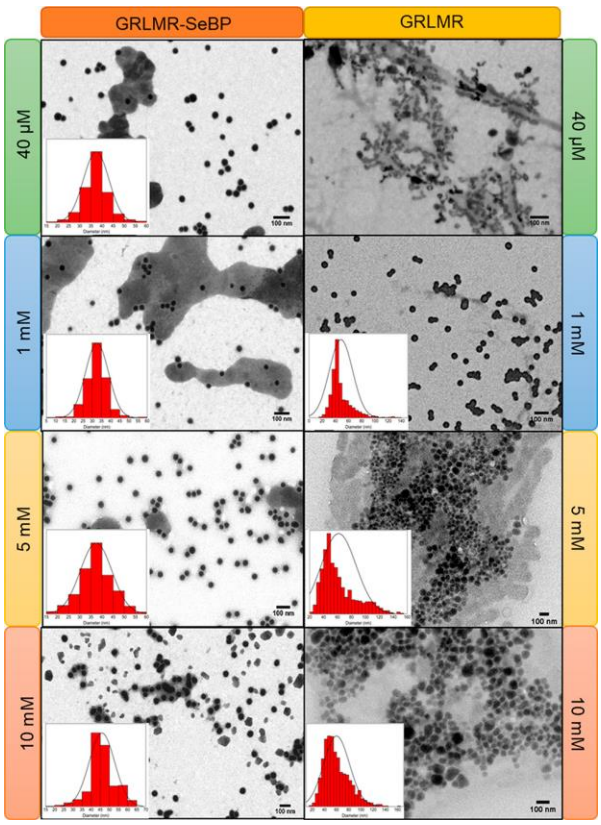

Figure 4.10. SEM images of nanoparticles formed using GRLMR-SeBP or GRLMR at indicated concentrations of SeO_3^{2-}. A histogram of the size distributions is shown where it could be determined.

Raman spectroscopy was used to monitor peptide conformation in both free and SeNP bound states. The interpretation of Raman spectra suggested that the SeBP peptide is unstructured in the absence of SeNPs. In the presence of SeNPs, the peptide's Raman signature changes to reflect spectra typical of a β-sheet conformation. Finally, the enzymatic activities of GRLMR versus GRLMR-SeBP were measured by spectroscopically monitoring NADPH depletion during enzymatic reactions. It was found that the K_M is significantly lower for GRLMR-SeBP than GRLMR alone when $HNaSeO_3$ was used as the substrate (0.22±0.06 mM versus 1.92±1.28 mM). Additionally, the k_{cat} was significantly higher for GRLMR-SeBP than GRLMR when using $HNaSeO_3$ as the substrate (40±2 min^{-1} versus 23±9 min^{-1}).

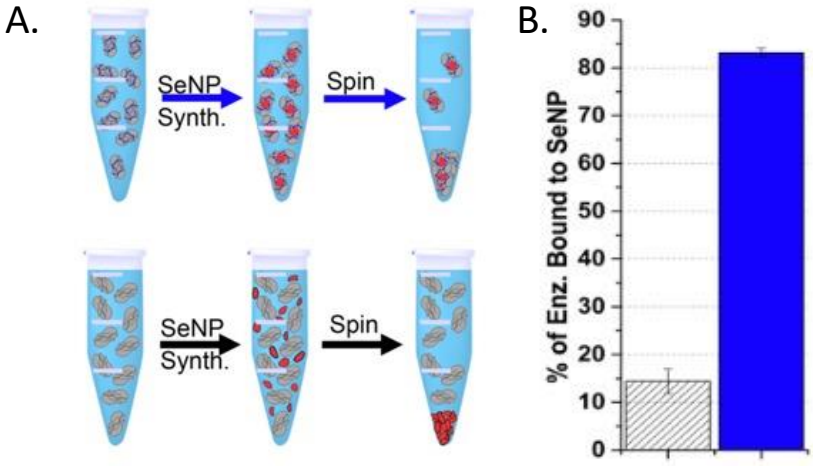

Figure 4.11. (a) Overview of the centrifugation assay used to assess enzyme-nanoparticle binding, (b) Percentage of enzyme that remained bound to nanoparticles following centrifugation for GRLMR (diagonal stripe) versus GRLMR-SeBP (blue).

When GSSG was used as the substrate, the measured K_M or k_{cat} values were not significantly different for GRLMR versus GRLMR-SeBP (Figure 4.12). These results indicate that concatenating SeBP to GRLMR leads to a more favourable enzyme-substrate complex and faster enzyme activity when selenite is used as the substrate. A possible reason for the increased enzyme-substrate stability and faster enzyme activity is that SeBP preconcentrates selenite near the active site. This could be due to the introduction of five positively charged histidine residues near the active site.

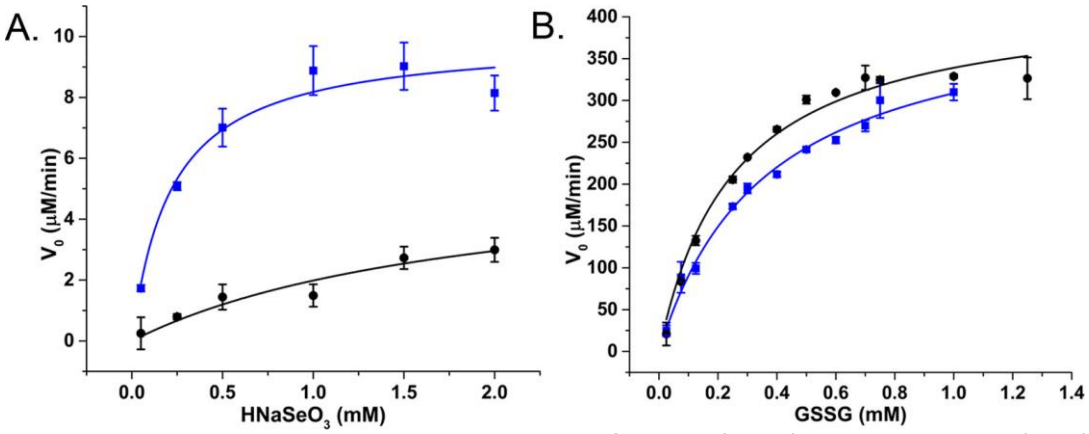

Figure 4.12. V_0 plotted against substrate concentration of GRLMR (black) and GRLMR-SeBP (blue) using (a) HNaSeO3as a substrate, (b) GSSG as a substrate.

Overall, the GRLMR-SeBP construct appears to constitute a cloneable SeNP (cSeNP). This construct selects the element (Se) from a background containing many metal(loid) ions; the construct reduces the Se in an NADPH dependent process to form Se precipitates of the red allotrope of Se(0). The SeBP arrests the particle size at a consistent size. Therefore, this construct—which is encoded in DNA—makes 35 nm diameter, spherical red Se nanoparticles that remain associated with the construct.

Assessment of molecular imaging with this cSeNP construct is ongoing and the cSeNP appears effective—localizing SeNPs to the expected intracellular positions of the proteins to which cSeNP is genetically concatenated.

4.2.5 *Motivation for "Multi-Color" cNPs*

Above is the 'story of a cSeNP'. For our goal of creating cNPs for imaging applications, multiplexed, simultaneous tagging of different proteins with distinguishable tags is a longer-term goal. Fluorescent proteins that were originally isolated as green (e.g., GFP) were subsequently evolved in laboratories to emit different colors (red, yellow, etc.)[187]. The multiple colors of fluorescent protein now enables multiplexed imaging of multiple proteins of interest, each labeled with a different color of fluorescent protein. Similarly, multiple cNP proteins, each producing a distinguishable cNP, comprise a panel of cNPs that enable multiplexed tagging of proteins of interest.

Inorganic NPs can be distinguished in EM on the basis of their elemental composition, size, and/or shape. For other modalities like X-ray imaging, elemental composition of the cNP may be the chief means of distinguishing different cNPs. The basis for distinguishing different elements in EM and X-ray imaging modalities may be as simple as elemental electron density (for instance, it is straightforward to distinguish Au and Ag NPs using TEM, where Au NPs simply have notably higher contrast). However, more sophisticated spectroscopic methods such as EDS and electron energy loss spectroscopy (EELS) can also map elemental compositions in TEM[195,196]. In X-ray imaging, X-ray fluorescence methods may allow elemental mapping (although the resolution may be low) and tuning the X-ray wavelength to absorption

edges of particular elements can also distinguish different elements, although variable wavelength X-rays require specialized X-ray sources such as synchrotrons.

In this context, we are working to make size/shape or elementally distinct cNPs. Most of our work to-date has been toward making elementally distinct cNPs.

4.2.6 *Identification of a TeO_3^{2-} reductase/mycothione reductase from Rhodococcus erythropolis PR4.*[2]

In this paper, we began by collecting environmental samples from abandoned mine sites in Clear Creek County, Colorado, USA. Mining in this region dates to the 1851 Colorado Gold Rush, and most mines have not been active for over a century. Many of these mines leach mine runoff that carries substantial metal contamination.

The environmental sampling was facilitated by the Clear Creek Watershed Foundation—a nonprofit organization dedicated to the cleanup of mine sites in Clear Creek County, whose mine runoff contaminates Clear Creek with toxic metals.

Here, we worked under the hypothesis that microorganisms that survive in normally lethal concentrations of toxic metals may reduce these metals to zerovalent form as a means of detoxification. One of the isolates from this sample collection was able to grow on LB-Agar that contained normally lethal concentrations of Fe(II), Cu(II), AsO_3^{2-}, SeO_3^{2-}, TeO_3^{2-}, Cd(II) and Zn(II).

To discover any inorganic oxidoreductases involved in this remarkable set of metal tolerances, we followed the same procedure that we used to isolate GRLMR from the Se specialized *P. moraviensis* stanleyae. This involves first fractionating all soluble proteins on one or more non-denaturing gels, then staining gels with different metal salts and enzyme cofactors, and finally performing proteomic mass spectrometry analysis on any bands that appear from combinations of enzyme cofactors and metal salts to identify enzymes that may have precipitated the metal salts.

Figure 4.13 shows the results of this screening for metal(loid) reductase activity in this isolate. Among the inorganic ions tested, only TeO_3^{2-} was enzymatically reduced in-gel (Figure 4.13, panel A).

Proteomic mass spectrometry revealed 13 proteins associated with the precipitate, 4 of which are NAD(P)H dependent enzymes (Figure 4.13, panel B). Of those enzymes, we judged the mycothione reductase to be of the greatest interest because it belongs to the same class I pyridine nucleotide-disulphide oxidoreductase enzyme family as GRLMR and mercuric reductase. Notably, mycothione reductase fills a similar role as glutathione reductase; in mycothione containing organisms, mycothione is used to establish redox balance—whereas in most organisms, GSH accomplishes this.

(B)

MS Identified Proteins	M_W
Putrescine Oxidase	*49 kDa*
β-ketoadipyl-CoA Thiolase	42 kDa
Mycothione Reductase	*49 kDa*
Malate Dehydrogenase	*41 kDa*
Aminopeptidase N	91 kDa
Superoxide Dismutase	23 kDa
Enoyl-CoA Hydratase	27 kDa
Thioredoxin Reductase	*35 kDa*
3-hydroxyisobutyrate Dehydrogenase	*30 kDa*
RNA Polymerase Subunit α	38 kDa
Zinc-Dependent Metalloprotease	50 kDa
Metallo-hydrolase	48 kDa
Phosphoenolpyruvate Carboxykinase	67 kDa

Figure 4.13. (a) Native PAGE gel sections incubated in indicated metal(loid) ions and NADPH. The arrow indicates reduced insoluble TE0 particulate. Cu(II) was precipitated in gel with and without protein. (b) Proteins associated with the excised Te(0) by LC-MS/MS. Entries in italics indicate the presence of an NAD(P)H binding domain.

Mass spectrometry identified the organism as *Rhodococcus erythropolis* PR4. The genome of this organism was already sequenced and available in published sequence databases. We used the existing genomic information to determine the sequence of the mycothione reductase, and then expressed and purified this enzyme recombinantly from BL21 E. coli.

In *in vitro* experiments, the mycothione reductase was found to have significant selectivity for tellurite over selenite. This was surprising because the oxyanions are very similar, and the reduction potential for selenite makes it easier to reduce than tellurite. The standard reduction of potential for the

reaction TeO_3^{2-} + 3 H_2O + 4e^- ← → Te + 6 OH^- is −0.57 V vs Hydrogen. The corresponding reduction of SeO_3^{2-} is −0.366 V. Thus, SeO_3^{2-} is the preferred substrate for reduction in the absence of a mechanism for substrate selectivity.

This selectivity for Te over Se was quantified in assays in which both TeO_3^{2-} and SeO_3^{2-} were present in different molar ratios. Figure 4.14 shows that in equimolar concentrations of Te and Se, the enzymatic precipitant incorporated 7 tellurium atoms for each selenium atom as determined by inductively coupled plasma mass spectrometry analysis. Even when selenium was present in a 10-fold excess to tellurium, the enzymatic products incorporated tellurium in an almost 2:1 ratio.

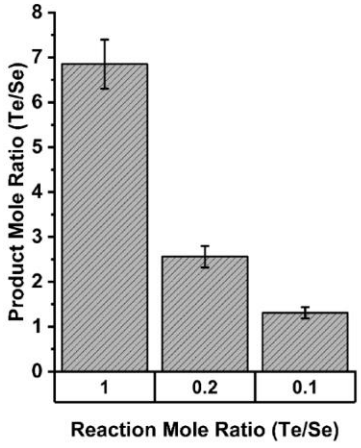

Figure 4.14. Elemental composition of precipitates resulting from enzymatic reactions in indicated ratios of tellurite and selenite as determined by ICP MS.

This selectivity was found to depend on pH. Assays done at pH values of 6, 7, 8 and 9 showed the greatest discrimination between tellurium and selenium at pH 6, with decreasing selectivity as pH rises (Figure 4.15).

In this paper, we postulated a mechanism for selectivity of tellurium over selenium by the mycothione reductase which we now view as flawed. Here, we postulate what we believe to be a more plausible mechanism for enzymatic preference of Te over Se.

A homology model for the structure of mycothione reductase was generated with Phyre2. This homology model was subsequently aligned with GRLMR in Pymol to show mutations which may contribute to the observed substrate specificity.

Several notable mutations in mycothione reductase are located in an apparent cavity that is oppositional to the putative substrate entry channel of GRLMR. Four of the seven mutations within this region result in aromatic residues for mycothione reductase, with several of these residues being Histidine.

This set of aromatic residues may contract the immediately surrounding region through π-π stacking interactions; this contraction may expand the substrate entry channel, accommodating of TeO_3^{2-}, which is a larger substrate than SeO_3^{2-}. The protonation of the histidine residues at lower pH values is implicated in this structural rearrangement by the pH dependence of the observed selectivity.

In summary, we isolated a Class I pyridine nucleotide-disulphide oxidoreductase that is specialized for tellurite reduction. This is a curious finding because tellurite reduction is energetically more difficult than selenite reduction, and selenite and tellurite are otherwise very similar oxyanions. This enzyme currently represents a lower priority for our adaptation to a cNP purpose because of the toxicity of tellurium. However, it is attractive for adaptation because mycothione is not present in most cells, meaning TeO_3^{2-} will not be competing with mycothione as a substrate. (In our testing, the mycothione reductase did not act upon oxidized glutathione in any detectable manner.)

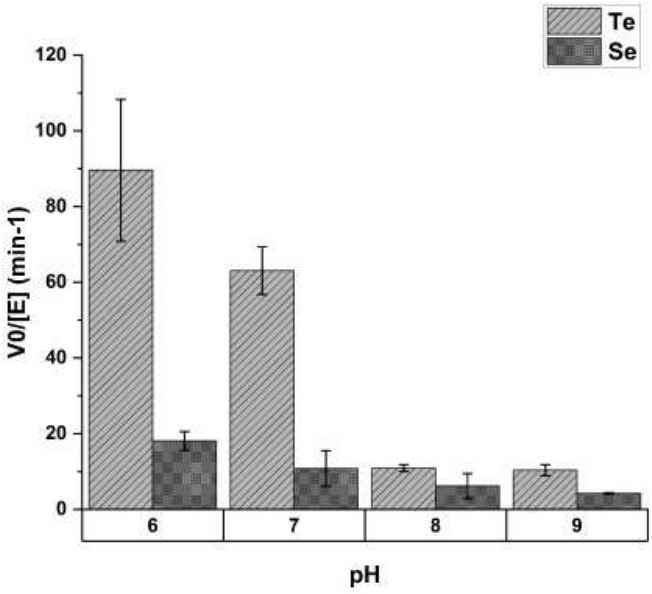

Figure 4.15. The effect of pH on mycothione reductase substrate selectivity; Y-axis shows initial velocity of mycothione reductase with tellurite or selenite. Each substrate was present at 2 nM.

4.2.7 *Enzyme-Catalyzed in Situ Synthesis of Temporally and Spatially Distinct CdSe Quantum Dots in Biological Backgrounds*[145]

Metal chalcogenide semiconductor nanoparticles are often referred to as quantum dots. This naming reflects the observation that electrons within semiconductor nanoparticles behave like a quantum particle in a box. Quantum dots can be very bright luminescent emitters with quantum yields over 90%. This makes quantum dots attractive as potential luminescent labels in optical or fluorescence microscopy.

Many semiconductor nanoparticles are made as metal-selenides, for example, CdSe. In this paper, we found that when Cd^{2+} ions are included in the synthesis of SeNPs by GRLMR, what results are luminescent CdSe nanoparticle quantum dots, instead of the non-emissive SeNPs that we made previously. Therefore, GRLMR joins cystathionine γ-lyase from *Stenotrophomonas maltophilia*[115,116] and nitrate reductase from *Fusarium oxysporum*[197] in a category of enzymes that generate active monomers to help mediate metal nanoparticle growth.

In prior papers that identified enzymes that synthesize quantum dots, a general theme is that the enzymes generate dianionic chalcogenides (e.g., S^{2-} from cysteine). These dianionic chalcogenides then crystalize with dicationic metals (e.g., Cd^{2+}). The resulting nanocrystals comprise quantum dots.

Following this rationale, we hypothesized that GRLMR might reduce GS-Se-SG (where Se's oxidation state is +2) to Se^{2-}. The Se^{2-}ions could then crystallize with any Cd^{2+} forming fluorescent semiconductor nanocrystals. This rationale is summarized in Figure 4.16. In this rationale, the presence of dissolved oxygen oxidizes Se^{2-} to Se(0) which forms the usual observed SeNP product of GRLMR. Evidence for this hypothesis arises from the observation that the QDs only form when oxygen is excluded from GRLMR catalyzed SeNP synthesis in the presence of Cd^{2+}.

Much of this paper describes mechanistic work showing that while GSH can also reduce SeO_3^{2-} to Se(0) and Se^{2-}, the rate of this process is slow compared to the enzymatic process. Overall, this paper shows that GRLMR can be used to form CdSe semiconductor quantum dots. This is appealing because of the possibility of making cNPs that are both electron dense and fluorescent. Such a tool is useful in the emerging field of CLEM—where fluorescence microscopy images are used to determine which parts of a sample should be examined at high resolution by EM, and which parts are of less interest.

4.2.8 *Other Approaches to Cloneable Contrast in EM*

In addition to the cNP approach, we have attempted to form cloneable contrast agents from the naturally occurring metal handling proteins Dps and metallothionein. The Dps approach failed completely and has never been published. The metallothionein approach functions in the limited circumstances of high-copy number proteins in fixed cells, as outlined below.

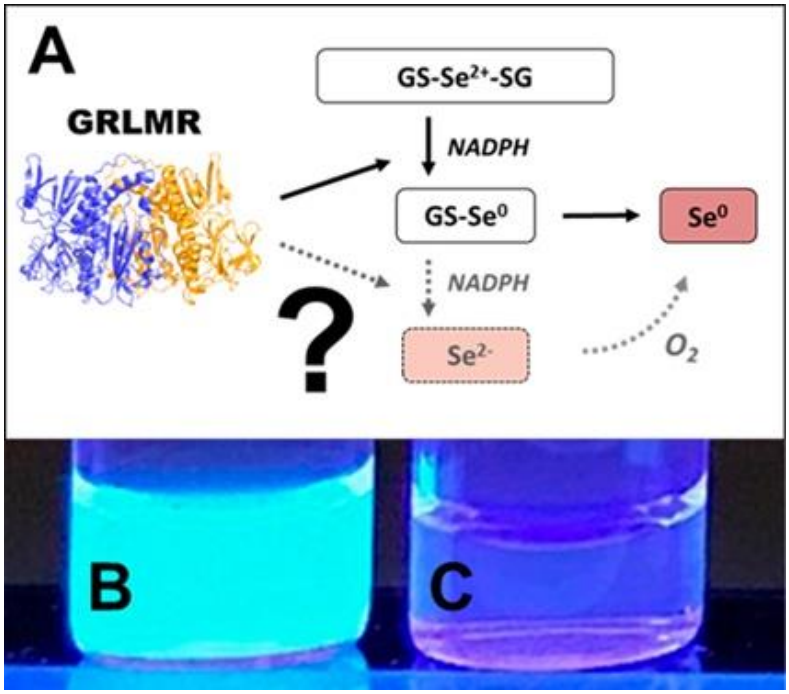

Figure 4.16. (A) Sketch of suggested selenite reduction pathway via GRLMR. Fluorescence can be visualized through UV illumination of particles formed by reduction of Se^{2+} to Se^{2-} by GRLMR with Cd^{2+} present in (B) air-free conditions and (C) in atmosphere.

4.2.9 *Metallothionein as a cloneable tag for protein localization by electron microscopy of cells*[37]

We explored the use of metallothionein as a cloneable contrast tag. Metallothioneins are small cysteine rich proteins belonging to the broader class of phytochelatins. Such proteins are naturally expressed during heavy metal stress to most cells. The cysteine-rich proteins chelate metal ions, helping to sequester and reduce toxic effects of metals. There is some prior history of investigation of metallothionein as a cloneable contrast agent by others.

Previous studies demonstrated by mass-spectrophotometric measurement that metallothionein can capture enough gold atoms to theoretically be visible in cellular electron microscopy. Metallothionein can achieve this function when conjugated to a protein.[189] These studies increased the appeal of metallothionein as a cloneable contrast tag but did not demonstrate success in imaging.

We do not define cloneable contrast tags formed by metallothionein as a biogenic cNP for three reasons. First, these tags are essentially inorganic coordination complexes—which are not classically

'particulate'—even as they may appear as such in an electron microscope. Second, the chemistries developed that allow successful imaging of metallothionein are incompatible with living cells; more specifically, the chemistries developed here use Au^{n+} salts, which are quite reactive with living cells. Finally, a cNP can be modified by altering the DNA encoding the cNP. In an approach where the underlying chemistry is stoichiometric binding of metal ions to cysteine, the only way to modify the construct to modify metal activity is adding or removing cysteine residues to the protein. This manipulation is only able to modify the number of metal ions coordinated—i.e., changing the DNA cannot dramatically modify materials properties such as elemental composition, crystal structure, size, or shape.

Nonetheless, metallothionein is appealing for potential applications as a cloneable contrast tag, whose electron scattering properties could be enhanced post-fixation and before EM imaging.

In this study, we attempted to label several proteins, which provided an assessment of how well metallothionein performed as a cloneable contrast tag. Metallothioneins range in weight from 0.5-14 kDa, which satisfies the requirement of a small-size tag. To assess the ability of metallothionein to label proteins with a high copy number, wild-type desmin (a filamenting protein) was tagged with a single metallothionein and expressed in bacteria. After desmin was freeze-substituted and treated with aurothiomalate, the metallothionein-labeled desmin showed staining with small particles. Furthermore, this type of staining was not seen in the wild-type desmin, which indicated that the staining was due to metallothionein and that the staining resulted in a good signal to noise ratio (Figure 4.17).

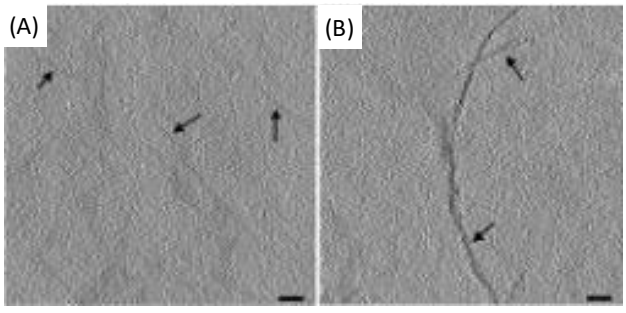

Figure 4.17. Tomographic slices of (A) wild-type desmin (B) metallothionein -labeled desmin. Scale bars = 100 nm.

To assess the ability of metallothionein to localize a tagged protein in the complex environment of a cell, an SPC42 protein product was tagged with two copies of metallothionein. SPC42 is a component of the yeast spindle pole body and is located approximately at the plane of the nuclear envelope. It was found that following the same procedure as followed for desmin did not yield adequate signal. Instead, use of a Nanoprobes gold enhancement kit was required (Figure 4.18). To this point, sections were stained with aurothiomalate after freeze substitution. Therefore, staining during the process of freeze substitution was assessed next.

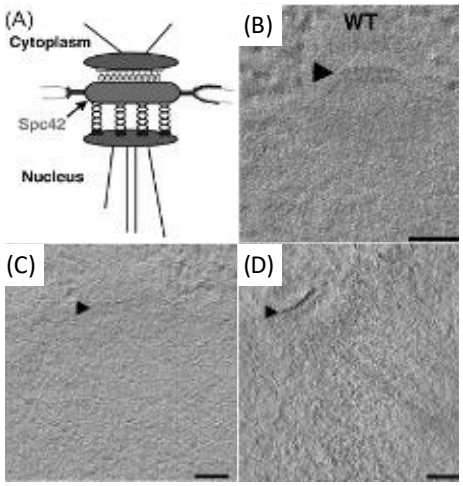

Figure 4.18. (A) Diagram of spc42; the metallothionein tag was added to the C-terminus. (B) Tomographic slices of wild-type spc42. Tomographic slices of Spc42-2x metallothionein (C) incubated with aurothiomalate alone, and (D) first stained with aurothiomalate followed by enhancement with the Nanoprobes gold enhancement kit. Scale bars = 100 nm.

It was found that the best signal was achieved by first staining sections with $Au(III)Cl_3$ during freeze-substitution, then treating samples with diglyme, and finally enhancing using a silver enhancement protocol[198]. Control samples not tagged with metallothionein did not show staining, regardless of whether they underwent the diglyme and silver enhancement protocol. However, metallothionein tagged samples that underwent staining during freeze-substitution, diglyme treatment, and silver enhancement showed strong labeling, which allowed single particles to be detected (Figure 4.19). The studies using desmin and spc42 provide evidence that metallothionein can reveal the location of proteins with many copies localized to a small area.

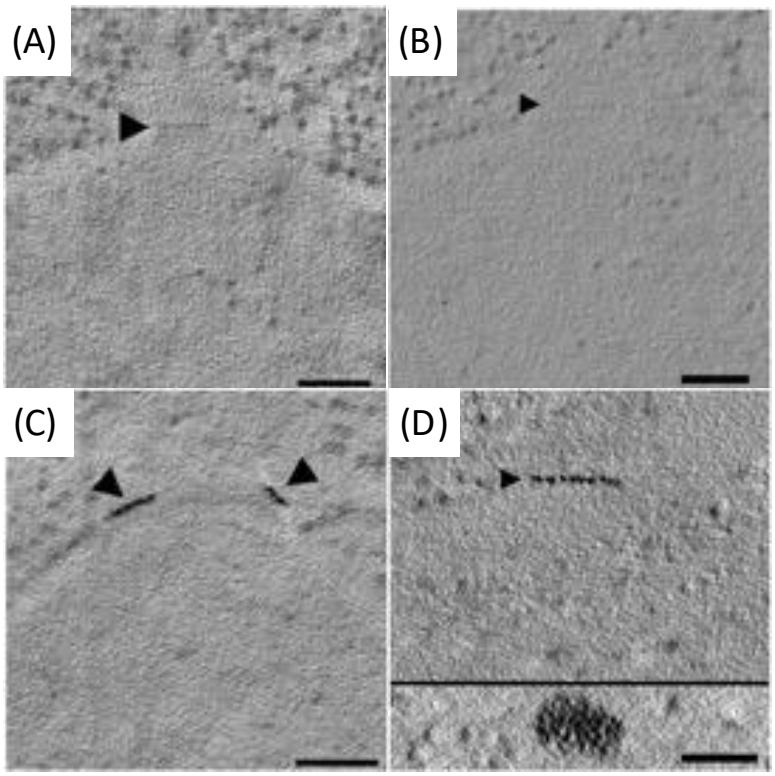

Figure 4.19. Staining of wild-type spc42 during freeze substitution (A) without diglyme treatment and silver enhancement and (B) with diglyme treatment and silver enhancement. Staining is not observed in either condition. Staining of Spc42-2xMTH sections (C) without diglyme and silver enhancement and (D) with diglyme treatment and silver enhancement, which allowed for the detection of particles (D, inset). Scale bars = 100 nm.

To assess the capabilities of metallothionein as a tag for low-copy number proteins, protein components of the nuclear-pore complex were tagged with metallothionein and stained. No staining of the nuclear pore complex was observed, although many staining and enhancement protocols were attempted.

Despite unsuccessful attempts to stain components of the NPC, the successful applications of metallothionein to stain both desmin and spc42 demonstrates the potential of metallothionein as a cloneable contrast tag in fixed cells.

Overall, this paper shows that metallothionein can be effective to localize high copy number proteins that are concentrated in specific areas, such as filamentous or ultrastructural proteins. For low copy number or isolated proteins, metallothionein does not appear effective. These approaches with

metallothionein also require that cells are fixed before metal incubation and are therefore somewhat limited compared to the cNP platform approach, which can use essential elements to form high contrast particles in live cells.

4.2.10 *Dps as a cloneable tag*

Iron oxide encapsulating proteins such as ferritin and Dps create iron oxides that can be identified in electron microscopy. Ferritin has been investigated as a cloneable tag[3]. Ferritin is comprised of 24 protein subunits that assemble into a capsule which can contain an iron oxide core of up to ~8nm in diameter. Concatenating a ferritin subunit to a protein of interest at the DNA level can cause a ferritin capsule to become attached to that protein of interest. This approach has not become widely used because several proteins of interest can become integrated into a single ferritin capsule. This cross-linking, as well as the sheer size of ferritin, are likely to cause artifactual observations around the localization of the protein of interest.

An improvement on this approach may be to use Dps, which is sometimes described as a mini-ferritin. Dps is a capsule protein comprised of 12 subunits, which can contain an iron oxide mineral up to ~4 nm in diameter, which can be visualized in cells. A 'single-chain' Dps—where up to 12 Dps protomers are linked with a flexible linker sequence at the DNA level is in principle possible.

Our work on Dps involved making the DNA that encodes Dps from 12 Dps protomers, each linked by a flexible linker. Despite many attempts, we were unable to express functional Dps as a 12-mer, 6-mer, 4-mer or 3-mer construct. For now, we hypothesize the linker that we chose may have been incompatible with DPS folding and therefore function. We hypothesize that different linkers might allow DPS protomers to be linked into functional units, using modern computational protein folding assessment tools to identify successful linkers.

4.3 Outlook and Future Directions for cNPs

As a field, synthetic chemistry aims to develop and improve methods for creation of well-defined molecules and materials. The synthetic chemistry sub-field of organic synthesis is particularly impressive in this regard, with well-developed methods for discrete addition or removal of atoms to defined locations in complex molecules. Cyclization reactions, solid phase synthesis and enantioselective control, among other tools, facilitate the precision synthesis of carbon-rich products including pharmaceuticals, oligonucleotides, and plastics.

Outside of organic synthesis, precise 'magic number' nanoclusters are now routinely made with atomic precision and resulting defined structure, up to about ~500 metal atoms. These nanoclusters are already used as extrinsic biological contrast agents, catalysts, and their continued synthetic exploration allows advancement of fundamental knowledge of cluster physics. Improved control over bNP synthesis is a logical (and destined) progression.

Research on Biogenic NPs appears to be currently in a "gold rush" era, with sharply growing numbers of active researchers and publications (Figure 4.20). These publications include those that address fundamental aspects of nanoparticle chemistry, new synthetic routes, and a wide variety of potential applications. The research area is presently highly interdisciplinary, with contributions coming from chemists, physicists, geologists, and microbiologists.

As the field of bNP synthesis and application continues to develop, we anticipate an increasing emphasis on synthetic precision—by analogy to the development of other synthetic chemistry sub-fields. We postulate that the cNP platform approach, which mixes and matches well-defined metal oxidoreductases and proteins and peptides that enforce NP shape, provides a robust approach to improving bNP precision and design. Biological evolution over eons has produced many examples of atomically precise/defined molecules. For bio-organic synthesis, biology often allows synthetic organic transformations that are difficult or impossible to achieve in vitro. It's an ambition of ours to push

bNP/cNP synthesis to achieve similar levels of atomic precision in nanomaterials synthesis, using well-defined biological approaches.

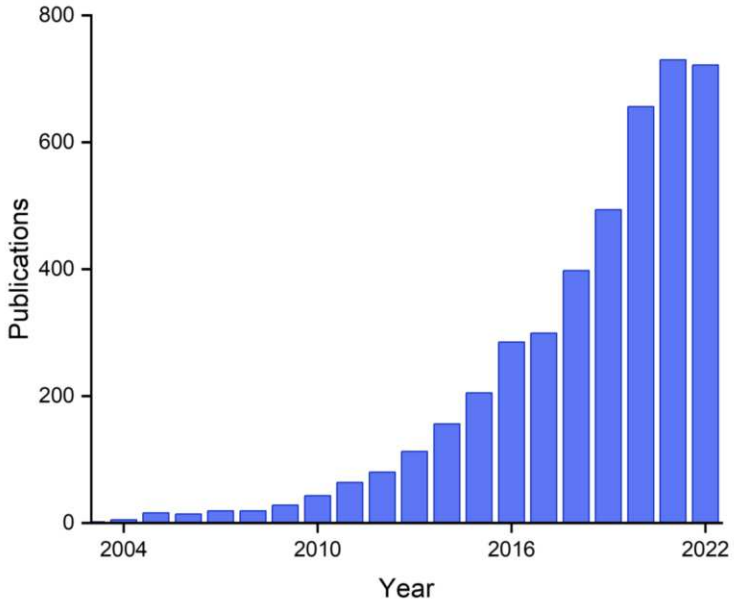

Figure 4.20. Papers on the topic of 'biogenic nanoparticles' per year, from Web of Science.

One way to conceptualize this approach is as an extension of the central dogma of molecular biology. This states that DNA contains all the information to create an atomically precise protein. To convert DNA information into protein function, the DNA is transcribed into RNA, which is then translated into functional proteins.

Extending this dogma to cNP synthesis, we suggest that DNA (information) can be transcribed into mRNA (information transfer) which is then translated into protein (translating information into function). The protein then creates a cNP, translating function into discrete synthetic product. This approach suggests the possibility of next-generation nanoscale materials where the synthetic information is not contained in journal-article text, but rather in DNA sequence.

Much in the same way that unnatural amino acid incorporation has expanded the "chemical space" that biology is allowed to partake in, so too will cNPs open the door to exploring new interfaces of

nanoscale inorganic nanomaterials and biosystems. As we approach this paradigm, we ask ourselves: what new and exciting things will be discovered?

cNP synthesis does have intrinsic limitations. Not every metal(loid) on the periodic table, for instance, is compatible with redox reactions that are biologically achievable. Elements with redox potentials outside the range of –1.0 V to 1.0 V relative to SHE will either be too favorable for controlled reduction or too unfavorable for any redox chemistry to occur at all. In the case of 'uncontrolled' reduction—oxidation of ubiquitous biomolecules such as sugars, tyrosine and tryptophan, and nucleobases by easily reduced elements is likely to be implicated. Such elements are likely to be reduced in nonspecific ways within biological matrices. Pourbaix diagrams describe expected redox potential versus pH and can help identify elements that are good candidates for inclusion in cNPs[155,199].

For our target applications in imaging, electron-rich (e.g., higher-Z) elements are the most attractive, as they provide greater contrast relative to the less electron rich elements of C, O, N, H and P that comprise most of the biological matrix. Based on these considerations, Zn, As, Te, Fe, Cd, Se, Bi and Co ions are of highest interest for cNP incorporation because of relatively favorable redox potentials and Z-values. We consider comparably toxic elements as lower priority choices. Although the cNP machinery may confer tolerance to elements such as Cd and Te, their intrinsic toxicity at small concentrations presents complications that are less pronounced for biologically essential elements such as Zn, Fe and Se, as well as elements that are generally less toxic such as Bi (a component in pharmaceuticals such as Pepto-Bismol). Bismuth is particularly attractive for our future work as it is the most electron-rich non-radioactive element on the periodic table.

Many metal(loid) oxidoreductases are comparatively large proteins. Class I pyridine nucleotide-disulphide oxidoreductases, including GRLMR, are typically ~100 KDa homodimers—before they are saddled with an attached inorganic nanoparticle[2,56,170,200]. For comparison, widely used fluorescent proteins like GFP are ~27 KDa monomers. GFP is well known to alter the biological activity of many of the

proteins that it is concatenated to, potentially resulting in artefactual observations[201,202]. It's hypothesized that larger 'tags' are more likely to alter biological activity of concatenated proteins; large size can hinder POI diffusion kinetics and position contrasting markers distally to the point of interest, whereas multimericity can convolute labelling efficiency. Therefore, one of our future directions in cNP synthesis is to develop smaller inorganic oxidoreductases.

We are investigating approaches for making GRLMR a functional monomer of decreased mass. Other metal(loid) oxidoreductase enzymes may be of interest as starting points for further engineering. For instance, a 27 kDa NADH-dependent cytochrome b_5 reductase was recently isolated from a strain of *Muchor racemosus*[203,204]; similar to GRLMR, the enzyme conveys nanoparticle-mediated metal tolerance to silver and palladium when cloned into laboratory microorganisms. Alternatively, arsenate reductase[171] may be amenable to engineering processes that alter its substrate specificity to metals other pnictides such as Bismuth.

It is possible that newfound and promising enzymatic systems may possess kinetics or substrate specificity that nullify their otherwise ideal characteristics (e.g., mass, stability, metal(loid) reduction, monomericity, etc.). Given the discrete genetic nature of cNPs, we offer the prospect of using directed evolution as a means of manipulating enzyme function to better serve the needs of cloneable contrast. Doing so will necessitate the development of robust selection methods for metal reductases, which is a relatively unexplored area.

4.4 Conclusions

In this feature-article, we have described the development of a cNP platform technology. Our main goal is to develop cNP based cloneable contrast agents for biological imaging. It is conceivable that our approach may one day result in a single cloneable contrast agent that allows imaging in many modalities (optical, fluorescent, electron, X-ray, magnetic imaging). We are also interested, to a lesser extent, in using cNP approaches for bioremediation of toxic metals.

The platform is not limited to applications in imaging and bioremediation. Rather, we expect that many applications explored for bNPs such as biomining and solar photoconversion might one day benefit from the increased precision of synthetic product made possible with the well-defined components of this platform and their intrinsic linkage to laboratory evolvable DNA sequences. The intracellular aspect of cNP synthesis further offers the prospect of integrating cNPs with other cellular processes to offer the prospect of cellular engineering to accomplish yet unimagined goals.

Manuscript adapted for dissertation submission[1]*. Author contributions:* ***ARH*** *(lead author), BG (2nd author), RC, GE, TT (co-authors), and CJA (principal investigator) wrote initial draft and edited. KMB (co-author) edited.*

CHAPTER 5: ENGINEERING THE NEXT GENERATION OF CLONEABLE NANOPARTICLES

5.1 Introduction

Cloneable contrast agents (i.e., protein tags) are routinely implemented to visualize cellular components (e.g., proteins) which are otherwise invisible or indistinguishable[25,35–37,150,205]. Contrast-enhanced visual data in turn enables more thorough interpretations and analyses, leading to a better understanding of biological systems. The degree of obtainable information pertaining to proteins-of-interest (POIs) and other cell components is nevertheless confined within the boundaries that cloneable tags are able to perform; where a cloneable tag is limited, so too will there be limitations in what can be inferred about chimeric POIs. The primary attribute of any cloneable tag is its ability to generate sufficiently contrasting signal from native cellular machinery; however, many other protein attributes are also important in dictating their usefulness across diverse applications.

Two of such primary attributes are **1)** the ability of protein tags (or a family of tags) to generate differential contrast in a controllable manner[195,206,207], and **2)** the extent to which protein tags affect the native behavior of their chimeric POIs[36,38]. The former generally pertains to the extent that multiple components (i.e., distinct POIs) can be visualized simultaneously within complex environments. The latter contributes to any endowed biases in the location/frequency of contrasting markers which arise from the inherent characteristics of protein tags rather than those of the studied POI.

Differential contrast is generally analogous to color in imaging contexts, which is an invaluable means of visually displaying information from multicomponent systems. For instance, differing colors allow players and viewers to readily distinguish teams in sporting events via jerseys. There is also generally a desire to reduce confounding factors which result from the use of contrast agents: imagine each jersey is so large and heavy that a player is unable to run across a field, or perhaps that each jersey might cause

players to aggregate uncontrollably. Contrast agents can have profound impacts on the systems they are being used to study.

Distinct colors from contrast tags can indicate specific molecules or tissue types at a subcellular level. On the other hand, contrast tag mass/size impacts the degree to which native behaviors of labeled components are affected. While magnificently colored cell images can be found in virtually any biochemistry textbook, underlying work which leads to an *accurate representation* of native chemistry often goes underappreciated. Such images are the product of many decades-worth of advancements in chemical contrast agents, instrumentation, and other imaging-related technologies. However, it is generally known that even well-developed contrast agents can lead to substantial imaging bias in modern studies[33,34,208]. Thus, the next generation of biological research necessitates continued development of multimodal cloneable contrast agents which minimally bias the systems they are being used to study.

Optical (fluorescence) microscopy is currently the primary means of obtaining multicolored cellular-level images. An expansive variety of multicolored protein fluorophores such as the 27 kDa green fluorescent protein (GFP) or cyan fluorescent protein (CFP) have been developed to the extent that they are ubiquitous[207,209]. It is currently 'mainstream' to label multiple POIs of a cell simultaneously within complex environments[206]. While powerful, optical techniques are resolution limited to hundreds or dozens of nm. And as is described in more detail in Chapter 1, super-resolution FM techniques which overcome the resolution limit are only able to resolve constituents which are labeled by fluorophores.

Biological electron microscopy (EM) is capable of visualizing an entire cell's ultrastructure at near atomic resolution yet lacks a toolkit analogous to multicolored fluorescent proteins[35]. Cloneable contrast agents are relatively unexplored in biological EM, multimodal cloneable contrast agents even less so. Greyscale micrograph images are conventionally associated with EM generated images; however, contrast markers can be distinguished analogously to colors according to several characteristics including relative morphology (shape and size), crystallinity, and elemental composition. Morphology can be

visualized by observation of relative size/shape of contrast markers. Crystallinity can be distinguished according to electron diffraction patterns of atomic lattice structures. Elements can be distinguished by observing characteristic X-rays emitted under electron bombardment through energy dispersive X-ray (EDX)[210] or relatively nascent electron energy-loss spectroscopy (EELS)[20].

There has been some preliminary work towards achieving 'colorful' cellular EM with cloneable contrast tags. Miniature singlet oxygen generator (miniSOG) and similar systems such as engineered ascorbate peroxidase (APEX2) can locally deposit highly contrasting osmiophilic diaminobenzidine (DAB) conjugated to chelated lanthanide atoms[195]. Here the osmiophilic polymer precursors are 'pre-stained' with 'colorful' lanthanide atoms which can be deposited in a temporally resolved manner. Polymerized DAB networks nevertheless diffuse dozens to hundreds of nanometers distally from their points of origination; although highly sensitive, DAB-precipitating systems inherently lack spatial resolution. Iron-storing ferritins of varying sizes have also been proposed as a means of generating multimodal contrast in EM. In one study, ferritin systems from two different cellular origins were distinguishable when expressed in mammalian cells due to their difference in relative size/particle radii[211]. While multimodality was achieved in this instance, ferritin-based contrasting markers are excessively large (~0.4 MDa) and multimeric (24 monomer units per marker), which severely restricts their application range. Metallothioneins currently have no established means of generating multimodal contrast within cellular contexts (although they are notably capable of binding several metal ion species)[37,189].

We have previously described cloneable nanoparticles (cNPs) as cloneable contrast agents which have the potential to overcome limitations associated with DAB-polymerizers, ferritins, and metallothioneins. cNPs are encodable metal(loid) nanoparticles which can be cloned into organisms much in the same way as recombinant proteins, with a similar degree of physicochemical uniformity. Implementation of cNPs in imaging contexts may offer reduced protein tag size (compared to 24-mer 0.4 MDa ferritin), pinpoint contrast (compared to DAB-polymerizers), and a sufficient signal-to-noise ratio

(compared to metallothioneins), allowing a more widely adoptable, balanced, and configurable platform. cNPs can moreover theoretically be constituted from a variety of metals, which would be analogous to the colorful toolbox of available fluorescent proteins such as GFP and CFP.

Glutathione reductase-like metalloid reductase (GRLMR), our lab's most 'mature' cNP described to-date, is a 100 kDa homodimer capable of synthesizing and retaining selenium nanoparticles in a cellular context[75,120]. The multimericity of GRLMR can introduce difficulties into labeling studies. Indeed, multimericity has been 'engineered out' of several other protein tags described to date[36,212]. The 100 kDa mass of GRLMR is additionally approaching that of large antibodies, the limitations of which are described in Chapter 1 (namely, positioning contrast markers distally and affecting diffusion/transportation kinetics of protein chimeras). Achieving widespread use of cNPs will require work done to limit deleterious effects from excessive mass and multimericity while also enabling multicolor EM; there is interest in evolving GRLMR to generate nanoparticles from metals other than selenium.

Herein is described work done towards achieving multicolor cNPs through directed evolution of GRLMR, while also rationally reducing enzyme mass and mericity. Fluorescence-assisted cell sorting (FACS) was used to determine if optical properties of cells expressing mutagenic GRLMR libraries could enable selection of non-selenium cNPs. GRLMR was rationally engineered to function as a monomer, which would reduce overall mass significantly. *Muchor racemosus* Cytochrome b5 Reductase[204] (Cb5R) was identified in the literature as a promising ~27 kDa monomeric selenium reductase which might be engineered as a smaller replacement for GRLMR. While each of the project areas were unable to generate desired outcomes, they have been continued through other means involving computation/molecular dynamics by the next generation of graduate students in the Ackerson Research Group.

5.2 Evolving 'multicolor' cNPs

We rationalized that the described 'life/death' method in Chapter 3 may depend on the specific activity and fast kinetics of GRLMR with respect to selenium and might not be readily translatable towards

other metal or enzyme systems. The selection for GRLMR mutants by challenging host cells may be enabled due to GRLMR's uniquely specialized function as a metal reductase; variations may be too slow or nonspecific in initial selection steps to be enriched above the ability of baseline cellular metabolism to withstand toxic quantities of metal(loids). We thus explored alternative high-throughput selection methods in the hopes that a more sensitive protocol could be established.

Fluorescence-assisted cell sorting (FACS) and flow cytometry may be appealing selection methods for directed evolution of metal reductase activity as they can rapidly (in the span of hours) sort through tens of thousands of cells according to their optical properties[213,214]. Moreover, there is evidence that elemental nanoparticles can exhibit unique absorbent and fluorescent properties that could be detectable through FACS[215,216]. We rationalized that it might be possible to sort for intracellular metal reductase activity according to relative amounts of metal in cells, under the hypothesis that cells which have improved ability to reduce ionic metals into insoluble nanoparticles will retain greater amounts as metal, as metal(loid) nanoparticles cannot be excreted by efflux pumps in the same manner as soluble metal(loid) ions[67,217].

5.2.1 *Preliminary experiments with GRLMR*

As a baseline experiment to determine if FACS could differentiate intracellular metal content which correlates to metal reductase activity, we opted to compare Ala-GRLMR and WT-GRLMR. Ala-GRLMR was a negative control, which mutates out the putative di-cysteine active site (Chapter 3). We hypothesized that, if intracellular selenium nanoparticles generated observable absorbance/fluorescence signal, then the WT-GRLMR expressing cells would have a higher degree of absorbance/fluorescence than Ala-GRLMR expressing cells. Each cell type was expressed at 50 uM IPTG overnight with an added 1 mM selenite (a non-lethal amount) to induce intracellular nanoparticle formation. In both cases, cells macroscopically exhibited the red color of zero-valent selenium, as cellular components in the cytosol can reduce selenite[218].

5.2.2 *Sorting Data - Selenite*

Flow cytometry preliminary evidence of selenium in Ala and WT shows there is a difference which may correlate with enzymatic activity. At thresholds set in FlowJo™ [219] for selenium fluorescence, WT-GRLMR exhibited a histogram within which 18% of all cell members exceed baseline, whereas 13% of Ala-GRLMR exceeded the baseline - indicating that there was a population difference (5%) in the amount of absorbance averaged over approximately 10,000 individual samples (**Figure 5.1**). This preliminary experiment supported the hypothesis that cells which have endowed improved ability to reduce ionic metals into particulate form can have higher amounts of metal inside them. With this encouraging data, we next opted to explore whether other metals could do the same.

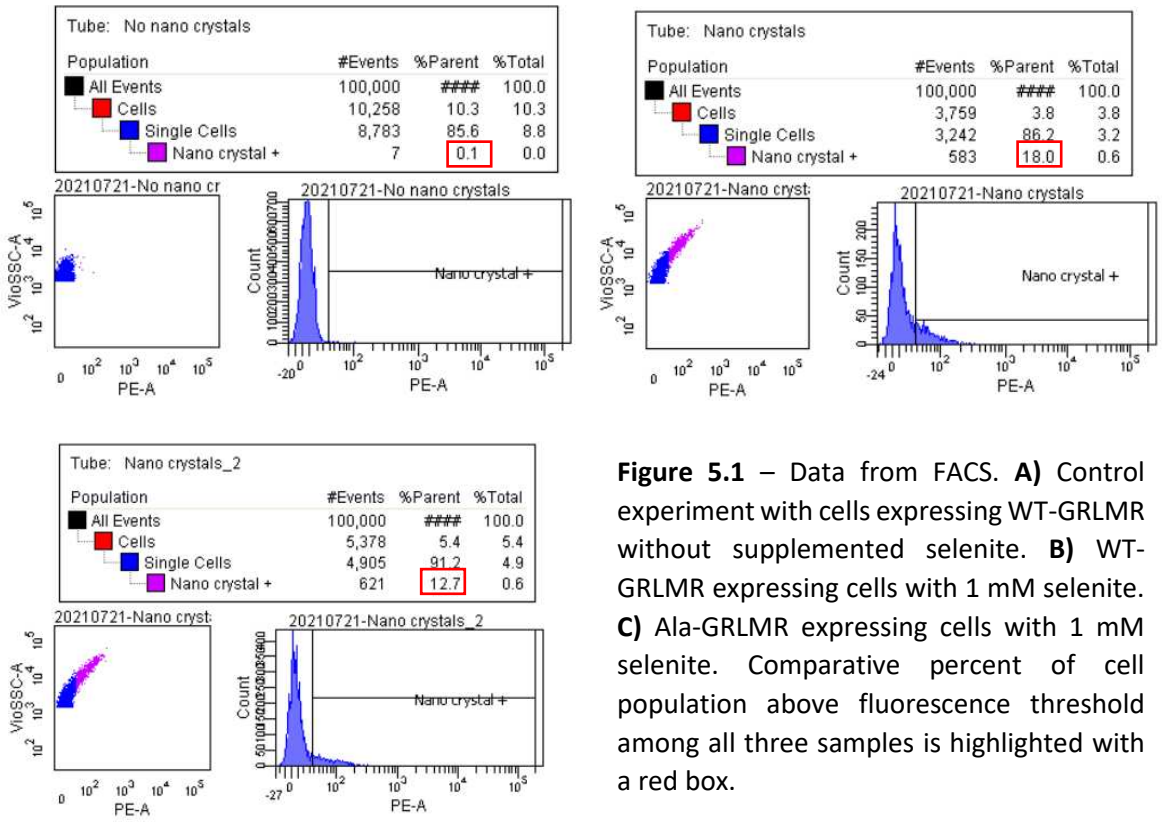

Figure 5.1 – Data from FACS. **A)** Control experiment with cells expressing WT-GRLMR without supplemented selenite. **B)** WT-GRLMR expressing cells with 1 mM selenite. **C)** Ala-GRLMR expressing cells with 1 mM selenite. Comparative percent of cell population above fluorescence threshold among all three samples is highlighted with a red box.

5.2.3 *Bismuth-glutathione and bismuth-cysteine syntheses*

Bismuth (Bi) is the heaviest nonradioactive element and is relatively non-toxic to mammalian cells. In the context of EM, the high-Z number of Bi is extremely attractive as it results in much 'darker' contrast spots (discussed in Chapter 1). We thus directed our initial attempts towards determining whether relative intracellular Bi could be determined via FACS. Subsequently, if we determined intracellular Bi could be determined, we intended to screen mutagenic GRLMR for possible Bi-reduction activity to develop a bismuth cloneable nanoparticle.

In our hands we found that all commercially sourced Bi salts were insoluble in water. We thus developed methods to ligate glutathione and cysteine to Bi to generate soluble forms. Glutathione was ligated to Bi at pH 10, whereas cysteine could be added at neutral conditions. In both cases, addition of the ligand in the appropriate respective condition immediately clarified the insoluble Bi up to ~100 mM. The 'solubilized' Bi was used without further purification. Future work will require purification and characterization to determine if the expected compounds were indeed formed. However, we rationalized that so long as Bi was solubilized and potentially more bioavailable, then cells would be able to internalize some amount such that FACS could determine relative intracellular abundance.

Similarly to the Se experiments, cells were grown in 1 mM Bi-glutathione and 1 mM Bi-cysteine, with non-metal media as a control. In both cases, cells grown overnight with supplemented Bi were pitch black and cells remained black after washing, indicating bismuth internalization. Upon running FACS with cells containing WT-GRLMR and Ala-GRLMR we found no discernable difference (data not shown). However, we note that the Ala-GRLMR vs. WT-GRLMR controls are not necessarily appropriate either. Future work will require known enzymatic activity which reduces Bi-ligands into nanoparticulate form. Nitrate reductase is potentially a promising option[128], however no single enzymes have been described to date which could be considered a bismuth reductase.

In parallel, we attempted to determine if there was latent activity with Bi-GSH compounds using purified enzyme, as previous data had indicated that tellurodiglutathione (GS-Te-SG) could be reduced by GRLMR and SeR. Our preliminary working hypothesis was that, in the case of GRLMR or related glutathione-reducing enzymes/analogues, other varying metals could similarly be ligated with GSH to enable reduction by GRLMR or SeR. Thus far, we have not observed the reduction of GS-[Metal(loid)]-SG substrates using GRLMR outside of selenium or tellurium.

We have also noted that Bi may not be an appropriate metal substrate for GRLMR, as it is typically in the 3+ state. Thus, we are currently exploring enzymes which may more appropriately fit this paradigm. Arsenate reductase[171] is intriguing, as it reduces As(V) to As(III) – while not a 3-electron transfer, we hypothesize coordination chemistry may be similar. And as described above, a nitrate reductase was implicated in bismuth biomineralization[128].

5.2.4 *Conclusions and future directions*

Continuation of the proposed library-based directed evolution through use of FACS would require an enrichment study similar to Chapter 3; e.g., to see if a mixed population of WT and Ala cells could be sorted according to relative enzymatic activities. A primary challenge of ours was developing an appropriate positive and negative control for library members (based on GRLMR or SeR) whose substrate preference was altered for bismuth reduction.

We propose that in vitro experiments using purified enzymes and NADPH in a 96-well plate format may be a more appropriate launchpad for evolving enzyme activities towards metals other than selenium. The only other known instance of evolving metal reductase activity was on a chromate reductase. In their work, a direct measurement of NADPH depletion was sufficient to sort for enzymatic activity. A similar system could be developed where there is no initial enzyme activity, but where mutations could lead to endowed activity. E.g., GRLMR may not currently reduce bismuth compounds, but a mutational library of GRLMR could be investigated for new activity using a NADPH depletion assay rather than FACS. Potential

caveats of this system are that only NADPH/NADH dependent enzymes could be considered, and that nanoparticle formation can obscure absorbance-based data acquisition.

5.3 Minimalization of cNP enzymes

5.3.1 *Monomerization of GRLMR (m-GRLMR)*

Glutathione Reductase-Like Metalloid Reductase (GRLMR) is a relatively large homodimeric selenium reductase constituted from two identical ~50 kDa monomers with an extensive dimerization interface shared between them (**figure 5.2**). As discussed previously, such multimericity and large mass can be a hindrance to protein tagging.

Each of the two mirrored catalytic pockets of Glutathione Reductase (GSHR), the parent homologue of GRLMR which natively reduces oxidized glutathione (GSSG) into reduced glutathione (GSH), make use of amino acid side chains from both monomers. This trait is also shared among other type-II pyridine disulfide oxidoreductases such as mycothione reductase and mercuric reductase, indicating a critical aspect of dimerization for this class of enzymes[2,56]. Although the exact catalytic mechanism of GRLMR towards selenium is currently unknown, preliminary evidence suggests high similarity to its reactivity towards GSHR. Other works have implicated the importance of the di-cysteine active site in mercuric reductase; however it has been demonstrated that the di-cysteine may not necessarily be redox active, but may rather serve to orient substrates near the FAD cofactor[131]. We thus decided to maintain as much of the putative active site channel as possible.

With these considerations, we attempted to monomerize GRLMR by maintaining its native dimerization interfacial core and creating a new solvent-exposed interface to eliminate roughly 1/3rd the overall mass (**Figure 5.3**).

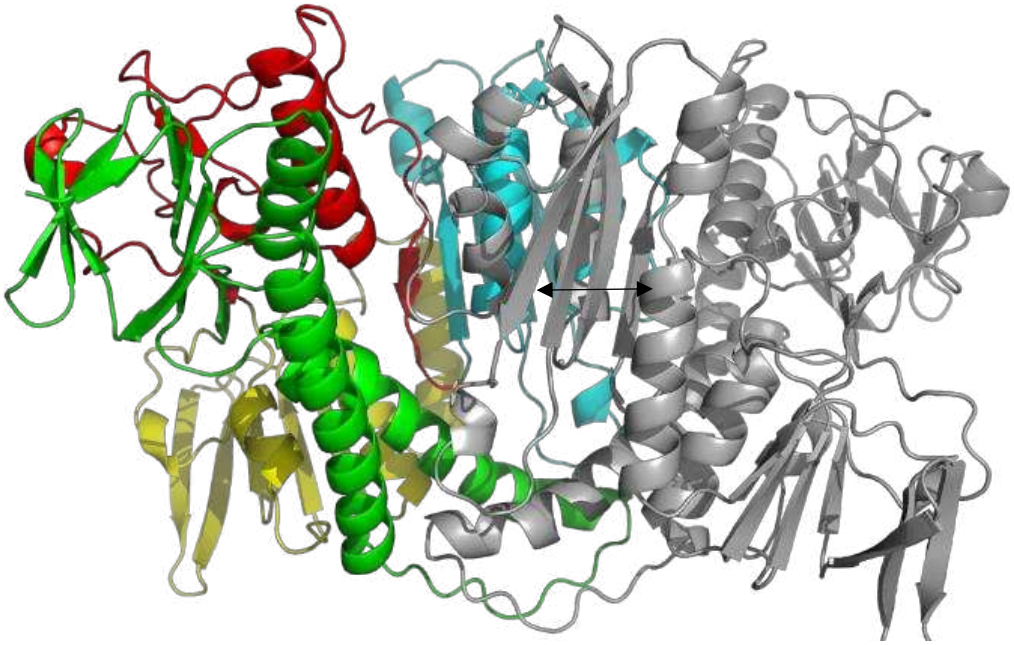

Figure 5.2. Overlay structure of *P. moravenis* GRLMR with respect to highly homologous *P. fluorescines* GSHR obtained through the Robetta server. Respective colors represent NADPH binding region (green), FAD binding domain (yellow), central domain (red), and dimerization domain (teal). Catalytic residues are thought to reside at between the NADPH binding domain and the sister monomer's (shown in grey) dimerization domain.

Protein re-surfacing and removal of dimerization interfaces are established techniques and have been successfully implemented on other cloneable tags to improve probe function such as engineered ascorbate peroxidase[36,220].

5.3.2 *Experimental Approach and Design*

As GRLMR activity is dependent on FAD and NADPH, we opted to maintain their respective domains while maintaining amino acid side chains bridged across the dimerization domain which are implicated in catalysis. In previous work, respective domains of human GSHR were shown to be modestly amenable to solubilization via rational site-directed mutagenesis of important hydrophobic residues[221], suggesting the GRLMR (and other related enzymes) could in theory be monomerized. We thus reasoned

that we could select a new solvent-exposed surface from within core domains of GRLMR to develop an effective 'monomerized' analogue (m-GRLMR).

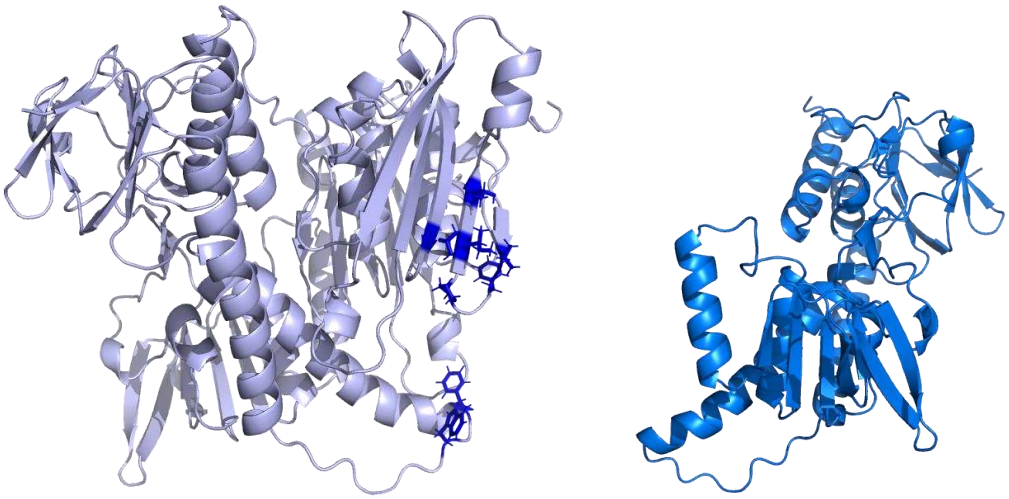

Figure 5.3. Rational design of monomerized GRLMR which maintains active channel residues along the dimerization interface. Newly exposed hydrophobic residues are shown in dark blue. Removed portion of GRLMR shown in teal.

Our newly selected dimerization interface was centered around three continuous α-helices along the native interface, which are in turn flanked by a series of alternating β-sheets and subsequently FAD and NADPH binding domains. An initial construct was envisioned wherein α-helices of the sister monomer would be retained (thus retaining important catalytic residues) while proximal β-sheets and FAD/NADPH domains would be removed, eliminating ~30 kDa from homodimeric GRLMR.

5.3.3 *Molecular Cloning and Protein Expression*

DNA encoding the newly exposed alpha helical dimerization domain was synthesized as a whole gene fragment (gBlock) and purchased from Integrated DNA Technologies, Inc (IDT, Inc.). This fragment was directly concatenated to DNA encoding a single monomer with an added linker through use of restriction digestion sites NdeI and XhoI. This resulted in a DNA construct expressing m-GRLMR with several exposed hydrophobic residues on the outer edge of the newly-exposed alpha helices. These residues were individually replaced with hydrophilic serine using the New England Biolabs site-directed

mutagenesis kit; serine was selected by following previous work on protein resurfacing to eliminate dimerization domains and protein-protein interactions[222]. Upon IPTG-induced expression at varying concentrations, m-GRLMR was completely insoluble as determined by Coomassie-stained SDS-PAGE and did not imbue selenium tolerance to host cells (data not shown) indicating a cessation of activity.

5.3.4 *Molecular Dynamics Simulations*

In addition to ongoing attempts at mGRLMR expression, a team of students (Nathan Krumland, Christopher Covacic, and Ryan Montagne) working under advisement from Professor Chris Snow investigated computational methods to elucidate m-GRLMR properties and to see whether notable optimizations could be made. Simulations were run using GROningen MAchine for Chemical Simulations[223] (GROMACS) and Systematic Hierarchical Algorithms for Rotamers and Proteins on an Extended Network[224] (SHARPEN) to model the expected behavior of m-GRLMR in water over several nanoseconds. Simulations ultimately described that a newly exposed dimerization domain would not adopt a single conformation, thus leading to unstable protein expression and subsequent aggregation.

5.3.5 *mGRLMR - conclusions and future directions*

Lack of soluble expression in concert with preliminary molecular simulations suggesting large-scale protein disorder suggested severe drawbacks in our initial experimental approaches. In retrospect, the monomerization of GRLMR was a highly ambitious inaugural project; even if such a monomer could express stably, it might never have meaningful enzyme function for use as a contrast tag. If soluble and functioning m-GRLMR was realized, it would still have a considerable mass of ~70 kDa (although future optimizations could still be made).

Nevertheless, these efforts were pivotal towards defining more rigid guidelines to improve the cNP platform. A primary result of these studies was realizing the need to more carefully select platform enzymes that are smaller than GRLMR which are also monomeric, as size and multimericity may be difficult or impossible to remove in downstream works. There is ongoing work by Rachel Cohen in the

Snow and Ackerson labs to extend this project by grafting GRLMR's active site into a stable monomer. However, while these and other subsequent works have been done on GRLMR, future works will likely focus on developing other more minimalist enzymes, as even though m-GRLMR may approach ~50-60 kDa it would still be fairly large.

5.3.6 – *Mucor racemosus cytochrome b5 reductase*

Mucor racemosus cytochrome b5 reductase (Cb5R) is a monomeric ~27 kDa enzyme described in work published previously[203,204] and is moderately similar to *Mortierella alpina* Cb5R DNA (57%) and low similarity to human (43%) and *Arabidopsis* (41%) cb5r DNA. Similarly to GRLMR, expression of Cb5R into non-native host *Pichia pastoris* cells was documented to endow nanoparticle-mediated tolerance of toxic quantities of selenium[66]; genetically modified *P. pastoris* containing the enzyme exhibited hallmark red coloration associated with zero-valence Se which were described to be approximately 180 nm in diameter. The described Cb5R also contains FAD and NADH domains, similarly to GRLMR. We thus rationalized that it could be adapted to serve as an improved cNP platform over GRLMR, particularly due to ideal characteristics of low size and monomericity.

5.3.7 *Cb5R - results and discussion*

We reasoned that low purified expression of Cb5R in work published by Elehain et. al. could be attributable to non-optimal codon patterns in *E coli* which would result in undue metabolic stress[225]. A DNA gene block encoding *Mucor racemosus* Cb5R was purchased from IDT, Inc. with codon adaptations made for expression in *E coli*. Cb5R variants including C-terminal 6x histidine tag, C-terminal selenium nanoparticle-binding 12-mer, and N-terminal small ubiquitin-like modifier (SUMO) were subsequently cloned and expressed to assess whether Cb5R might have ideal cNP characteristics.

Upon IPTG-induced expression of mr-Cb5R and its variants in E. coli, no meaningful solubility was observed for any of the variants. Expressed mr-Cb5R appeared to only express insolubly, similarly to m-GRLMR. While it was possible there were trace amounts of Cb5R in soluble fractions, downstream cNP

usefulness would be limited if the gene was particularly subject to aggregation and/or insoluble expression.

We initially reasoned that the mr-Cb5R was crashing out of solution throughout cell lysis procedures. Several parameters were screened to improve expression which included temperature, timeframe, IPTG concentration, lysis buffers, and lysis methods. We additionally cloned DNA into Rosetta Bl21 *E. coli* cells which are specifically adapted for expression of eukaryotic genes[226]. No substantial improvements in soluble expression were observed.

We also tried transforming into *Pichia pastoris* yeast cells. Although cloning was successful as indicated by a diagnostic polymerase chain reaction (PCR) and endowed Zeocin resistance offered by the host plasmid, no protein activity was detected through using His-tag stains on SDS-PAGE gels. Subsequent analysis by proteomic tandem mass spectrometry indicated that no quantifiable amount of Cb5R was detected.

5.3.8 *Conclusion and Future Directions – Cb5R*

Reliable expression of Cb5R in bacteria and in yeast has yet to be realized. In the time since the aforementioned studies, we have noted three potential surface-exposed glycosylation sites on Cb5R. As glycosylation is a eukaryotic process, lack of glycosylation machinery within *E. coli* could have potentially led to insoluble protein expression. Further experimentation would be needed to determine this.

We nevertheless maintain that Cb5R could serve as an excellent starting point for downstream use as a cNP. There is ongoing work by Rachel Cohen to develop more readily expressible analogues by 'supercharging' protein surfaces to highly positive or negative chemistries through computational design. Preliminary evidence indicates that the initial supercharged enzymes have activity towards Se(4+) in PBS, as indicated by visual observation of enzyme in the presence of NADH and selenium sources over several days (formation of red coloring). It is likely that the enzyme will require evolution/development to achieve

reaction kinetics that are on the same order as GRLMR, which is noted in the literature as having the most amount of activity towards selenium[126].

5.4 Conclusions and future directions

The cNP platform is promising, but nascent. A great deal of work is needed to make the cNP platform attractive and widely applicable to the next generation of structural biology research. There is much interest in developing clonable tags that are minimally perturbing and have the ability to track multimodal systems. Here we have demonstrated some initial efforts towards these ends, which are expected to continue in future works. Most prominently, the recent advent of AlphaFold[137] and other computational tools may now more readily enable computational development of such cNP enzymes.

Initial results suggest FACS is capable of sorting for cells with high intracellular content of metal, which may be correlated to increased enzymatic reduction of soluble metal into insoluble (and potentially optically active) solid. Future work will be needed to **1)** determine a more appropriate 'starting point' for Bi reduction (e.g., through use of a different enzyme such as arsenate reductase) and **2)** identify appropriate control experiments which can lead to the development of a robust selection platform. FACS is highly attractive due to its high throughput and relative ease of experimental setup. However, we propose that an NADPH depletion assay in a 96-well plate format of purified enzymes may be a more sensitive approach for initial studies. Other options could be considered as well, such as **1)** relative gravity/density and **2)** proxy staining of intracellular metal content and/or substrate depletion (e.g., through XPS).

While GRLMR was not successfully adapted into a monomeric unit in the presented works, there is ongoing work by Rachel Cohen, Tony Tien, and Gavin McEwen to 'hallucinate' the active site into different protein scaffolds through deep machine learning[227]. Furthermore, Cb5R is nearing soluble expression through the work of Rachel Cohen using AlphaFold and other computational methods. We have also considered the use of *de novo* protein discovery/design, which has been gaining traction in

recent years. Indeed, a recent publication described the *de novo* discovery of a small protein which can synthesize quantum dots[228,229].

As a final note, we are currently exploring the use of cNPs in several model organisms, which is not otherwise discussed in This Thesis. Preliminary work has indicated that the GRLMR Se cNP is capable of functioning in *Pichia pastoris* yeast cells, in *Drosophila melanogaster* fruit flies, and potentially in HeLa mammalian cells. We are also exploring the use of cNPs in correlative light electron microscopy (CLEM) and computed tomography (CT). Over the next several years/decades, we hope that the cNP platform will grow to rival or exceed the profound influence that fluorescent proteins have had on biological imaging.

5.5 Materials and Methods

All DNA oligomer primers and gene blocks were purchased from Integrated DNA Technologies (IDT), Inc. Restriction enzymes, Q5 polymerase, Quick Ligase, 1kb and 100 bp DNA gel ladders, and 6x DNA loading buffers were purchased from New England Biolabs (NEB) along with their respective buffers. Monarch Plasmid Miniprep kits and Monarch DNA Gel Extraction kits were purchased from NEB. pET20b+ vector was purchased through Millipore Sigma. LB Miller Broth powder was purchased from IBI Scientific. Tryptone, yeast extract, glucose, agarose, SYBR I Nucleic Acid Stain, Pierce protease inhibitor tablets, and agar were purchased from Thermo Fischer. All antibiotics were purchased from Gold Biotechnology. 40% acrylamide 1% bis-acrylamide solution was purchased from Bio-Rad. All other reagents were purchased from Sigma Aldrich. Buffers were made in-house and are described in the following: 50x TAE buffer (50 mM EDTA disodium salt, 2 M Tris-base, 1 M glacial acetic acid), super optimal growth (SOC) media (2% w/v tryptone, 0.5 % w/v yeast extract, 10 mM NaCl, 2.5 mM KCl, 10 mM MgCl2, 20 mM glucose), 10x SDS-PAGE buffer (30 g Trizma base, 10 g sodium dodecyl sulfate (SDS), 144 g glycine dissolved in 1 L H2O), 0.1% Coomassie staining reagent (0.1 g Coomassie R250, 100 mL glacial acetic acid, 400 mL methanol to 1 L with H2O), SDS-PAGE gel fixing solution (10% glacial acetic acid, 40% ethanol, 50% H2O), SDS-PAGE gel washing solution (10% glacial acetic acid, 40% methanol, 50% H2O), 10x phosphate buffered saline

solution (80 g NaCl, 2.0 g KCl, 14.4 g Na2HPO4, 2.4 g KH2PO4 to 1 L, pH 7.4), Tris cell lysis buffer (20 mM Tris HCl, 137 mM NaCl, 5% glycerol, 1% Triton X-100). Chemically competent BL21 DE3 PlysS and DH5α E. coli cells were cultured in-house and stored at -80 °C in 0.1 M CaCl, 15% glycerol in 50 uL aliquots. Roestta DE3 PlysS E. coli cells were purchased from EMD Millipore Sigma.

5.5.1 *Molecular cloning*

Generalized procedures were carried out as outlined: Polymerase chain reactions (PCRs) and restriction digestions were performed using a Bio-Rad MJ Mini Personal Thermal Cycler and followed protocols outlined by NEB. Digestion and PCR products mixed with DNA loading dye and SYBR I Nucleic Acid Stain to 1x working concentrations were purified on 1% agarose gels using 1x TAE buffer at 115 V, 40 min on Bio-Rad PowerPac Basic power supplies. Post-electrophoresed gels visualized by UV illumination, and desired fragments were excised and purified using the Monarch DNA Gel Extraction Kit. All DNA concentrations were recorded using a Nanodrop 2000 (Thermo Fischer). DNA ligations used Quick Ligase and the established procedure. Chemically competent DH5 E. coli cells were thawed on ice for 10 min under sterile conditions, and 2 uL chilled ligation mixture was added. The cells were further incubated for 30 min on ice, followed by a 30 s incubation in a 37 °C water bath, followed by an additional 5 min incubation on ice. Subsequently, 950 uL sterile SOC media was added, and the suspended cells were incubated at 37 °C, 250 RPM for 1 h. 200 uL of incubated cells were added to pre-set LB-agar gels containing ampicillin (100 ug/mL) under sterile conditions then placed in a 37 °C incubator overnight. Respective colonies were picked into 5 mL LB-ampicillin cultures for overnight growth at 37 °C, 250 RPM. Prior to DNA harvesting through use of the Monarch Plasmid Miniprep Kit, cells were centrifuged (Beckman Coulter Avanti J-E) at 5,000 g for 10 min at 4 °C and supernatant was discarded. and sent to Genewiz for sequencing. Bacterial colonies containing desired sequenced DNA were stored at -80 °C in 25% glycerol.

5.5.2 *Protein Expression*

BL21 DE3 PlysS cells (50 uL) were thawed on ice for 10 min, to which was added chilled 1 uL sequenced DNA of genes-of-interest ligated into pET20b+ vector. The mixture was gently flicked to mix, and incubated on ice for 10 min. The cell mixture was then incubated in a 37 °C water bath for 10 s before returning to ice for 1 min. 950 uL SOC media was added to resuspend the cells, and the mixture was incubated at 37 °C, 250 RPM for 1 h. 50 uL incubated cells were then plated on LB-agar plates containing 100 ug/mL ampicillin and 25 ug/mL chloramphenicol (to maintain the PlysS plasmid). Selected colonies were grown in 5 mL LB-ampicillin/chloramphenicol culture at 37 °C, 250 RPM overnight before miniprepping for sequencing. Sequenced colonies were stored at -80 °C in 25% glycerol for future use. For protein expression, glycerol stock bacterial samples were incubated overnight in 5 mL LB-ampicillin/chloramphenicol media at 37 °C, 250 RPM. Cultures grown overnight were inoculated in a 1:100 ratio to 50 or 100 mL LB-ampicillin/chloramphenicol. Upon reaching an optical density at 600 nm (OD600), IPTG was added to a final concentration of 1 mM (1 uM selenite was additionally added to induced cultures of GRLMR). Induced cells were grown overnight at r.t. on an orbital shaker set to approximately 150 RPM. The cell cultures were then centrifuged at 5,000 g at 4 °C for 10 min and the supernatant discarded. Cell pellets were re-suspended in 1x PBS containing protease inhibitor cocktail, and the suspensions were probe-sonicated (Thermo Fischer) for 10 min in intervals of 3 s on, 7 s off on ice. Lysed cells were clarified by centrifugation at 10,000 g for 30 min at 4 °C, and the soluble fractions were passed through 0.22 um filters prior to usage and storage (at 4 °C). Insoluble fractions were stored at -20 °C.

5.5.3 *Native-PAGE and SDS-PAGE*

Native-PAGE buffers and gels were prepared in identical fashion to SDS-PAGE with the exceptions of SDS addition and running temperature (native-PAGE was run at 4 °C and SDS-PAGE at r.t.). 10% SDS-PAGE gels were prepared by addition of 7.7 mL water, 4 mL 40% acrylamide 1% bis-acrylamide (pre-warmed to r.t.), 4 mL 1.5 M Tris base pH 8.8, 160 uL 10 % SDS, 160 uL 10% ammonium persulfate, 16 uL

tetramethylethylenediamine (TEMED). Upon TEMED addition, the gels were immediately poured into 1.5 mm casts (Bio-Rad) and allowed to polymerize for at least 1 h at r.t. Protein samples were prepared as 16 uL aliquots using 4x loading dye (4% β mercaptoethanol, 0.02 % bromophenol blue, 25% glycerol, 10% SDS, 250 mM Tris HCl) at 1x working concentration. Approximated protein concentrations measured at an absorbance of 280 nm were targeted to 40 ug/sample. Insoluble fractions were swabbed with the tip of a pipette and dissolved into 40 uL 1x loading dye. All protein samples were heated to 95 °C for 5 min to ensure denaturation before being immediately added to SDS-PAGE gels. Gels were run at 150 V for 1 h at r.t. Gels were then fixed in ethanol solution for 1 h with gentle agitation, followed by a washing step in methanol solution overnight, also with gentle agitation at r.t. Fixed and washed gels were gently agitated in Coomassie staining reagent for 1 h at r.t., then placed in water with addition of Kimwipes (to adsorb away excess stain). Upon completion of the de-staining process, gels were placed on an illuminator for imaging with a digital Canon Rebel XT camera.

5.5.4 *FACS experiments*

Fluorescence assisted cell sorting (FACS) was run on a FACSAria-III (BD Biosciences) by the Colorado State University Flow Cytometry, Cell Sorting, and Single Cell Sequencing Facility. Prior to sorting, cells were grown overnight in 5 mL LB/Carb until confluency. The following day, a 100 uL aliquot was inoculated into 5 mL fresh LB/Carb and allowed to grow to OD600 of 0.5. Protein expression was induced through addition of IPTG to a final concentration of 50 uM and cells were allowed to grow overnight at RT at 250 RPM. Cultures were supplemented with up to 1 mM of Bi, Se, and Zn salts. The following day, cell cultures were centrifuged at 3,000 g, then washed with 5 mL cold sterile PBS. Cells were pelleted, then resuspended immediately prior to cell sorting in PBS.

REFERENCES

(1) Hendricks, A. R.; Guilliams, B. F.; Cohen, R. S.; Tien, T.; McEwen, G. A.; Borgognoni, K. M.; Ackerson, C. J. Cloneable Inorganic Nanoparticles. *Chem. Commun.* **2023**, 10.1039.D3CC01319G. https://doi.org/10.1039/D3CC01319G.

(2) Butz, Z. J.; Hendricks, A.; Borgognoni, K.; Ackerson, C. J. Identification of a TeO32− Reductase/Mycothione Reductase from *Rhodococcus Erythropolis* PR4. *FEMS Microbiology Ecology* **2020**, *97* (1), fiaa220. https://doi.org/10.1093/femsec/fiaa220.

(3) Hendricks, A.; Cohen, R.; McEwen, G.; Tien, T.; Guilliams, B.; Alspach, A.; Snow, C.; Ackerson, C. *Laboratory Evolution of Metalloid Reductase Substrate Specificity and Product Size*; preprint; Chemistry, 2023. https://doi.org/10.26434/chemrxiv-2023-w2swm.

(4) Rensen, E.; Pietropaoli, S.; Mueller, F.; Weber, C.; Souquere, S.; Sommer, S.; Isnard, P.; Rabant, M.; Gibier, J.-B.; Terzi, F.; Simon-Loriere, E.; Rameix-Welti, M.-A.; Pierron, G.; Barba-Spaeth, G.; Zimmer, C. Sensitive Visualization of SARS-CoV-2 RNA with CoronaFISH. *Life Sci. Alliance* **2022**, *5* (4), e202101124. https://doi.org/10.26508/lsa.202101124.

(5) Hopfer, H.; Herzig, M. C.; Gosert, R.; Menter, T.; Hench, J.; Tzankov, A.; Hirsch, H. H.; Miller, S. E. Hunting Coronavirus by Transmission Electron Microscopy – a Guide to SARS-CoV-2-associated Ultrastructural Pathology in COVID-19 Tissues. *Histopathology* **2021**, *78* (3), 358–370. https://doi.org/10.1111/his.14264.

(6) Xu, Y.-H.; Dong, J.-H.; An, W.-M.; Lv, X.-Y.; Yin, X.-P.; Zhang, J.-Z.; Dong, L.; Ma, X.; Zhang, H.-J.; Gao, B.-L. Clinical and Computed Tomographic Imaging Features of Novel Coronavirus Pneumonia Caused by SARS-CoV-2. *Journal of Infection* **2020**, *80* (4), 394–400. https://doi.org/10.1016/j.jinf.2020.02.017.

(7) Delorme, C.; Paccoud, O.; Kas, A.; Hesters, A.; Bombois, S.; Shambrook, P.; Boullet, A.; Doukhi, D.; Le Guennec, L.; Godefroy, N.; Maatoug, R.; Fossati, P.; Millet, B.; Navarro, V.; Bruneteau, G.; Demeret, S.; Pourcher, V.; the CoCo-Neurosciences study group and COVID SMIT PSL study group; Delorme, C.; Corvol, J.; Delattre, J.; Carvalho, S.; Sagnes, S.; Dubois, B.; Navarro, V.; Louapre, C.; Stojkovic, T.; Idbaih, A.; Rosso, C.; Grabli, D.; Gales, A. Z.; Millet, B.; Rohaut, B.; Bayen, E.; Dupont, S.; Bruneteau, G.; Lehericy, S.; Seilhean, D.; Durr, A.; Lamari, F.; Houot, M.; Brochard, V. B.; Dupont, S.; Lubetzki, C.; Seilhean, D.; Pradat-Diehl, P.; Rosso, C.; Hoang-Xuan, K.; Fontaine, B.; Naccache, L.; Fossati, P.; Arnulf, I.; Durr, A.; Carpentier, A.; Lehericy, S.; Edel, Y.; Robain, G.; Thoumie, P.; Degos, B.; Sharshar, T.; Alamowitch, S.; Apartis-Bourdieu, E.; Peretti, C.; Ursu, R.; Dzierzynski, N.; Bourron, K. K.; Belmin, J.; Oquendo, B.; Pautas, E.; Verny, M.; Delorme, C.; Corvol, J.; Delattre, J.; Samson, Y.; Leder, S.; Leger, A.; Deltour, S.; Baronnet, F.; Gales, A. Z.; Bombois, S.; Touat, M.; Idbaih, A.; Sanson, M.; Dehais, C.; Houillier, C.; Laigle-Donadey, F.; Psimaras, D.; Alenton, A.; Younan, N.; Villain, N.; Grabli, D.; Amador, M. del M.; Bruneteau, G.; Louapre, C.; Mariani, L.; Mezouar, N.; Mangone, G.; Meneret, A.; Hartmann, A.; Tarrano, C.; Bendetowicz, D.; Pradat, P.; Baulac, M.; Sambin, S.; Pichit, P.; Chochon, F.; Hesters, A.; Nguyen, B. H. H.; Procher, V.; Demoule, A.; Morawiec, E.; Mayaux, J.; Faure, M.; Ewenczyk, C.; Coarelli, G.; Heinzmann, A.; Stojkovic, T.; Masingue, M.; Bassez, G.; Navarro, V.; An, I.; Worbe, Y.; Lambrecq, V.; Debs, R.; Musat, E. M.; Lenglet, T.; Lambrecq, V.; Hanin, A.; Chougar, L.; Shor, N.; Pyatigorskaya, N.; Galanaud, D.; Leclercq, D.; Demeret, S.; Rohaut, B.; Cao, A.; Marois, C.; Weiss, N.; Gassama, S.; Guennec, L. L.; Degos, V.; Jacquens, A.; Similowski, T.; Morelot-Panzini, C.; Rotge, J.; Saudreau, B.; Millet, B.; Pitron, V.; Sarni, N.; Girault, N.; Maatoug, R.; Gales, A. Z.; Leu, S.; Bayen, E.; Thivard, L.; Mokhtari, K.; Plu, I.; Gonçalves, B.; Bottin, L.; Yger, M.; Ouvrard, G.; Haddad, R.; Ketz, F.; Lafuente, C.; Oasi, C.; Megabarne, B.; Herve, D.; Salman, H.; Rametti-Lacroux, A.;

Chalançon, A.; Herve, A.; Royer, H.; Beauzor, F.; Maheo, V.; Laganot, C.; Minelli, C.; Fekete, A.; Grine, A.; Biet, M.; Hilab, R.; Besnard, A.; Bouguerra, M.; Goudard, G.; Houairi, S.; Al-Youssef, S.; Pires, C.; Oukhedouma, A.; Siuda-Krzywicka, K.; Malkinson, T. S.; Agguini, H.; Said, S.; Houot, M. COVID-19-related Encephalopathy: A Case Series with Brain FDG-positron-emission Tomography/Computed Tomography Findings. *Euro J of Neurology* **2020**, *27* (12), 2651–2657. https://doi.org/10.1111/ene.14478.

(8) Zheng, Z.; Lauritzen, J. S.; Perlman, E.; Robinson, C. G.; Nichols, M.; Milkie, D.; Torrens, O.; Price, J.; Fisher, C. B.; Sharifi, N.; Calle-Schuler, S. A.; Kmecova, L.; Ali, I. J.; Karsh, B.; Trautman, E. T.; Bogovic, J. A.; Hanslovsky, P.; Jefferis, G. S. X. E.; Kazhdan, M.; Khairy, K.; Saalfeld, S.; Fetter, R. D.; Bock, D. D. A Complete Electron Microscopy Volume of the Brain of Adult Drosophila Melanogaster. *Cell* **2018**, *174* (3), 730-743.e22. https://doi.org/10.1016/j.cell.2018.06.019.

(9) Nguyen, J. P.; Shipley, F. B.; Linder, A. N.; Plummer, G. S.; Liu, M.; Setru, S. U.; Shaevitz, J. W.; Leifer, A. M. Whole-Brain Calcium Imaging with Cellular Resolution in Freely Behaving *Caenorhabditis Elegans*. *Proc. Natl. Acad. Sci. U.S.A.* **2016**, *113* (8). https://doi.org/10.1073/pnas.1507110112.

(10) Goerzen, D.; Fowler, C.; Devenyi, G. A.; Germann, J.; Madularu, D.; Chakravarty, M. M.; Near, J. An MRI-Derived Neuroanatomical Atlas of the Fischer 344 Rat Brain. *Sci Rep* **2020**, *10* (1), 6952. https://doi.org/10.1038/s41598-020-63965-x.

(11) Neumann, D.; Kollorz, E. Ultrasound. In *Medical Imaging Systems*; Maier, A., Steidl, S., Christlein, V., Hornegger, J., Eds.; Lecture Notes in Computer Science; Springer International Publishing: Cham, 2018; Vol. 11111, pp 237–249. https://doi.org/10.1007/978-3-319-96520-8_11.

(12) Moses, W. W. Fundamental Limits of Spatial Resolution in PET. *Nuclear Instruments and Methods in Physics Research Section A: Accelerators, Spectrometers, Detectors and Associated Equipment* **2011**, *648*, S236–S240. https://doi.org/10.1016/j.nima.2010.11.092.

(13) Jamme, F.; Kascakova, S.; Villette, S.; Allouche, F.; Pallu, S.; Rouam, V.; Réfrégiers, M. Deep UV Autofluorescence Microscopy for Cell Biology and Tissue Histology: Deep UV Autofluorescence Microscopy. *Biol. Cell* **2013**, *105* (7), 277–288. https://doi.org/10.1111/boc.201200075.

(14) Cremer, J. T.; Piestrup, M. A.; Gary, C. K.; Pantell, R. H.; Glinka, C. J. Biological Imaging with a Neutron Microscope. *Appl. Phys. Lett.* **2004**, *85* (3), 494–496. https://doi.org/10.1063/1.1774254.

(15) Jacobsen, C.; Kirz, J. X-Ray Microscopy with Synchrotron Radiation. *Nat Struct Mol Biol* **1998**, *5* (8), 650–653. https://doi.org/10.1038/1341.

(16) Ettinger, A.; Wittmann, T. Fluorescence Live Cell Imaging. In *Methods in Cell Biology*; Elsevier, 2014; Vol. 123, pp 77–94. https://doi.org/10.1016/B978-0-12-420138-5.00005-7.

(17) Leung, B. O.; Chou, K. C. Review of Super-Resolution Fluorescence Microscopy for Biology. *Appl Spectrosc* **2011**, *65* (9), 967–980. https://doi.org/10.1366/11-06398.

(18) Huang, B.; Bates, M.; Zhuang, X. Super-Resolution Fluorescence Microscopy. *Annu. Rev. Biochem.* **2009**, *78* (1), 993–1016. https://doi.org/10.1146/annurev.biochem.77.061906.092014.

(19) Prakash, K.; Diederich, B.; Heintzmann, R.; Schermelleh, L. Super-Resolution Microscopy: A Brief History and New Avenues. *Phil. Trans. R. Soc. A.* **2022**, *380* (2220), 20210110. https://doi.org/10.1098/rsta.2021.0110.

(20) Hofer, F.; Schmidt, F. P.; Grogger, W.; Kothleitner, G. Fundamentals of Electron Energy-Loss Spectroscopy. *IOP Conf. Ser.: Mater. Sci. Eng.* **2016**, *109*, 012007. https://doi.org/10.1088/1757-899X/109/1/012007.

(21) Callaway, E. Revolutionary Cryo-EM Is Taking over Structural Biology. *Nature* **2020**, *578* (7794), 201–201. https://doi.org/10.1038/d41586-020-00341-9.

(22) Milne, J. L. S.; Borgnia, M. J.; Bartesaghi, A.; Tran, E. E. H.; Earl, L. A.; Schauder, D. M.; Lengyel, J.; Pierson, J.; Patwardhan, A.; Subramaniam, S. Cryo-Electron Microscopy - a Primer for the Non-Microscopist. *FEBS J* **2013**, *280* (1), 28–45. https://doi.org/10.1111/febs.12078.

(23) Cressey, D.; Callaway, E. Cryo-Electron Microscopy Wins Chemistry Nobel. *Nature* **2017**, *550* (7675), 167–167. https://doi.org/10.1038/nature.2017.22738.
(24) Mollenhauer, H. H. Artifacts Caused by Dehydration and Epoxy Embedding in Transmission Electron Microscopy. *Microsc. Res. Tech.* **1993**, *26* (6), 496–512. https://doi.org/10.1002/jemt.1070260604.
(25) Ni, T. W.; Staicu, L. C.; Nemeth, R. S.; Schwartz, C. L.; Crawford, D.; Seligman, J. D.; Hunter, W. J.; Pilon-Smits, E. A. H.; Ackerson, C. J. Progress toward Clonable Inorganic Nanoparticles. *Nanoscale* **2015**, *7* (41), 17320–17327. https://doi.org/10.1039/C5NR04097C.
(26) *Transmission Electron Microscopy*; Carter, C. B., Williams, D. B., Eds.; Springer International Publishing: Cham, 2016. https://doi.org/10.1007/978-3-319-26651-0.
(27) Pandithage, R. *Brief Introduction to Contrasting for EM Sample Preparation*. Leica Microsystems. https://www.leica-microsystems.com/science-lab/life-science/brief-introduction-to-contrasting-for-em-sample-preparation/ (accessed 2023-05-09).
(28) Watson, M. L. Staining of Tissue Sections for Electron Microscopy with Heavy Metals. *The Journal of Cell Biology* **1958**, *4* (4), 475–478. https://doi.org/10.1083/jcb.4.4.475.
(29) Bozzola, J. J.; Russell, L. D. *Electron Microscopy: Principles and Techniques for Biologists*, 2nd ed.; Jones and Bartlett: Sudbury, Mass, 1999.
(30) He, Y.; Jensen, G. J.; Bjorkman, P. J. Nanogold as a Specific Marker for Electron Cryotomography. *Microsc Microanal* **2009**, *15* (3), 183–188. https://doi.org/10.1017/S1431927609090424.
(31) Singer, S. J. Preparation of an Electron-Dense Antibody Conjugate. *Nature* **1959**, *183* (4674), 1523–1524. https://doi.org/10.1038/1831523a0.
(32) Webster, P.; Schwarz, H.; Griffiths, G. Chapter 3 Preparation of Cells and Tissues for Immuno EM. In *Methods in Cell Biology*; Elsevier, 2008; Vol. 88, pp 45–58. https://doi.org/10.1016/S0091-679X(08)00403-2.
(33) Jones, J. C. R. Pre- and Post-Embedding Immunogold Labeling of Tissue Sections. In *High-Resolution Imaging of Cellular Proteins*; Schwartzbach, S. D., Skalli, O., Schikorski, T., Eds.; Methods in Molecular Biology; Springer New York: New York, NY, 2016; Vol. 1474, pp 291–307. https://doi.org/10.1007/978-1-4939-6352-2_19.
(34) Griffiths, G.; Lucocq, J. M. Antibodies for Immunolabeling by Light and Electron Microscopy: Not for the Faint Hearted. *Histochem Cell Biol* **2014**, *142* (4), 347–360. https://doi.org/10.1007/s00418-014-1263-5.
(35) Shu, X.; Lev-Ram, V.; Deerinck, T. J.; Qi, Y.; Ramko, E. B.; Davidson, M. W.; Jin, Y.; Ellisman, M. H.; Tsien, R. Y. A Genetically Encoded Tag for Correlated Light and Electron Microscopy of Intact Cells, Tissues, and Organisms. *PLoS Biology* **2011**, *9* (4), e1001041. https://doi.org/10.1371/journal.pbio.1001041.
(36) Martell, J. D.; Deerinck, T. J.; Sancak, Y.; Poulos, T. L.; Mootha, V. K.; Sosinsky, G. E.; Ellisman, M. H.; Ting, A. Y. Engineered Ascorbate Peroxidase as a Genetically Encoded Reporter for Electron Microscopy. *Nat Biotechnol* **2012**, *30* (11), 1143–1148. https://doi.org/10.1038/nbt.2375.
(37) Morphew, M. K.; O'Toole, E. T.; Page, C. L.; Pagratis, M.; Meehl, J.; Giddings, T.; Gardner, J. M.; Ackerson, C.; Jaspersen, S. L.; Winey, M.; Hoenger, A.; Mcintosh, J. R. Metallothionein as a Clonable Tag for Protein Localization by Electron Microscopy of Cells: METALLOTHIONEIN FOR PROTEIN LOCALIZATION IN CELLS. *Journal of Microscopy* **2015**, *260* (1), 20–29. https://doi.org/10.1111/jmi.12262.
(38) Wang, Q.; Mercogliano, C. P.; Löwe, J. A Ferritin-Based Label for Cellular Electron Cryotomography. *Structure* **2011**, *19* (2), 147–154. https://doi.org/10.1016/j.str.2010.12.002.
(39) Magos, L.; Tuffery, A. A.; Clarkson, T. W. Volatilization of Mercury By Bacteria. *Occupational and Environmental Medicine* **1964**, *21* (4), 294–298. https://doi.org/10.1136/oem.21.4.294.
(40) Choudhury, R; Srivastava, S. Zinc Resistance Mechanisms in Bacteria. *Curr Sci* **2001**, *81* (7), 768–775.

(41) Puškarova, A.; Ferianc, P.; Kormanec, J.; Homerova, D.; Farewell, A.; Nyström, T. Regulation of YodA Encoding a Novel Cadmium-Induced Protein in Escherichia Coli The GenBank Accession Number for the E. Coli YodA Gene and the SWISS-PROT Accession Number for E. Coli YodA Protein in This Paper Are AAC75039 and P76344, Respectively. *Microbiology* **2002**, *148* (12), 3801–3811. https://doi.org/10.1099/00221287-148-12-3801.

(42) Sarret, G.; Avoscan, L.; Carrière, M.; Collins, R.; Geoffroy, N.; Carrot, F.; Covès, J.; Gouget, B. Chemical Forms of Selenium in the Metal-Resistant Bacterium *Ralstonia Metallidurans* CH34 Exposed to Selenite AndSelenate. *Appl Environ Microbiol* **2005**, *71* (5), 2331–2337. https://doi.org/10.1128/AEM.71.5.2331-2337.2005.

(43) Ollivier, P. R. L.; Bahrou, A. S.; Marcus, S.; Cox, T.; Church, T. M.; Hanson, T. E. Volatilization and Precipitation of Tellurium by Aerobic, Tellurite-Resistant Marine Microbes. *Appl Environ Microbiol* **2008**, *74* (23), 7163–7173. https://doi.org/10.1128/AEM.00733-08.

(44) von Rozycki, T.; Nies, D. H. Cupriavidus Metallidurans: Evolution of a Metal-Resistant Bacterium. *Antonie van Leeuwenhoek* **2009**, *96* (2), 115–139. https://doi.org/10.1007/s10482-008-9284-5.

(45) Llorens, I.; Untereiner, G.; Jaillard, D.; Gouget, B.; Chapon, V.; Carriere, M. Uranium Interaction with Two Multi-Resistant Environmental Bacteria: Cupriavidus Metallidurans CH34 and Rhodopseudomonas Palustris. *PLoS ONE* **2012**, *7* (12), e51783. https://doi.org/10.1371/journal.pone.0051783.

(46) Lal, D.; Nayyar, N.; Kohli, P.; Lal, R. Cupriavidus Metallidurans: A Modern Alchemist. *Indian J Microbiol* **2013**, *53* (1), 114–115. https://doi.org/10.1007/s12088-013-0355-6.

(47) Arenas, F. A.; Pugin, B.; Henríquez, N. A.; Arenas-Salinas, M. A.; Díaz-Vásquez, W. A.; Pozo, M. F.; Muñoz, C. M.; Chasteen, T. G.; Pérez-Donoso, J. M.; Vásquez, C. C. Isolation, Identification and Characterization of Highly Tellurite-Resistant, Tellurite-Reducing Bacteria from Antarctica. *Polar Science* **2014**, *8* (1), 40–52. https://doi.org/10.1016/j.polar.2014.01.001.

(48) Huang, P. C.; Morris, S.; Dinman, J.; Pine, R.; Smith, B. Role of Metallothionein in Detoxification and Tolerance to Transition Metals. In *Metallothionein II*; Kägi, J. H. R., Kojima, Y., Eds.; Experientia Supplementum; Birkhäuser Basel: Basel, 1987; Vol. 52, pp 439–446. https://doi.org/10.1007/978-3-0348-6784-9_43.

(49) Ecker, D. J.; Butt, T. R.; Sternberg, E. J.; Neeper, M. P.; Debouck, C.; Gorman, J. A.; Crooke, S. T. Yeast Metallothionein Function in Metal Ion Detoxification. *Journal of Biological Chemistry* **1986**, *261* (36), 16895–16900. https://doi.org/10.1016/S0021-9258(19)75973-0.

(50) Klaassen, C. D.; Liu, J.; Choudhuri, S. METALLOTHIONEIN: An Intracellular Protein to Protect Against Cadmium Toxicity. *Annu. Rev. Pharmacol. Toxicol.* **1999**, *39* (1), 267–294. https://doi.org/10.1146/annurev.pharmtox.39.1.267.

(51) Reddy, M. S.; Prasanna, L.; Marmeisse, R.; Fraissinet-Tachet, L. Differential Expression of Metallothioneins in Response to Heavy Metals and Their Involvement in Metal Tolerance in the Symbiotic Basidiomycete Laccaria Bicolor. *Microbiology* **2014**, *160* (10), 2235–2242. https://doi.org/10.1099/mic.0.080218-0.

(52) Schor-Fumbarov, T.; Goldsbrough, P. B.; Adam, Z.; Tel-Or, E. Characterization and Expression of a Metallothionein Gene in the Aquatic Fern Azolla Filiculoides under Heavy Metal Stress. *Planta* **2005**, *223* (1), 69–76. https://doi.org/10.1007/s00425-005-0070-6.

(53) Li, L.-S.; Meng, Y.-P.; Cao, Q.-F.; Yang, Y.-Z.; Wang, F.; Jia, H.-S.; Wu, S.-B.; Liu, X.-G. Type 1 Metallothionein (ZjMT) Is Responsible for Heavy Metal Tolerance in Ziziphus Jujuba. *Biochemistry Moscow* **2016**, *81* (6), 565–573. https://doi.org/10.1134/S000629791606002X.

(54) Yang, Z.; Lu, L.; Berard, V. F.; He, Q.; Kiely, C. J.; Berger, B. W.; McIntosh, S. Biomanufacturing of CdS Quantum Dots. *Green Chem.* **2015**, *17* (7), 3775–3782. https://doi.org/10.1039/C5GC00194C.

(55) Yang, Z.; Lu, L.; Kiely, C. J.; Berger, B. W.; McIntosh, S. Single Enzyme Direct Biomineralization of CdSe and CdSe-CdS Core-Shell Quantum Dots. *ACS Appl. Mater. Interfaces* **2017**, *9* (15), 13430–13439. https://doi.org/10.1021/acsami.7b00133.

(56) Fox, B.; Walsh, C. T. Mercuric Reductase. Purification and Characterization of a Transposon-Encoded Flavoprotein Containing an Oxidation-Reduction-Active Disulfide. *Journal of Biological Chemistry* **1982**, *257* (5), 2498–2503. https://doi.org/10.1016/S0021-9258(18)34951-2.

(57) Engst, S.; Miller, S. M. Rapid Reduction of Hg(II) by Mercuric Ion Reductase Does Not Require the Conserved C-Terminal Cysteine Pair Using $HgBr_2$ as the Substrate. *Biochemistry* **1998**, *37* (33), 11496–11507. https://doi.org/10.1021/bi9808161.

(58) Freedman, Z.; Zhu, C.; Barkay, T. Mercury Resistance and Mercuric Reductase Activities and Expression among Chemotrophic Thermophilic Aquificae. *Appl Environ Microbiol* **2012**, *78* (18), 6568–6575. https://doi.org/10.1128/AEM.01060-12.

(59) Avazéri, C.; Turner, R. J.; Pommier, J.; Weiner, J. H.; Giordano, G.; Verméglio, A. Tellurite Reductase Activity of Nitrate Reductase Is Responsible for the Basal Resistance of Escherichia Coli to Tellurite. *Microbiology* **1997**, *143* (4), 1181–1189. https://doi.org/10.1099/00221287-143-4-1181.

(60) Sabaty, M.; Avazeri, C.; Pignol, D.; Vermeglio, A. Characterization of the Reduction of Selenate and Tellurite by Nitrate Reductases. *Appl Environ Microbiol* **2001**, *67* (11), 5122–5126. https://doi.org/10.1128/AEM.67.11.5122-5126.2001.

(61) Calderón, I. L.; Arenas, F. A.; Pérez, J. M.; Fuentes, D. E.; Araya, M. A.; Saavedra, C. P.; Tantaleán, J. C.; Pichuantes, S. E.; Youderian, P. A.; Vásquez, C. C. Catalases Are NAD(P)H-Dependent Tellurite Reductases. *PLoS ONE* **2006**, *1* (1), e70. https://doi.org/10.1371/journal.pone.0000070.

(62) Castro, M. E.; Molina, R.; Díaz, W.; Pichuantes, S. E.; Vásquez, C. C. The Dihydrolipoamide Dehydrogenase of Aeromonas Caviae ST Exhibits NADH-Dependent Tellurite Reductase Activity. *Biochemical and Biophysical Research Communications* **2008**, *375* (1), 91–94. https://doi.org/10.1016/j.bbrc.2008.07.119.

(63) Zhou, S.; Dong, L.; Deng, P.; Jia, Y.; Bai, Q.; Gao, J.; Xiao, H. Reducing Capacity and Enzyme Activity of Chromate Reductase in a ChrT-Engineered Strain. *Experimental and Therapeutic Medicine* **2017**, *14* (3), 2361–2366. https://doi.org/10.3892/etm.2017.4775.

(64) Turner, R. J.; Weiner, J. H.; Taylor, D. E. [No Title Found]. *BioMetals* **1998**, *11* (3), 223–227. https://doi.org/10.1023/A:1009290213301.

(65) Avendaño, R.; Chaves, N.; Fuentes, P.; Sánchez, E.; Jiménez, J. I.; Chavarría, M. Production of Selenium Nanoparticles in Pseudomonas Putida KT2440. *Sci Rep* **2016**, *6* (1), 37155. https://doi.org/10.1038/srep37155.

(66) Elahian, F.; Reiisi, S.; Shahidi, A.; Mirzaei, S. A. High-Throughput Bioaccumulation, Biotransformation, and Production of Silver and Selenium Nanoparticles Using Genetically Engineered Pichia Pastoris. *Nanomedicine: Nanotechnology, Biology and Medicine* **2017**, *13* (3), 853–861. https://doi.org/10.1016/j.nano.2016.10.009.

(67) Chasteen, T. G.; Fuentes, D. E.; Tantaleán, J. C.; Vásquez, C. C. Tellurite: History, Oxidative Stress, and Molecular Mechanisms of Resistance. *FEMS Microbiol Rev* **2009**, *33* (4), 820–832. https://doi.org/10.1111/j.1574-6976.2009.00177.x.

(68) Presentato, A.; Piacenza, E.; Darbandi, A.; Anikovskiy, M.; Cappelletti, M.; Zannoni, D.; Turner, R. J. Assembly, Growth and Conductive Properties of Tellurium Nanorods Produced by Rhodococcus Aetherivorans BCP1. *Sci Rep* **2018**, *8* (1), 3923. https://doi.org/10.1038/s41598-018-22320-x.

(69) Borghese, R.; Malferrari, M.; Brucale, M.; Ortolani, L.; Franchini, M.; Rapino, S.; Borsetti, F.; Zannoni, D. Structural and Electrochemical Characterization of Lawsone-Dependent Production of Tellurium-Metal Nanoprecipitates by Photosynthetic Cells of Rhodobacter Capsulatus. *Bioelectrochemistry* **2020**, *133*, 107456. https://doi.org/10.1016/j.bioelechem.2020.107456.

(70) Moore, M. D.; Kaplan, S. Identification of Intrinsic High-Level Resistance to Rare-Earth Oxides and Oxyanions in Members of the Class Proteobacteria: Characterization of Tellurite, Selenite, and Rhodium Sesquioxide Reduction in Rhodobacter Sphaeroides. *J Bacteriol* **1992**, *174* (5), 1505–1514. https://doi.org/10.1128/jb.174.5.1505-1514.1992.

(71) Maltman, C.; Donald, L. J.; Yurkov, V. Two Distinct Periplasmic Enzymes Are Responsible for Tellurite/Tellurate and Selenite Reduction by Strain ER-Te-48 Associated with the Deep Sea Hydrothermal Vent Tube Worms at the Juan de Fuca Ridge Black Smokers. *Arch Microbiol* **2017**, *199* (8), 1113–1120. https://doi.org/10.1007/s00203-017-1382-1.

(72) Maltman, C.; Donald, L.; Yurkov, V. Tellurite and Tellurate Reduction by the Aerobic Anoxygenic Phototroph Erythromonas Ursincola, Strain KR99 Is Carried out by a Novel Membrane Associated Enzyme. *Microorganisms* **2017**, *5* (2), 20. https://doi.org/10.3390/microorganisms5020020.

(73) Maltman, C.; Yurkov, V. Extreme Environments and High-Level Bacterial Tellurite Resistance. *Microorganisms* **2019**, *7* (12), 601. https://doi.org/10.3390/microorganisms7120601.

(74) *CRC Handbook of Chemistry and Physics: A Ready-Reference Book of Chemical and Physical Data*, 89. ed., 2008/2009.; Lide, D. R., Ed.; CRC, Taylor & Francis: Boca Raton, Fla., 2008.

(75) Nemeth, R.; Neubert, M.; Ni, T.; Ackerson, C. J. The Metalloid Reductase of Pseudomonas Moravenis Stanleyae Conveys Nanoparticle Mediated Metalloid Tolerance. **2018**. https://doi.org/10.26434/chemrxiv.6267383.v1.

(76) Komukai-Nakamura, S.; Sugiura, K.; Yamauchi-Inomata, Y.; Toki, H.; Venkateswaran, K.; Yamamoto, S.; Tanaka, H.; Harayama, S. Construction of Bacterial Consortia That Degrade Arabian Light Crude Oil. *Journal of Fermentation and Bioengineering* **1996**, *82* (6), 570–574. https://doi.org/10.1016/S0922-338X(97)81254-8.

(77) Sekine, M.; Tanikawa, S.; Omata, S.; Saito, M.; Fujisawa, T.; Tsukatani, N.; Tajima, T.; Sekigawa, T.; Kosugi, H.; Matsuo, Y.; Nishiko, R.; Imamura, K.; Ito, M.; Narita, H.; Tago, S.; Fujita, N.; Harayama, S. Sequence Analysis of Three Plasmids Harboured in Rhodococcus Erythropolis Strain PR4. *Environ Microbiol* **2006**, *8* (2), 334–346. https://doi.org/10.1111/j.1462-2920.2005.00899.x.

(78) Kelley, L. A.; Mezulis, S.; Yates, C. M.; Wass, M. N.; Sternberg, M. J. E. The Phyre2 Web Portal for Protein Modeling, Prediction and Analysis. *Nat Protoc* **2015**, *10* (6), 845–858. https://doi.org/10.1038/nprot.2015.053.

(79) Patel, M. P.; Blanchard, J. S. Expression, Purification, and Characterization of *Mycobacterium Tuberculosis* Mycothione Reductase. *Biochemistry* **1999**, *38* (36), 11827–11833. https://doi.org/10.1021/bi991025h.

(80) Kumar, A.; Nartey, W.; Shin, J.; Manimekalai, M. S. S.; Grüber, G. Structural and Mechanistic Insights into Mycothiol Disulphide Reductase and the Mycoredoxin-1-Alkylhydroperoxide Reductase E Assembly of Mycobacterium Tuberculosis. *Biochimica et Biophysica Acta (BBA) - General Subjects* **2017**, *1861* (9), 2354–2366. https://doi.org/10.1016/j.bbagen.2017.05.007.

(81) Kumar, A.; Subramanian Manimekalai, M. S.; Grüber, G. Substrate-induced Structural Alterations of Mycobacterial Mycothione Reductase and Critical Residues Involved. *FEBS Lett* **2018**, *592* (4), 568–585. https://doi.org/10.1002/1873-3468.12984.

(82) Chivers, T.; Laitinen, R. S. Tellurium: A Maverick among the Chalcogens. *Chem. Soc. Rev.* **2015**, *44* (7), 1725–1739. https://doi.org/10.1039/C4CS00434E.

(83) Liu, Z.; Hu, Z.; Xie, Q.; Yang, B.; Wu, J.; Qian, Y. Surfactant-Assisted Growth of Uniform Nanorods of Crystalline Tellurium. *J. Mater. Chem.* **2003**, *13* (1), 159–162. https://doi.org/10.1039/b208420a.

(84) Liu, Z.; Hu, Z.; Liang, J.; Li, S.; Yang, Y.; Peng, S.; Qian, Y. Size-Controlled Synthesis and Growth Mechanism of Monodisperse Tellurium Nanorods by a Surfactant-Assisted Method. *Langmuir* **2004**, *20* (1), 214–218. https://doi.org/10.1021/la035160d.

(85) Gautam, U. K.; Rao, C. N. R. Controlled Synthesis of Crystalline Tellurium Nanorods, Nanowires, Nanobelts and Related Structures by a Self-Seeding Solution Process. *J. Mater. Chem.* **2004**, *14* (16), 2530. https://doi.org/10.1039/b405006a.
(86) Saveliev, S. V.; Woodroofe, C. C.; Sabat, G.; Adams, C. M.; Klaubert, D.; Wood, K.; Urh, M. Mass Spectrometry Compatible Surfactant for Optimized In-Gel Protein Digestion. *Anal. Chem.* **2013**, *85* (2), 907–914. https://doi.org/10.1021/ac302423t.
(87) Scopes, R. K. Measurement of Protein by Spectrophotometry at 205 Nm. *Analytical Biochemistry* **1974**, *59* (1), 277–282. https://doi.org/10.1016/0003-2697(74)90034-7.
(88) Keller, A.; Nesvizhskii, A. I.; Kolker, E.; Aebersold, R. Empirical Statistical Model To Estimate the Accuracy of Peptide Identifications Made by MS/MS and Database Search. *Anal. Chem.* **2002**, *74* (20), 5383–5392. https://doi.org/10.1021/ac025747h.
(89) Searle, B. C.; Turner, M.; Nesvizhskii, A. I. Improving Sensitivity by Probabilistically Combining Results from Multiple MS/MS Search Methodologies. *J. Proteome Res.* **2008**, *7* (1), 245–253. https://doi.org/10.1021/pr070540w.
(90) Käll, L.; Storey, J. D.; MacCoss, M. J.; Noble, W. S. Assigning Significance to Peptides Identified by Tandem Mass Spectrometry Using Decoy Databases. *J. Proteome Res.* **2008**, *7* (1), 29–34. https://doi.org/10.1021/pr700600n.
(91) Nesvizhskii, A. I.; Keller, A.; Kolker, E.; Aebersold, R. A Statistical Model for Identifying Proteins by Tandem Mass Spectrometry. *Anal. Chem.* **2003**, *75* (17), 4646–4658. https://doi.org/10.1021/ac0341261.
(92) Esvelt, K. M.; Carlson, J. C.; Liu, D. R. A System for the Continuous Directed Evolution of Biomolecules. *Nature* **2011**, *472* (7344), 499–503. https://doi.org/10.1038/nature09929.
(93) Chen, K.; Arnold, F. H. Engineering New Catalytic Activities in Enzymes. *Nat Catal* **2020**, *3* (3), 203–213. https://doi.org/10.1038/s41929-019-0385-5.
(94) Engström, K.; Nyhlén, J.; Sandström, A. G.; Bäckvall, J.-E. Directed Evolution of an Enantioselective Lipase with Broad Substrate Scope for Hydrolysis of α-Substituted Esters. *J. Am. Chem. Soc.* **2010**, *132* (20), 7038–7042. https://doi.org/10.1021/ja100593j.
(95) Reetz, M. T. Directed Evolution of Enantioselective Enzymes: An Unconventional Approach to Asymmetric Catalysis in Organic Chemistry. *J. Org. Chem.* **2009**, *74* (16), 5767–5778. https://doi.org/10.1021/jo901046k.
(96) Prier, C. K.; Zhang, R. K.; Buller, A. R.; Brinkmann-Chen, S.; Arnold, F. H. Enantioselective, Intermolecular Benzylic C–H Amination Catalysed by an Engineered Iron-Haem Enzyme. *Nature Chem* **2017**, *9* (7), 629–634. https://doi.org/10.1038/nchem.2783.
(97) Ma, S. K.; Gruber, J.; Davis, C.; Newman, L.; Gray, D.; Wang, A.; Grate, J.; Huisman, G. W.; Sheldon, R. A. A Green-by-Design Biocatalytic Process for Atorvastatin Intermediate. *Green Chem.* **2010**, *12* (1), 81–86. https://doi.org/10.1039/B919115C.
(98) Bell, E. L.; Smithson, R.; Kilbride, S.; Foster, J.; Hardy, F. J.; Ramachandran, S.; Tedstone, A. A.; Haigh, S. J.; Garforth, A. A.; Day, P. J. R.; Levy, C.; Shaver, M. P.; Green, A. P. Directed Evolution of an Efficient and Thermostable PET Depolymerase. *Nat Catal* **2022**, *5* (8), 673–681. https://doi.org/10.1038/s41929-022-00821-3.
(99) Wu, S.; Xiang, C.; Zhou, Y.; Khan, M. S. H.; Liu, W.; Feiler, C. G.; Wei, R.; Weber, G.; Höhne, M.; Bornscheuer, U. T. A Growth Selection System for the Directed Evolution of Amine-Forming or Converting Enzymes. *Nat Commun* **2022**, *13* (1), 7458. https://doi.org/10.1038/s41467-022-35228-y.
(100) Vaud, S.; Pearcy, N.; Hanževački, M.; Van Hagen, A. M. W.; Abdelrazig, S.; Safo, L.; Ehsaan, M.; Jonczyk, M.; Millat, T.; Craig, S.; Spence, E.; Fothergill, J.; Bommareddy, R. R.; Colin, P.-Y.; Twycross, J.; Dalby, P. A.; Minton, N. P.; Jäger, C. M.; Kim, D.-H.; Yu, J.; Maness, P.-C.; Lynch, S.; Eckert, C. A.; Conradie, A.; Bryan, S. J. Engineering Improved Ethylene Production: Leveraging Systems Biology and

Adaptive Laboratory Evolution. *Metabolic Engineering* **2021**, *67*, 308–320. https://doi.org/10.1016/j.ymben.2021.07.001.

(101) Tran, J. R.; Paulson, D. I.; Moresco, J. J.; Adam, S. A.; Yates, J. R.; Goldman, R. D.; Zheng, Y. An APEX2 Proximity Ligation Method for Mapping Interactions with the Nuclear Lamina. *Journal of Cell Biology* **2021**, *220* (1), e202002129. https://doi.org/10.1083/jcb.202002129.

(102) Lam, S. S.; Martell, J. D.; Kamer, K. J.; Deerinck, T. J.; Ellisman, M. H.; Mootha, V. K.; Ting, A. Y. Directed Evolution of APEX2 for Electron Microscopy and Proximity Labeling. *Nat Methods* **2015**, *12* (1), 51–54. https://doi.org/10.1038/nmeth.3179.

(103) Xu, S.; Chisholm, A. D. Highly Efficient Optogenetic Cell Ablation in C. Elegans Using Membrane-Targeted MiniSOG. *Sci Rep* **2016**, *6* (1), 21271. https://doi.org/10.1038/srep21271.

(104) Li, Z.; Jiang, Y.; Guengerich, F. P.; Ma, L.; Li, S.; Zhang, W. Engineering Cytochrome P450 Enzyme Systems for Biomedical and Biotechnological Applications. *Journal of Biological Chemistry* **2020**, *295* (3), 833–849. https://doi.org/10.1016/S0021-9258(17)49939-X.

(105) Otey, C. R.; Bandara, G.; Lalonde, J.; Takahashi, K.; Arnold, F. H. Preparation of Human Metabolites of Propranolol Using Laboratory-Evolved Bacterial Cytochromes P450. *Biotechnol. Bioeng.* **2006**, *93* (3), 494–499. https://doi.org/10.1002/bit.20744.

(106) Zhou, Q.; Chin, M.; Fu, Y.; Liu, P.; Yang, Y. Stereodivergent Atom-Transfer Radical Cyclization by Engineered Cytochromes P450. *Science* **2021**, *374* (6575), 1612–1616. https://doi.org/10.1126/science.abk1603.

(107) Payne, J. T.; Poor, C. B.; Lewis, J. C. Directed Evolution of RebH for Site-Selective Halogenation of Large Biologically Active Molecules. *Angew. Chem. Int. Ed.* **2015**, *54* (14), 4226–4230. https://doi.org/10.1002/anie.201411901.

(108) Prakinee, K.; Phintha, A.; Visitsatthawong, S.; Lawan, N.; Sucharitakul, J.; Kantiwiriyawanitch, C.; Damborsky, J.; Chitnumsub, P.; Van Pée, K.-H.; Chaiyen, P. Mechanism-Guided Tunnel Engineering to Increase the Efficiency of a Flavin-Dependent Halogenase. *Nat Catal* **2022**, *5* (6), 534–544. https://doi.org/10.1038/s41929-022-00800-8.

(109) Snodgrass, H. M.; Mondal, D.; Lewis, J. C. Directed Evolution of Flavin-Dependent Halogenases for Site- and Atroposelective Halogenation of 3-Aryl-4(3 *H*)-Quinazolinones via Kinetic or Dynamic Kinetic Resolution. *J. Am. Chem. Soc.* **2022**, *144* (36), 16676–16682. https://doi.org/10.1021/jacs.2c07422.

(110) Jutz, G.; Van Rijn, P.; Santos Miranda, B.; Böker, A. Ferritin: A Versatile Building Block for Bionanotechnology. *Chem. Rev.* **2015**, *115* (4), 1653–1701. https://doi.org/10.1021/cr400011b.

(111) Haikarainen, T.; Papageorgiou, A. C. Dps-like Proteins: Structural and Functional Insights into a Versatile Protein Family. *Cell. Mol. Life Sci.* **2010**, *67* (3), 341–351. https://doi.org/10.1007/s00018-009-0168-2.

(112) Butterfield, C. N.; Soldatova, A. V.; Lee, S.-W.; Spiro, T. G.; Tebo, B. M. Mn(II,III) Oxidation and MnO_2 Mineralization by an Expressed Bacterial Multicopper Oxidase. *Proc. Natl. Acad. Sci. U.S.A.* **2013**, *110* (29), 11731–11735. https://doi.org/10.1073/pnas.1303677110.

(113) Soldatova, A. V.; Romano, C. A.; Tao, L.; Stich, T. A.; Casey, W. H.; Britt, R. D.; Tebo, B. M.; Spiro, T. G. Mn(II) Oxidation by the Multicopper Oxidase Complex Mnx: A Coordinated Two-Stage Mn(II)/(III) and Mn(III)/(IV) Mechanism. *J. Am. Chem. Soc.* **2017**, *139* (33), 11381–11391. https://doi.org/10.1021/jacs.7b02772.

(114) Liu, J.; Feng, L.; Wu, Y. Enzymatically Synthesised MnO_2 Nanoparticles for Efficient near-Infrared Photothermal Therapy and Dual-Responsive Magnetic Resonance Imaging. *Nanoscale* **2021**, *13* (25), 11093–11103. https://doi.org/10.1039/D1NR02400K.

(115) Dunleavy, R.; Lu, L.; Kiely, C. J.; McIntosh, S.; Berger, B. W. Single-Enzyme Biomineralization of Cadmium Sulfide Nanocrystals with Controlled Optical Properties. *Proc. Natl. Acad. Sci. U.S.A.* **2016**, *113* (19), 5275–5280. https://doi.org/10.1073/pnas.1523633113.

(116) Wang, Y.; Chen, H.; Huang, Z.; Yang, M.; Yu, H.; Peng, M.; Yang, Z.; Chen, S. Structural Characterization of Cystathionine γ-Lyase SmCSE Enables Aqueous Metal Quantum Dot Biosynthesis. *International Journal of Biological Macromolecules* **2021**, *174*, 42–51. https://doi.org/10.1016/j.ijbiomac.2021.01.141.

(117) Huang, S.; Chua, J. H.; Yew, W. S.; Sivaraman, J.; Moore, P. K.; Tan, C.-H.; Deng, L.-W. Site-Directed Mutagenesis on Human Cystathionine-γ-Lyase Reveals Insights into the Modulation of H2S Production. *Journal of Molecular Biology* **2010**, *396* (3), 708–718. https://doi.org/10.1016/j.jmb.2009.11.058.

(118) Staicu, L. C.; Ackerson, C. J.; Cornelis, P.; Ye, L.; Berendsen, R. L.; Hunter, W. J.; Noblitt, S. D.; Henry, C. S.; Cappa, J. J.; Montenieri, R. L.; Wong, A. O.; Musilova, L.; Sura-de Jong, M.; van Hullebusch, E. D.; Lens, P. N. L.; Reynolds, R. J. B.; Pilon-Smits, E. A. H. *Pseudomonas Moraviensis* Subsp. Stanleyae, a Bacterial Endophyte of Hyperaccumulator *Stanleya Pinnata* , Is Capable of Efficient Selenite Reduction to Elemental Selenium under Aerobic Conditions. *J Appl Microbiol* **2015**, *119* (2), 400–410. https://doi.org/10.1111/jam.12842.

(119) Nemeth, R.; Neubert, M.; Butz, Z. J.; Ni, T. W.; Ackerson, C. J. Metalloid Reductase of *Pseudomonas Moravenis* Stanleyae Conveys Nanoparticle Mediated Metalloid Tolerance. *ACS Omega* **2018**, *3* (11), 14902–14909. https://doi.org/10.1021/acsomega.8b00826.

(120) Butz, Z. J.; Borgognoni, K.; Nemeth, R.; Nilsson, Z. N.; Ackerson, C. J. Metalloid Reductase Activity Modified by a Fused Se ^{0} Binding Peptide. *ACS Chem. Biol.* **2020**, *15* (7), 1987–1995. https://doi.org/10.1021/acschembio.0c00387.

(121) Barak, Y.; Ackerley, D. F.; Dodge, C. J.; Banwari, L.; Alex, C.; Francis, A. J.; Matin, A. Analysis of Novel Soluble Chromate and Uranyl Reductases and Generation of an Improved Enzyme by Directed Evolution. *Appl Environ Microbiol* **2006**, *72* (11), 7074–7082. https://doi.org/10.1128/AEM.01334-06.

(122) Liu, X.; Lopez, P. A.; Giessen, T. W.; Giles, M.; Way, J. C.; Silver, P. A. Engineering Genetically-Encoded Mineralization and Magnetism via Directed Evolution. *Sci Rep* **2016**, *6* (1), 38019. https://doi.org/10.1038/srep38019.

(123) Rawlings, D. E. Heavy Metal Mining Using Microbes. *Annu. Rev. Microbiol.* **2002**, *56* (1), 65–91. https://doi.org/10.1146/annurev.micro.56.012302.161052.

(124) Gumulya, Y.; Boxall, N.; Khaleque, H.; Santala, V.; Carlson, R.; Kaksonen, A. In a Quest for Engineering Acidophiles for Biomining Applications: Challenges and Opportunities. *Genes* **2018**, *9* (2), 116. https://doi.org/10.3390/genes9020116.

(125) Hoque, E.; Fritscher, J. Multimetal Bioremediation and Biomining by a Combination of New Aquatic Strains of Mucor Hiemalis. *Sci Rep* **2019**, *9* (1), 10318. https://doi.org/10.1038/s41598-019-46560-7.

(126) Staicu, L. C.; van Hullebusch, E. D.; Ackerson, C. Editorial: Microbial Biominerals: Toward New Functions and Resource Recovery. *Front. Microbiol.* **2021**, *12*, 796374. https://doi.org/10.3389/fmicb.2021.796374.

(127) Verma, S.; Kuila, A. Bioremediation of Heavy Metals by Microbial Process. *Environmental Technology & Innovation* **2019**, *14*, 100369. https://doi.org/10.1016/j.eti.2019.100369.

(128) Shakibaie, M.; Amiri-Moghadam, P.; Ghazanfari, M.; Adeli-Sardou, M.; Jafari, M.; Forootanfar, H. Cytotoxic and Antioxidant Activity of the Biogenic Bismuth Nanoparticles Produced by Delftia Sp. SFG. *Materials Research Bulletin* **2018**, *104*, 155–163. https://doi.org/10.1016/j.materresbull.2018.04.001.

(129) Hendricks, A. R.; Guilliams, B. F.; Cohen, R. S.; Tien, T.; McEwen, G. A.; Borgognoni, K. M.; Ackerson, C. J. Cloneable Inorganic Nanoparticles. *Chem Comm Accepted June 2nd, 2023*. https://doi.org/10.1039/D3CC01319G.

(130) Lian, P.; Guo, H.-B.; Riccardi, D.; Dong, A.; Parks, J. M.; Xu, Q.; Pai, E. F.; Miller, S. M.; Wei, D.-Q.; Smith, J. C.; Guo, H. X-Ray Structure of a Hg^{2+} Complex of Mercuric Reductase (MerA) and Quantum Mechanical/Molecular Mechanical Study of Hg^{2+} Transfer between the C-Terminal and Buried Catalytic Site Cysteine Pairs. *Biochemistry* **2014**, *53* (46), 7211–7222. https://doi.org/10.1021/bi500608u.

(131) Distefano, M. D.; Au, K. G.; Walsh, C. T. Mutagenesis of the Redox-Active Disulfide in Mercuric Ion Reductase: Catalysis by Mutant Enzymes Restricted to Flavin Redox Chemistry. *Biochemistry* **1989**, *28* (3), 1168–1183. https://doi.org/10.1021/bi00429a035.

(132) Whaley, S. R.; English, D. S.; Hu, E. L.; Barbara, P. F.; Belcher, A. M. Selection of Peptides with Semiconductor Binding Specificity for Directed Nanocrystal Assembly. *Nature* **2000**, *405* (6787), 665–668. https://doi.org/10.1038/35015043.

(133) Naik, R. R.; Stringer, S. J.; Agarwal, G.; Jones, S. E.; Stone, M. O. Biomimetic Synthesis and Patterning of Silver Nanoparticles. *Nature Mater* **2002**, *1* (3), 169–172. https://doi.org/10.1038/nmat758.

(134) OriginPro. 2023. OriginLab Corporation, Northampton, MA., 2023.

(135) Pannala, V. R.; Bazil, J. N.; Camara, A. K. S.; Dash, R. K. A Biophysically Based Mathematical Model for the Catalytic Mechanism of Glutathione Reductase. *Free Radical Biology and Medicine* **2013**, *65*, 1385–1397. https://doi.org/10.1016/j.freeradbiomed.2013.10.001.

(136) Painter, E. P. The Chemistry and Toxicity of Selenium Compounds, with Special Reference to the Selenium Problem. *Chem. Rev.* **1941**, *28* (2), 179–213. https://doi.org/10.1021/cr60090a001.

(137) Jumper, J.; Evans, R.; Pritzel, A.; Green, T.; Figurnov, M.; Ronneberger, O.; Tunyasuvunakool, K.; Bates, R.; Žídek, A.; Potapenko, A.; Bridgland, A.; Meyer, C.; Kohl, S. A. A.; Ballard, A. J.; Cowie, A.; Romera-Paredes, B.; Nikolov, S.; Jain, R.; Adler, J.; Back, T.; Petersen, S.; Reiman, D.; Clancy, E.; Zielinski, M.; Steinegger, M.; Pacholska, M.; Berghammer, T.; Bodenstein, S.; Silver, D.; Vinyals, O.; Senior, A. W.; Kavukcuoglu, K.; Kohli, P.; Hassabis, D. Highly Accurate Protein Structure Prediction with AlphaFold. *Nature* **2021**, *596* (7873), 583–589. https://doi.org/10.1038/s41586-021-03819-2.

(138) Evans, R.; O'Neill, M.; Pritzel, A.; Antropova, N.; Senior, A.; Green, T.; Žídek, A.; Bates, R.; Blackwell, S.; Yim, J.; Ronneberger, O.; Bodenstein, S.; Zielinski, M.; Bridgland, A.; Potapenko, A.; Cowie, A.; Tunyasuvunakool, K.; Jain, R.; Clancy, E.; Kohli, P.; Jumper, J.; Hassabis, D. *Protein Complex Prediction with AlphaFold-Multimer*; preprint; Bioinformatics, 2021. https://doi.org/10.1101/2021.10.04.463034.

(139) Mirdita, M.; Schütze, K.; Moriwaki, Y.; Heo, L.; Ovchinnikov, S.; Steinegger, M. ColabFold: Making Protein Folding Accessible to All. *Nat Methods* **2022**, *19* (6), 679–682. https://doi.org/10.1038/s41592-022-01488-1.

(140) Mirdita, M.; Steinegger, M.; Söding, J. MMseqs2 Desktop and Local Web Server App for Fast, Interactive Sequence Searches. *Bioinformatics* **2019**, *35* (16), 2856–2858. https://doi.org/10.1093/bioinformatics/bty1057.

(141) Berman, H.; Henrick, K.; Nakamura, H. Announcing the Worldwide Protein Data Bank. *Nat Struct Mol Biol* **2003**, *10* (12), 980–980. https://doi.org/10.1038/nsb1203-980.

(142) Steinegger, M.; Meier, M.; Mirdita, M.; Vöhringer, H.; Haunsberger, S. J.; Söding, J. HH-Suite3 for Fast Remote Homology Detection and Deep Protein Annotation. *BMC Bioinformatics* **2019**, *20* (1), 473. https://doi.org/10.1186/s12859-019-3019-7.

(143) The PyMOL Molecular Graphics System, Version 2.5.5, Schrödinger, LLC.

(144) Bornhorst, J. A.; Falke, J. J. [16] Purification of Proteins Using Polyhistidine Affinity Tags. In *Methods in Enzymology*; Elsevier, 2000; Vol. 326, pp 245–254. https://doi.org/10.1016/S0076-6879(00)26058-8.

(145) Riskowski, R. A.; Nemeth, R. S.; Borgognoni, K.; Ackerson, C. J. Enzyme-Catalyzed in Situ Synthesis of Temporally and Spatially Distinct CdSe Quantum Dots in Biological Backgrounds. *J. Phys. Chem. C* **2019**, *123* (44), 27187–27195. https://doi.org/10.1021/acs.jpcc.9b05519.

(146) Cadwell, R. C.; Joyce, G. F. Randomization of Genes by PCR Mutagenesis. *Genome Res.* **1992**, *2* (1), 28–33. https://doi.org/10.1101/gr.2.1.28.
(147) Hunter, W. J.; Manter, D. K. Reduction of Selenite to Elemental Red Selenium by Pseudomonas Sp. Strain CA5. *Curr Microbiol* **2009**, *58* (5), 493–498. https://doi.org/10.1007/s00284-009-9358-2.
(148) Dieudonné, A.; Pignol, D.; Prévéral, S. Magnetosomes: Biogenic Iron Nanoparticles Produced by Environmental Bacteria. *Appl Microbiol Biotechnol* **2019**, *103* (9), 3637–3649. https://doi.org/10.1007/s00253-019-09728-9.
(149) Jogler, C.; Lin, W.; Meyerdierks, A.; Kube, M.; Katzmann, E.; Flies, C.; Pan, Y.; Amann, R.; Reinhardt, R.; Schüler, D. Toward Cloning of the Magnetotactic Metagenome: Identification of Magnetosome Island Gene Clusters in Uncultivated Magnetotactic Bacteria from Different Aquatic Sediments. *Appl Environ Microbiol* **2009**, *75* (12), 3972–3979. https://doi.org/10.1128/AEM.02701-08.
(150) Clarke, N. I.; Royle, S. J. FerriTag Is a New Genetically-Encoded Inducible Tag for Correlative Light-Electron Microscopy. *Nat Commun* **2018**, *9* (1), 2604. https://doi.org/10.1038/s41467-018-04993-0.
(151) Jiang, B.; Fang, L.; Wu, K.; Yan, X.; Fan, K. Ferritins as Natural and Artificial Nanozymes for Theranostics. *Theranostics* **2020**, *10* (2), 687–706. https://doi.org/10.7150/thno.39827.
(152) Karas, V. O.; Westerlaken, I.; Meyer, A. S. The DNA-Binding Protein from Starved Cells (Dps) Utilizes Dual Functions To Defend Cells against Multiple Stresses. *J Bacteriol* **2015**, *197* (19), 3206–3215. https://doi.org/10.1128/JB.00475-15.
(153) Orban, K.; Finkel, S. E. Dps Is a Universally Conserved Dual-Action DNA-Binding and Ferritin Protein. *J Bacteriol* **2022**, *204* (5), e00036-22. https://doi.org/10.1128/jb.00036-22.
(154) Mughal, B.; Zaidi, S. Z. J.; Zhang, X.; Hassan, S. U. Biogenic Nanoparticles: Synthesis, Characterisation and Applications. *Applied Sciences* **2021**, *11* (6), 2598. https://doi.org/10.3390/app11062598.
(155) Choi, Y.; Lee, S. Y. Biosynthesis of Inorganic Nanomaterials Using Microbial Cells and Bacteriophages. *Nat Rev Chem* **2020**, *4* (12), 638–656. https://doi.org/10.1038/s41570-020-00221-w.
(156) Hemmati, S.; Retzlaff-Roberts, E.; Scott, C.; Harris, M. T. Artificial Sweeteners and Sugar Ingredients as Reducing Agent for Green Synthesis of Silver Nanoparticles. *Journal of Nanomaterials* **2019**, *2019*, 1–16. https://doi.org/10.1155/2019/9641860.
(157) Shankar, S.; Rhim, J.-W. Amino Acid Mediated Synthesis of Silver Nanoparticles and Preparation of Antimicrobial Agar/Silver Nanoparticles Composite Films. *Carbohydrate Polymers* **2015**, *130*, 353–363. https://doi.org/10.1016/j.carbpol.2015.05.018.
(158) Carter, C. J.; Dolska, M.; Owczarek, A.; Ackerson, C. J.; Eaton, B. E.; Feldheim, D. L. In Vitro Selection of RNA Sequences Capable of Mediating the Formation of Iron Oxide Nanoparticles. *J. Mater. Chem.* **2009**, *19* (44), 8320. https://doi.org/10.1039/b912423c.
(159) Naik, R. R.; Jones, S. E.; Murray, C. J.; McAuliffe, J. C.; Vaia, R. A.; Stone, M. O. Peptide Templates for Nanoparticle Synthesis Derived from Polymerase Chain Reaction-Driven Phage Display. *Adv. Funct. Mater.* **2004**, *14* (1), 25–30. https://doi.org/10.1002/adfm.200304501.
(160) Md Ishak, N. A. I.; Kamarudin, S. K.; Timmiati, S. N. Green Synthesis of Metal and Metal Oxide Nanoparticles via Plant Extracts: An Overview. *Mater. Res. Express* **2019**, *6* (11), 112004. https://doi.org/10.1088/2053-1591/ab4458.
(161) Capeness, M. J.; Echavarri-Bravo, V.; Horsfall, L. E. Production of Biogenic Nanoparticles for the Reduction of 4-Nitrophenol and Oxidative Laccase-Like Reactions. *Front. Microbiol.* **2019**, *10*, 997. https://doi.org/10.3389/fmicb.2019.00997.
(162) Sawant, S. Y.; Sayed, M. S.; Han, T. H.; Karim, M. R.; Shim, J.-J.; Cho, M. H. Bio-Synthesis of Finely Distributed Ag Nanoparticle-Decorated TiO2 Nanorods for Sunlight-Induced Photoelectrochemical Water Splitting. *Journal of Industrial and Engineering Chemistry* **2019**, *69*, 48–56. https://doi.org/10.1016/j.jiec.2018.09.002.
(163) Singh, P.; Garg, A.; Pandit, S.; Mokkapati, V.; Mijakovic, I. Antimicrobial Effects of Biogenic Nanoparticles. *Nanomaterials* **2018**, *8* (12), 1009. https://doi.org/10.3390/nano8121009.

(164) Fayaz, A. M.; Balaji, K.; Girilal, M.; Yadav, R.; Kalaichelvan, P. T.; Venketesan, R. Biogenic Synthesis of Silver Nanoparticles and Their Synergistic Effect with Antibiotics: A Study against Gram-Positive and Gram-Negative Bacteria. *Nanomedicine: Nanotechnology, Biology and Medicine* **2010**, *6* (1), 103–109. https://doi.org/10.1016/j.nano.2009.04.006.
(165) Zambonino, M. C.; Quizhpe, E. M.; Mouheb, L.; Rahman, A.; Agathos, S. N.; Dahoumane, S. A. Biogenic Selenium Nanoparticles in Biomedical Sciences: Properties, Current Trends, Novel Opportunities and Emerging Challenges in Theranostic Nanomedicine. *Nanomaterials* **2023**, *13* (3), 424. https://doi.org/10.3390/nano13030424.
(166) Nayak, V.; Singh, K. R.; Verma, R.; Pandey, M. D.; Singh, J.; Pratap Singh, R. Recent Advancements of Biogenic Iron Nanoparticles in Cancer Theranostics. *Materials Letters* **2022**, *313*, 131769. https://doi.org/10.1016/j.matlet.2022.131769.
(167) Heuer-Jungemann, A.; Feliu, N.; Bakaimi, I.; Hamaly, M.; Alkilany, A.; Chakraborty, I.; Masood, A.; Casula, M. F.; Kostopoulou, A.; Oh, E.; Susumu, K.; Stewart, M. H.; Medintz, I. L.; Stratakis, E.; Parak, W. J.; Kanaras, A. G. The Role of Ligands in the Chemical Synthesis and Applications of Inorganic Nanoparticles. *Chem. Rev.* **2019**, *119* (8), 4819–4880. https://doi.org/10.1021/acs.chemrev.8b00733.
(168) Jozefczak, M.; Remans, T.; Vangronsveld, J.; Cuypers, A. Glutathione Is a Key Player in Metal-Induced Oxidative Stress Defenses. *IJMS* **2012**, *13* (3), 3145–3175. https://doi.org/10.3390/ijms13033145.
(169) Mittl, P. R. E.; Schulz, G. E. Structure of Glutathione Reductase from Escherichia Coli at 1.86 Å Resolution: Comparison with the Enzyme from Human Erythrocytes. *Protein Science* **2008**, *3* (5), 799–809. https://doi.org/10.1002/pro.5560030509.
(170) Carlberg, I.; Mannervik, B. [59] Glutathione Reductase. In *Methods in Enzymology*; Elsevier, 1985; Vol. 113, pp 484–490. https://doi.org/10.1016/S0076-6879(85)13062-4.
(171) Mukhopadhyay, R.; Rosen, B. P. Arsenate Reductases in Prokaryotes and Eukaryotes. *Environmental Health Perspectives* **2002**, *110* (suppl 5), 745–748. https://doi.org/10.1289/ehp.02110s5745.
(172) Thatoi, H.; Das, S.; Mishra, J.; Rath, B. P.; Das, N. Bacterial Chromate Reductase, a Potential Enzyme for Bioremediation of Hexavalent Chromium: A Review. *Journal of Environmental Management* **2014**, *146*, 383–399. https://doi.org/10.1016/j.jenvman.2014.07.014.
(173) Bruins, M. R.; Kapil, S.; Oehme, F. W. Microbial Resistance to Metals in the Environment. *Ecotoxicology and Environmental Safety* **2000**, *45* (3), 198–207. https://doi.org/10.1006/eesa.1999.1860.
(174) Carter, C. J.; Ackerson, C. J.; Feldheim, D. L. Unusual Reactivity of a Silver Mineralizing Peptide. *ACS Nano* **2010**, *4* (7), 3883–3888. https://doi.org/10.1021/nn100630v.
(175) Chandra, K.; Culver, K. S. B.; Werner, S. E.; Lee, R. C.; Odom, T. W. Manipulating the Anisotropic Structure of Gold Nanostars Using Good's Buffers. *Chem. Mater.* **2016**, *28* (18), 6763–6769. https://doi.org/10.1021/acs.chemmater.6b03242.
(176) Xie, J.; Lee, J. Y.; Wang, D. I. C. Seedless, Surfactantless, High-Yield Synthesis of Branched Gold Nanocrystals in HEPES Buffer Solution. *Chem. Mater.* **2007**, *19* (11), 2823–2830. https://doi.org/10.1021/cm0700100.
(177) Arakaki, A.; Webb, J.; Matsunaga, T. A Novel Protein Tightly Bound to Bacterial Magnetic Particles in Magnetospirillum Magneticum Strain AMB-1. *Journal of Biological Chemistry* **2003**, *278* (10), 8745–8750. https://doi.org/10.1074/jbc.M211729200.
(178) Kashyap, S.; Woehl, T. J.; Liu, X.; Mallapragada, S. K.; Prozorov, T. Nucleation of Iron Oxide Nanoparticles Mediated by Mms6 Protein *in Situ*. *ACS Nano* **2014**, *8* (9), 9097–9106. https://doi.org/10.1021/nn502551y.
(179) Kolinko, I.; Lohße, A.; Borg, S.; Raschdorf, O.; Jogler, C.; Tu, Q.; Pósfai, M.; Tompa, É.; Plitzko, J. M.; Brachmann, A.; Wanner, G.; Müller, R.; Zhang, Y.; Schüler, D. Biosynthesis of Magnetic

Nanostructures in a Foreign Organism by Transfer of Bacterial Magnetosome Gene Clusters. *Nature Nanotech* **2014**, *9* (3), 193–197. https://doi.org/10.1038/nnano.2014.13.
(180) Komeili, A.; Li, Z.; Newman, D. K.; Jensen, G. J. Magnetosomes Are Cell Membrane Invaginations Organized by the Actin-Like Protein MamK. *Science* **2006**, *311* (5758), 242–245. https://doi.org/10.1126/science.1123231.
(181) Bradley, J. M.; Svistunenko, D. A.; Wilson, M. T.; Hemmings, A. M.; Moore, G. R.; Le Brun, N. E. Bacterial Iron Detoxification at the Molecular Level. *Journal of Biological Chemistry* **2020**, *295* (51), 17602–17623. https://doi.org/10.1074/jbc.REV120.007746.
(182) Payne, C. K. A Protein Corona Primer for Physical Chemists. *J. Chem. Phys.* **2019**, *151* (13), 130901. https://doi.org/10.1063/1.5120178.
(183) Pino, P. del; Pelaz, B.; Zhang, Q.; Maffre, P.; Nienhaus, G. U.; Parak, W. J. Protein Corona Formation around Nanoparticles – from the Past to the Future. *Mater. Horiz.* **2014**, *1* (3), 301–313. https://doi.org/10.1039/C3MH00106G.
(184) Lenz, M.; Kolvenbach, B.; Gygax, B.; Moes, S.; Corvini, P. F. X. Shedding Light on Selenium Biomineralization: Proteins Associated with Bionanominerals. *Appl. Environ. Microbiol.* **2011**, *77* (13), 4676–4680. https://doi.org/10.1128/AEM.01713-10.
(185) Shimomura, O. Structure of the Chromophore of *Aequorea* Green Fluorescent Protein. *FEBS Letters* **1979**, *104* (2), 220–222. https://doi.org/10.1016/0014-5793(79)80818-2.
(186) Chalfie, M.; Tu, Y.; Euskirchen, G.; Ward, W.; Prasher, D. Green Fluorescent Protein as a Marker for Gene Expression. *Science* **1994**, *263* (5148), 802–805. https://doi.org/10.1126/science.8303295.
(187) Chudakov, D. M.; Matz, M. V.; Lukyanov, S.; Lukyanov, K. A. Fluorescent Proteins and Their Applications in Imaging Living Cells and Tissues. *Physiological Reviews* **2010**, *90* (3), 1103–1163. https://doi.org/10.1152/physrev.00038.2009.
(188) Lam, S. S.; Martell, J. D.; Kamer, K. J.; Deerinck, T. J.; Ellisman, M. H.; Mootha, V. K.; Ting, A. Y. Directed Evolution of APEX2 for Electron Microscopy and Proximity Labeling. *Nat Methods* **2015**, *12* (1), 51–54. https://doi.org/10.1038/nmeth.3179.
(189) Mercogliano, C. P.; DeRosier, D. J. Concatenated Metallothionein as a Clonable Gold Label for Electron Microscopy. *Journal of Structural Biology* **2007**, *160* (1), 70–82. https://doi.org/10.1016/j.jsb.2007.06.010.
(190) Lu, G. J.; Farhadi, A.; Szablowski, J. O.; Lee-Gosselin, A.; Barnes, S. R.; Lakshmanan, A.; Bourdeau, R. W.; Shapiro, M. G. Acoustically Modulated Magnetic Resonance Imaging of Gas-Filled Protein Nanostructures. *Nature Mater* **2018**, *17* (5), 456–463. https://doi.org/10.1038/s41563-018-0023-7.
(191) Mingos, D. M. P.; Wales, D. J. *Introduction to Cluster Chemistry*; Prentice Hall advanced reference series; Prentice Hall: Englewood Cliffs, N.J, 1990.
(192) Scott, D.; Toney, M.; Muzikár, M. Harnessing the Mechanism of Glutathione Reductase for Synthesis of Active Site Bound Metallic Nanoparticles and Electrical Connection to Electrodes. *J. Am. Chem. Soc.* **2008**, *130* (3), 865–874. https://doi.org/10.1021/ja074660g.
(193) Mavis, R. D.; Stellwagen, E. Purification and Subunit Structure of Glutathione Reductase from Bakers' Yeast. *Journal of Biological Chemistry* **1968**, *243* (4), 809–814. https://doi.org/10.1016/S0021-9258(19)81737-4.
(194) Yu, J.; Zhou, C.-Z. Crystal Structure of Glutathione Reductase Glr1 from the Yeast Saccharomyces Cerevisiae. *Proteins* **2007**, *68* (4), 972–979. https://doi.org/10.1002/prot.21354.
(195) Adams, S. R.; Mackey, M. R.; Ramachandra, R.; Palida Lemieux, S. F.; Steinbach, P.; Bushong, E. A.; Butko, M. T.; Giepmans, B. N. G.; Ellisman, M. H.; Tsien, R. Y. Multicolor Electron Microscopy for Simultaneous Visualization of Multiple Molecular Species. *Cell Chemical Biology* **2016**, *23* (11), 1417–1427. https://doi.org/10.1016/j.chembiol.2016.10.006.

(196) Scotuzzi, M.; Kuipers, J.; Wensveen, D. I.; de Boer, P.; Hagen, K. W.; Hoogenboom, J. P.; Giepmans, B. N. G. Multi-Color Electron Microscopy by Element-Guided Identification of Cells, Organelles and Molecules. *Sci Rep* **2017**, *7* (1), 45970. https://doi.org/10.1038/srep45970.
(197) Hamedi, S.; Ghaseminezhad, M.; Shokrollahzadeh, S.; Shojaosadati, S. A. Controlled Biosynthesis of Silver Nanoparticles Using Nitrate Reductase Enzyme Induction of Filamentous Fungus and Their Antibacterial Evaluation. *Artificial Cells, Nanomedicine, and Biotechnology* **2017**, *45* (8), 1588–1596. https://doi.org/10.1080/21691401.2016.1267011.
(198) Morphew, M.; He, W.; Bjorkman, P. J.; McINTOSH, J. R. Silver Enhancement of Nanogold Particles during Freeze Substitution for Electron Microscopy: ENHANCEMENT OF NANOGOLD DURING FREEZE SUBSTITUTION. *Journal of Microscopy* **2008**, *230* (2), 263–267. https://doi.org/10.1111/j.1365-2818.2008.01983.x.
(199) Choi, Y.; Park, T. J.; Lee, D. C.; Lee, S. Y. Recombinant *Escherichia Coli* as a Biofactory for Various Single- and Multi-Element Nanomaterials. *Proc. Natl. Acad. Sci. U.S.A.* **2018**, *115* (23), 5944–5949. https://doi.org/10.1073/pnas.1804543115.
(200) Carothers, D. J.; Pons, G.; Patel, M. S. Dihydrolipoamide Dehydrogenase: Functional Similarities and Divergent Evolution of the Pyridine Nucleotide-Disulfide Oxidoreductases. *Archives of Biochemistry and Biophysics* **1989**, *268* (2), 409–425. https://doi.org/10.1016/0003-9861(89)90309-3.
(201) Swulius, M. T.; Jensen, G. J. The Helical MreB Cytoskeleton in Escherichia Coli MC1000/PLE7 Is an Artifact of the N-Terminal Yellow Fluorescent Protein Tag. *J Bacteriol* **2012**, *194* (23), 6382–6386. https://doi.org/10.1128/JB.00505-12.
(202) Huang, Z.; Zhang, C.; Chen, S.; Ye, F.; Xing, X.-H. Active Inclusion Bodies of Acid Phosphatase PhoC: Aggregation Induced by GFP Fusion and Activities Modulated by Linker Flexibility. *Microb Cell Fact* **2013**, *12* (1), 25. https://doi.org/10.1186/1475-2859-12-25.
(203) Mirzaei, S. A.; Yazdi, M. T.; Sepehrizadeh, Z. Secretory Expression and Purification of a Soluble NADH Cytochrome B5 Reductase Enzyme from Mucor Racemosus in Pichia Pastoris Based on Codon Usage Adaptation. *Biotechnol Lett* **2010**, *32* (11), 1705–1711. https://doi.org/10.1007/s10529-010-0348-z.
(204) Setayesh, N. A.; Sepehrizadeh, Z.; Jaberi, E.; Yazdi, M. T. Cloning, Molecular Characterization and Expression of a CDNA Encoding a Functional NADH-Cytochrome B5 Reductase from Mucor Racemosus PTCC 5305 in E. Coli. *Biol. Res.* **2009**, *42* (2). https://doi.org/10.4067/S0716-97602009000200001.
(205) Presley, J. F.; Cole, N. B.; Schroer, T. A.; Hirschberg, K.; Zaal, K. J. M.; Lippincott-Schwartz, J. ER-to-Golgi Transport Visualized in Living Cells. *Nature* **1997**, *389* (6646), 81–85. https://doi.org/10.1038/38001.
(206) Bates, M.; Huang, B.; Dempsey, G. T.; Zhuang, X. Multicolor Super-Resolution Imaging with Photo-Switchable Fluorescent Probes. *Science* **2007**, *317* (5845), 1749–1753. https://doi.org/10.1126/science.1146598.
(207) Heim, R.; Tsien, R. Y. Engineering Green Fluorescent Protein for Improved Brightness, Longer Wavelengths and Fluorescence Resonance Energy Transfer. *Current Biology* **1996**, *6* (2), 178–182. https://doi.org/10.1016/S0960-9822(02)00450-5.
(208) Schnell, U.; Dijk, F.; Sjollema, K. A.; Giepmans, B. N. G. Immunolabeling Artifacts and the Need for Live-Cell Imaging. *Nat Methods* **2012**, *9* (2), 152–158. https://doi.org/10.1038/nmeth.1855.
(209) Goedhart, J.; Von Stetten, D.; Noirclerc-Savoye, M.; Lelimousin, M.; Joosen, L.; Hink, M. A.; Van Weeren, L.; Gadella, T. W. J.; Royant, A. Structure-Guided Evolution of Cyan Fluorescent Proteins towards a Quantum Yield of 93%. *Nat Commun* **2012**, *3* (1), 751. https://doi.org/10.1038/ncomms1738.
(210) *Scanning Electron Microscopy and X-Ray Microanalysis*, 3rd ed.; Goldstein, J., Ed.; Kluwer Academic/Plenum Publishers: New York, 2003.

(211) Sigmund, F.; Pettinger, S.; Kube, M.; Schneider, F.; Schifferer, M.; Schneider, S.; Efremova, M. V.; Pujol-Martí, J.; Aichler, M.; Walch, A.; Misgeld, T.; Dietz, H.; Westmeyer, G. G. Iron-Sequestering Nanocompartments as Multiplexed Electron Microscopy Gene Reporters. *ACS Nano* **2019**, *13* (7), 8114–8123. https://doi.org/10.1021/acsnano.9b03140.

(212) Wu, S.-C.; Wong, S.-L. Engineering Soluble Monomeric Streptavidin with Reversible Biotin Binding Capability. *Journal of Biological Chemistry* **2005**, *280* (24), 23225–23231. https://doi.org/10.1074/jbc.M501733200.

(213) Ruff, A. J.; Dennig, A.; Wirtz, G.; Blanusa, M.; Schwaneberg, U. Flow Cytometer-Based High-Throughput Screening System for Accelerated Directed Evolution of P450 Monooxygenases. *ACS Catal.* **2012**, *2* (12), 2724–2728. https://doi.org/10.1021/cs300115d.

(214) Black, C. B.; Duensing, T. D.; Trinkle, L. S.; Dunlay, R. T. Cell-Based Screening Using High-Throughput Flow Cytometry. *ASSAY and Drug Development Technologies* **2011**, *9* (1), 13–20. https://doi.org/10.1089/adt.2010.0308.

(215) Khalid, A.; Tran, P. A.; Norello, R.; Simpson, D. A.; O'Connor, A. J.; Tomljenovic-Hanic, S. Intrinsic Fluorescence of Selenium Nanoparticles for Cellular Imaging Applications. *Nanoscale* **2016**, *8* (6), 3376–3385. https://doi.org/10.1039/C5NR08771F.

(216) Bi, H.; He, F.; Dong, Y.; Yang, D.; Dai, Y.; Xu, L.; Lv, R.; Gai, S.; Yang, P.; Lin, J. Bismuth Nanoparticles with "Light" Property Served as a Multifunctional Probe for X-Ray Computed Tomography and Fluorescence Imaging. *Chem. Mater.* **2018**, *30* (10), 3301–3307. https://doi.org/10.1021/acs.chemmater.8b00565.

(217) Xu, C.; Zhou, T.; Kuroda, M.; Rosen, B. P. Metalloid Resistance Mechanisms in Prokaryotes. *Journal of Biochemistry* **1998**, *123* (1), 16–23. https://doi.org/10.1093/oxfordjournals.jbchem.a021904.

(218) Staicu, L. C.; Barton, L. L. Bacterial Metabolism of Selenium—For Survival or Profit. In *Bioremediation of Selenium Contaminated Wastewater*; Van Hullebusch, E. D., Ed.; Springer International Publishing: Cham, 2017; pp 1–31. https://doi.org/10.1007/978-3-319-57831-6_1.

(219) Becton, Dickson and Company. FlowJo Software, 2023.

(220) Chapman, A. M.; McNaughton, B. R. Scratching the Surface: Resurfacing Proteins to Endow New Properties and Function. *Cell Chemical Biology* **2016**, *23* (5), 543–553. https://doi.org/10.1016/j.chembiol.2016.04.010.

(221) Leistler, B.; Perham, R. N. Solubilizing Buried Domains of Proteins: A Self-Assembling Interface Domain from Glutathione Reductase. *Biochemistry* **1994**, *33* (10), 2773–2781. https://doi.org/10.1021/bi00176a005.

(222) Trevino, S. R.; Scholtz, J. M.; Pace, C. N. Amino Acid Contribution to Protein Solubility: Asp, Glu, and Ser Contribute More Favorably than the Other Hydrophilic Amino Acids in RNase Sa. *Journal of Molecular Biology* **2007**, *366* (2), 449–460. https://doi.org/10.1016/j.jmb.2006.10.026.

(223) Abraham, M. J.; Murtola, T.; Schulz, R.; Páll, S.; Smith, J. C.; Hess, B.; Lindahl, E. GROMACS: High Performance Molecular Simulations through Multi-Level Parallelism from Laptops to Supercomputers. *SoftwareX* **2015**, *1–2*, 19–25. https://doi.org/10.1016/j.softx.2015.06.001.

(224) Loksha, I. V.; Maiolo, J. R.; Hong, C. W.; Ng, A.; Snow, C. D. SHARPEN-Systematic Hierarchical Algorithms for Rotamers and Proteins on an Extended Network. *J. Comput. Chem.* **2009**, *30* (6), 999–1005. https://doi.org/10.1002/jcc.21204.

(225) Fu, H.; Liang, Y.; Zhong, X.; Pan, Z.; Huang, L.; Zhang, H.; Xu, Y.; Zhou, W.; Liu, Z. Codon Optimization with Deep Learning to Enhance Protein Expression. *Sci Rep* **2020**, *10* (1), 17617. https://doi.org/10.1038/s41598-020-74091-z.

(226) Tegel, H.; Tourle, S.; Ottosson, J.; Persson, A. Increased Levels of Recombinant Human Proteins with the Escherichia Coli Strain Rosetta(DE3). *Protein Expression and Purification* **2010**, *69* (2), 159–167. https://doi.org/10.1016/j.pep.2009.08.017.

(227) Wang, J.; Lisanza, S.; Juergens, D.; Tischer, D.; Watson, J. L.; Castro, K. M.; Ragotte, R.; Saragovi, A.; Milles, L. F.; Baek, M.; Anishchenko, I.; Yang, W.; Hicks, D. R.; Expòsit, M.; Schlichthaerle, T.; Chun, J.-H.; Dauparas, J.; Bennett, N.; Wicky, B. I. M.; Muenks, A.; DiMaio, F.; Correia, B.; Ovchinnikov, S.; Baker, D. Scaffolding Protein Functional Sites Using Deep Learning. *Science* **2022**, *377* (6604), 387–394. https://doi.org/10.1126/science.abn2100.

(228) Hoegler, K. J.; Hecht, M. H. A de Novo Protein Confers Copper Resistance in Escherichia Coli: Novel Protein Confers Copper Resistance. *Protein Science* **2016**, *25* (7), 1249–1259. https://doi.org/10.1002/pro.2871.

(229) Spangler, L. C.; Yao, Y.; Cheng, G.; Yao, N.; Chari, S. L.; Scholes, G. D.; Hecht, M. H. A de Novo Protein Catalyzes the Synthesis of Semiconductor Quantum Dots. *Proc. Natl. Acad. Sci. U.S.A.* **2022**, *119* (51), e2204050119. https://doi.org/10.1073/pnas.2204050119.

(230) Laczi, K.; Kis, Á.; Horváth, B.; Maróti, G.; Hegedüs, B.; Perei, K.; Rákhely, G. Metabolic Responses of Rhodococcus Erythropolis PR4 Grown on Diesel Oil and Various Hydrocarbons. *Appl. Microbiol. Biotechnol.* **2015**, *99* (22), 9745–9759. https://doi.org/10.1007/s00253-015-6936-z.

(231) Singhi, D.; Jain, A.; Srivastava, P. Localization of Low Copy Number Plasmid PRC4 in Replicating Rod and Non-Replicating Cocci Cells of Rhodococcus Erythropolis PR4. *PLoS ONE* **2016**, *11* (12), e0166491. https://doi.org/10.1371/journal.pone.0166491.

(232) Bosello, M.; Zeyadi, M.; Kraas, F. I.; Linne, U.; Xie, X.; Marahiel, M. A. Structural Characterization of the Heterobactin Siderophores from Rhodococcus Erythropolis PR4 and Elucidation of Their Biosynthetic Machinery. *J. Nat. Prod.* **2013**, *76* (12), 2282–2290. https://doi.org/10.1021/np4006579.

(233) van der Geize, R.; Dijkhuizen, L. Harnessing the Catabolic Diversity of Rhodococci for Environmental and Biotechnological Applications. *Current Opinion in Microbiology* **2004**, *7* (3), 255–261. https://doi.org/10.1016/j.mib.2004.04.001.

(234) Larkin, M. J.; Kulakov, L. A.; Allen, C. C. Biodegradation and Rhodococcus – Masters of Catabolic Versatility. *Current Opinion in Biotechnology* **2005**, *16* (3), 282–290. https://doi.org/10.1016/j.copbio.2005.04.007.

(235) Sekine, M.; Tanikawa, S.; Omata, S.; Saito, M.; Fujisawa, T.; Tsukatani, N.; Tajima, T.; Sekigawa, T.; Kosugi, H.; Matsuo, Y.; Nishiko, R.; Imamura, K.; Ito, M.; Narita, H.; Tago, S.; Fujita, N.; Harayama, S. Sequence Analysis of Three Plasmids Harboured in Rhodococcus Erythropolis Strain PR4. *Environmental Microbiology* **2006**, *8* (2), 334–346. https://doi.org/10.1111/j.1462-2920.2005.00899.x.

(236) Nies, D. H. Efflux-Mediated Heavy Metal Resistance in Prokaryotes. *FEMS Microbiol. Rev.* **2003**, *27* (2–3), 313–339. https://doi.org/10.1016/S0168-6445(03)00048-2.

(237) Crupper, S. S.; Worrell, V.; Stewart, G. C.; Iandolo, J. J. Cloning and Expression of CadD, a New Cadmium Resistance Gene of Staphylococcus Aureus. *Journal of Bacteriology* **1999**, *181* (13), 4071–4075.

(238) Arnesano, F.; Banci, L.; Bertini, I.; Mangani, S.; Thompsett, A. R. A Redox Switch in CopC: An Intriguing Copper Trafficking Protein That Binds Copper(I) and Copper(II) at Different Sites. *PNAS* **2003**, *100* (7), 3814–3819. https://doi.org/10.1073/pnas.0636904100.

(239) Broth Microdilution MIC Test. In *Clinical Microbiology Procedures Handbook, 3rd Edition*; Garcia, L. S., Ed.; American Society of Microbiology, 2010; pp 25–41. https://doi.org/10.1128/9781555817435.ch5.2.

(240) European Committee for Antimicrobial Susceptibility Testing (EUCAST) of the European Society of Clinical Microbiology and Infectious Diseases (ESCMID). Determination of Minimum Inhibitory Concentrations (MICs) of Antibacterial Agents by Broth Dilution. *Clinical Microbiology and Infection* **2003**, *9* (8), ix–xv. https://doi.org/10.1046/j.1469-0691.2003.00790.x.

(241) Arenas, F. A.; Pugin, B.; Henríquez, N. A.; Arenas-Salinas, M. A.; Díaz-Vásquez, W. A.; Pozo, M. F.; Muñoz, C. M.; Chasteen, T. G.; Pérez-Donoso, J. M.; Vásquez, C. C. Isolation, Identification and Characterization of Highly Tellurite-Resistant, Tellurite-Reducing Bacteria from Antarctica. *Polar Science* **2014**, *8* (1), 40–52. https://doi.org/10.1016/j.polar.2014.01.001.

(242) Ollivier, P. R. L.; Bahrou, A. S.; Marcus, S.; Cox, T.; Church, T. M.; Hanson, T. E. Volatilization and Precipitation of Tellurium by Aerobic, Tellurite-Resistant Marine Microbes. *Appl. Environ. Microbiol.* **2008**, *74* (23), 7163–7173. https://doi.org/10.1128/AEM.00733-08.

(243) Borghese, R.; Borsetti, F.; Foladori, P.; Ziglio, G.; Zannoni, D. Effects of the Metalloid Oxyanion Tellurite (TeO32−) on Growth Characteristics of the Phototrophic Bacterium Rhodobacter Capsulatus. *Appl. Environ. Microbiol.* **2004**, *70* (11), 6595–6602. https://doi.org/10.1128/AEM.70.11.6595-6602.2004.

(244) Moore, M. D.; Kaplan, S. Identification of Intrinsic High-Level Resistance to Rare-Earth Oxides and Oxyanions in Members of the Class Proteobacteria: Characterization of Tellurite, Selenite, and Rhodium Sesquioxide Reduction in Rhodobacter Sphaeroides. *Journal of Bacteriology* **1992**, *174* (5), 1505–1514. https://doi.org/10.1128/jb.174.5.1505-1514.1992.

(245) Rathgeber, C.; Yurkova, N.; Stackebrandt, E.; Beatty, J. T.; Yurkov, V. Isolation of Tellurite- and Selenite-Resistant Bacteria from Hydrothermal Vents of the Juan de Fuca Ridge in the Pacific Ocean. *Appl. Environ. Microbiol.* **2002**, *68* (9), 4613–4622. https://doi.org/10.1128/AEM.68.9.4613-4622.2002.

APPENDIX A: SUPPLEMENTAL TO CHAPTER 2

A1.1 Environmental bacterial isolation and metal screening

The collection of water and soil samples were collected from various locations within the Colorado Mining Belt. Water sources in the area have been contaminated with heavy metals since the advent of gold mining in Colorado in the 1851 gold rush. On a microbial level, the time scale of metal contamination provides a greater chance for finding bacteria that have evolved processes to handle high concentrations of metal. Water and soil samples were then diluted into PBS to collect bacteria and plated on various LB or minimal media agar plates of varying pH to provide different bacteria chances to grow. Plates were grown at room temperature (RT) and as colonies began to become visible, they were picked and grown up in corresponding liquid media. Once grown to density, freezer stocks were made and samples were diluted into media containing either Fe(II) (5 mM), Cu(II) (2 mM), AsO_3^{2-} (2 mM), SeO_3^{2-} (2 mM), TeO_3^{2-} (0.1 mM), Cd(II) (1 mM), or Zn(II) (2 mM) and allowed several days to grow. Bacterial samples were observed for both the ability to grow to density and if a color change was observed indicating a change in metal speciation. Of the ~200 bacterial colonies capable of growing in a lab setting, 16 isolated bacterial cultures showed growth and/or color change in all the metals tested. The sample LB_5-2_10^2_P1 (indicated by the arrow in **Figure A1.1**) was able to grow in liquid culture and agar plates supplemented with metals. Color changes were also observed when incubated with Fe(II), Cu(II), SeO_3^{2-}, and TeO_3^{2-}. LC-MS/MS was used to identify the species as *Rhodococcus erythropolis* PR4, a gram-positive nonmotile Actinomycete closely related to *Mycobacterium* and *Corynebacterium*.

R. erythropolis PR4 has been studied for its production of numerous siderophores and utilization of diesel oil and other hydrocarbons as carbon sources.[230–234] The genome of *R. erythopolis* PR4 has been sequenced along resulting in a circular genome of 6.5 Mb, two smaller circular plasmids of 104 kb and 3.6 kb, and a linear plasmid of 272 kb.[235] Encoded on the linear plasmid were genes that were homologous to metal resistance genes, namely a cation-efflux-family transporter known to increase resistance to cadmium, zinc, and cobalt, and a possible membrane-associated cadmium-binding protein, and a predicted cadmium-transporting P-type ATPase.[236,237] A protein belonging to the CopC/PcoC family involved in copper sequestration was also identified in this region although some amino acid residues were not conserved possibly preventing functionality.[238]

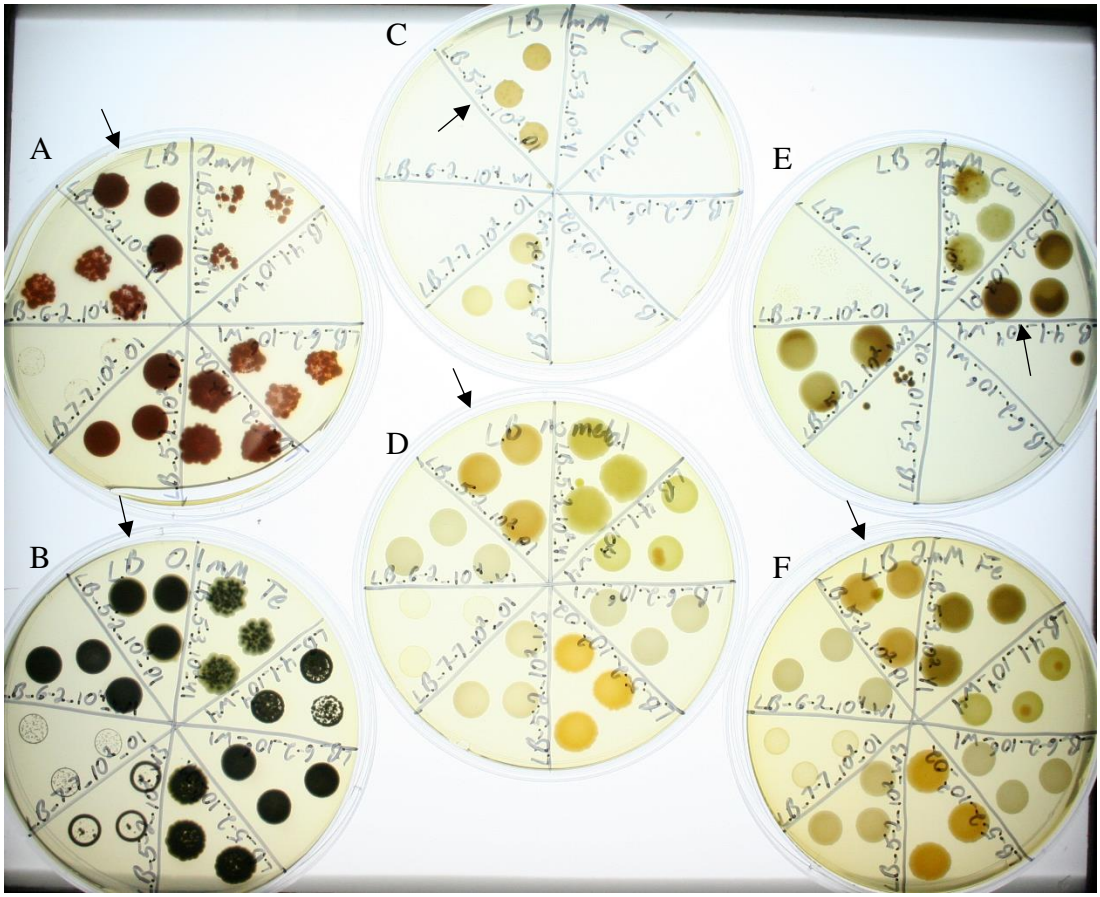

Figure A1.1. Various metal supplemented LB agar plates on which 8 different environmental isolates were plated. (**A**) 2 mM SeO_3^{2-}, (**B**) 0.1 mM TeO_3^{2-}, (**C**) 1 mM Cd(II), (**D**) no metal, (**E**) 2 mM Cu(II), (**F**) 2 mM Fe(II). The black arrows indicate the environmental isolate LB_5-2_10^2_P1.

A1.1.2 *MIC of Rhodococcus erythropolis PR4*

The minimal inhibitory concentration (MIC) for *R. erythropolis* PR4 was found using broth microdilution.[239,240] Resulting MICs for *R. erythropolis* PR4 are in **Table A.1**. The wide range of metal resistances of *R. erythropolis* PR4 was impressive, specifically the resistance identified against tellurium. There have been many species identified with Te-resistance with most falling between 1 – 2 mM MIC however bacteria isolated from hydrothermal vents in the Juan de Fuca Ridge were capable of growing in 10 mM concentrations.[241–245] Although not the highest resistance, growth up to 4.5 mM TeO_3^{2-} was an impressive outcome.

Table A1.1. MIC values for *R. erythropolis* PR4 determined by broth microdilution (mM)

Metal	TeO_3^{2-}	SeO_3^{2-}	Cd(II)	Cu(II)	Ni(II)	Co(II)	AsO_3^{2-}	Fe(II)	Zn(II)
Conc. (mM)	4.5	2.5	1.5	5.5	8	2.5	>10	5	5.5

In order to see if the color change observed in the cultures was due to formation of metal precipitate intra- or extracellularly, *R. erythropolis* PR4 was grown in LB supplemented with 2 mM of either SeO_3^{2-} or TeO_3^{2-}. After culture reached density, cells were collected and fixed for scanning electron microscopy (SEM) imaging. The resulting images showed a dramatic difference between cells incubated with SeO_3^{2-} and TeO_3^{2-} (**Figure A1.2**). When incubated with SeO_3^{2-} cells had large extrusions with high aspect ratios from the outer membranes composed of Se. When incubated with TeO_3^{2-} nanostructures were observed mostly at the distal ends of the cells. This variance between the two metals was unexpected and poses the question of what mechanisms are provoking such differences.

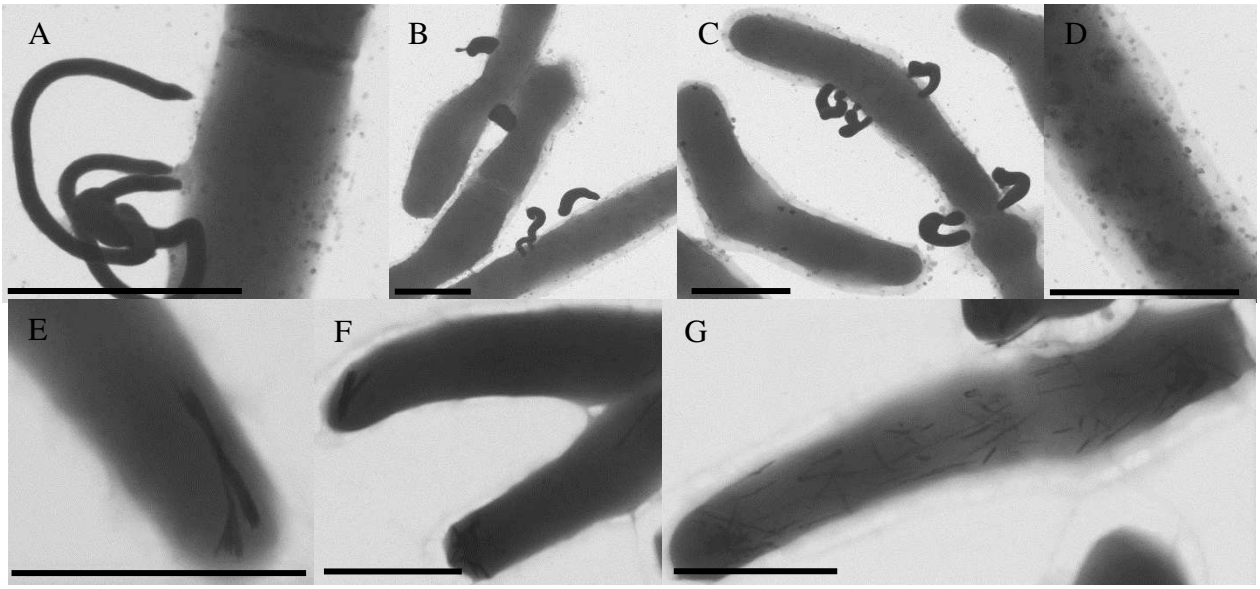

Figure A1.2. SEM images of *R. erythropolis* PR4. Panels (**A**) – (**D**) cells incubated in 2 mM SeO_3^{2-} with large nanostructures and/or nanoparticulate composed of Se on the cell surface. Panels (**E**) – (**G**) cells incubated with 2 mM TeO_3^{2-} with nanostructures present in the cytoplasm of the cell. Scale bar = 1 µm

A1.1.3 *Environmental Bacterial Isolation and Metal Screening*

Water ways around the Colorado Mineral Belt were visited and samples of water and soil were collected. For the soil samples, a small sample of soil was added to PBS and gently agitated. Supernatant was removed and applied to LB-agar or minimal media agar plates of various pH 3, 5, or 7. Samples were applied in dilutions of $10^0 – 10^6$. These various environs were expected to give some of the environmental isolates better chances to grow increasing the number of culturable microbes.

Plates were grown at Room Temperature for 2 weeks. After each week colonies were picked and grown in liquid media that corresponded to the plate the colony was picked from. Cultures were also grown at RT. Once grown to concentration a fraction of the cultures were stored in glycerol at -80°C until future studies.

Metal screening were initially performed in culture. First, liquid cultures of the targeted isolates were grown to until dense. A 1/100 fraction of the dense culture was then added to growth tubes that had media supplemented with the metals of interest, Fe(II) (5 mM), Cu(II) (2 mM), AsO_3^{2-} (2 mM), SeO_3^{2-} (2 mM), TeO_3^{2-} (0.1 mM), Cd(II) (1 mM), or Zn(II) (2 mM) and allowed to grow. Aspects of the incubated cultures were recorded; the density of the culture and if there was a color change of the colony indicating presence of metal reductive capabilities.

A1.1.4 *MIC Determination*

MIC for *R. erythropolis* PR4 was determined using a broth microdilution protocol.[239] First, a starter culture was begun of *R. erythropolis* in LB media with 5 µM K_2TeO_3 as a selecting agent and grown at RT with agitation. After 2 days, the culture was dense. Culture tubes were filled with 990 µL LB media and supplemented with 0.1 – 10 mM metal. 10 µL of the dense culture was then added to the culture tube. All inoculated tubes were then allowed to grow at RT for 3 days with gentle agitation to aerate the culture. After 3 days, the tube in which no growth was observed was considered the MIC.

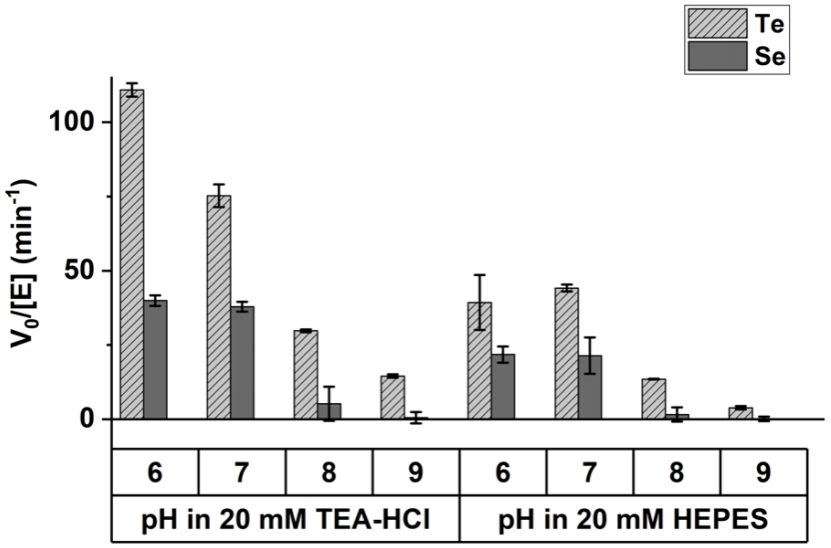

Figure A1.3. Buffer and pH screen indicating initial velocities for Mtr with substrates TeO_3^{2-} and SeO_3^{2-}. Substrates were at a starting concentration of 2 mM.

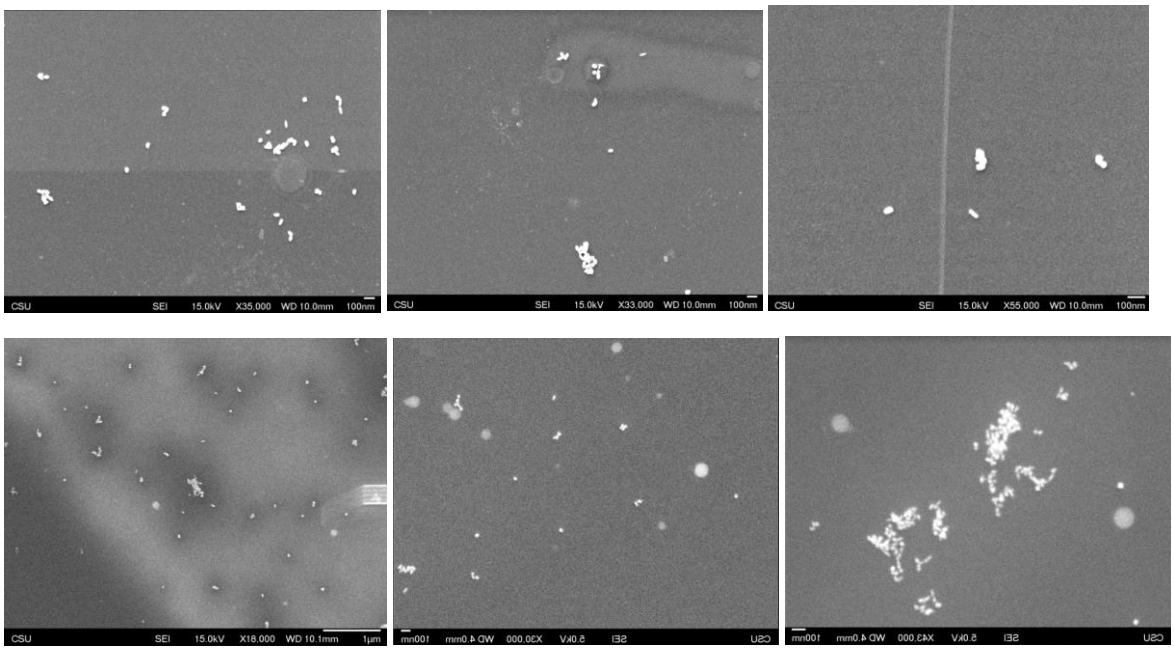

Figure A1.4A: Gallery of representative images of TeNPs synthesized by Mtr at [TeO_3^{2-}] of 1mM.

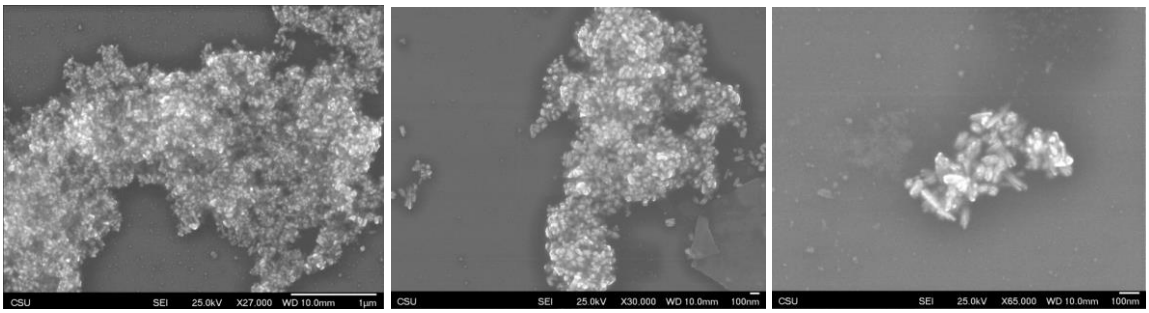

Figure A1.4C: Gallery of representative images of TeNPs synthesized by Mtr at [TeO_3^{2-}] of 7mM.

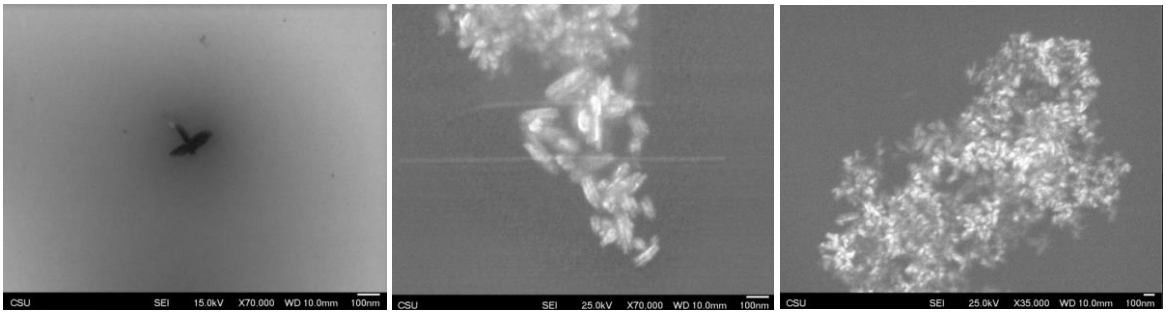

Figure A1.4B: Gallery of representative images of TeNPs synthesized by Mtr at [TeO_3^{2-}] of 3mM. Often the 'bundles of rods' appeared in larger aggregations (center and left panels).

APPENDIX B: SUPPLEMENTAL TO CHAPTER 3

A2.1 Materials and Methods

A2.1.1 *Molecular cloning*

Unless stated otherwise, all restriction enzymes used in molecular cloning were purchased through New England Biolabs, and DNA primers were purchased from Integrated DNA technologies (IDT, Inc.). Polymerase chain reaction (PCR) and digestion products were purified on 1% agarose (Thermo Fischer) gels run at 115 V for 40 min and imaged on a Bio-Rad Molecular Imager Gel Dox XR+ for further analysis and purification.

A2.1.2 *Error-prone PCR library*

An error-prone polymerase chain reaction (PCR) library of GRLMR was constructed using the GeneMorph™ II Random Mutagenesis Kit (Agilent) with parameters set for 3-5 mutations per 1000 bp using pET20b-GRLMR as a template and primers listed in the Supporting Information. After purification on a 1.0% agarose gel, the PCR product and pET20b plasmid were restriction digested using NdeI and XhoI (New England Biolabs) and subject to another round of purification following calf alkaline phosphatase (New England Biolabs) treatment of the plasmid. Digested PCR product and plasmid were combined at a 100 ng to 100 ng ratio and ligated overnight at 16 C using T4 Ligase (New England Biolabs). After heat inactivation at 65 C for 10 min, the ligation sample buffer was exchanged to Millipore water using a Monarch™ PCR and DNA Cleanup Kit (New England Biolabs) and electroporated to electrocompetent NEB-10Bs (New England Biolabs) using a Gene Pulser Xcell (Bio-Rad) according to factory settings. Serial dilution of the rescued cells yielded a total transformation number of ~100,000 library colony forming units (CFUs). The following day, library DNA was collected using a ZymoPURE™ Plasmid Maxiprep Kit (Zymo Research) and a sampling of 10 random colonies were sent for sequencing (Azenta Biosciences, LLC), which confirmed a mutational load in the desired range. Purified library plasmid was subsequently

transformed to chemically competent T7 Express lysY cells (New England Biolabs), yielding transformation efficiency 5x higher than the electroporated cells (500,000 library transformants). After rescue, cells were grown to an optical density at 600 nm (OD600) of 0.4 and aliquoted to 15% glycerol stocks for storage at –80 C.

The ePCR library of GRLMR was set up according to the specifications of the GeneMorph II Random Mutagenesis Kit with parameters set for approximately 5 mutations per gene. A random selection of 10 plated colonies were grown to confluency in 5 mL LB media, miniprepped, and DNA sent for sequencing (Azenta Biosciences).

A2.1.3 *Protein expression, purification, and characterization*

All protein expressions were conducted in T7 Express lysY cells with pET20b. Cells were grown from glycerol stocks overnight in 5 mL LB/carb cultures at 37 C and 250 RPM. 1 mL aliquots were dispensed into 1 L fresh LB/carb for a 1:000 inoculation. The cells were then grown to an OD600 of ~0.5 to 0.6 prior to addition of 50 uM IPTG and grown at RT at ~200 RPM. 50 uM selenite was added to expression vessels to supplement nutritional levels of selenium.

After expressing overnight, cells were centrifuged at 3,000 g then resuspended in 10 mL pH 6 100 mM MES lysate buffer containing 100 mM NaCl, 5% glycerol, and 0.5% triton x100 (Sigma Aldritch). Resuspended cells were sonicated at 70% in iterative cycles of 3 seconds on followed by 7 seconds off. Crude lysate was centrifuged at 10,000 g for 1 h, and the supernatant was filtered through a 0.2 um sterile filter.

Filtered lysate was combined at 1:1 volume with 10 mM imidazole/PBS buffer. A bed of 4 mL HisPur Nickel NTA resin (Thermo Fischer) was prepared by washing with 10 mM imidazole/PBS. The combined lysate/buffer solution was added to the prepared Ni-NTA resin and incubated at 4 C with stirring on an orbital shaker for 1 h. Crude lysate was discarded, and the column washed 4x with 40 mM imidazole/PBS, followed by an elution with 2 mL 300 mM imidazole. The buffer was exchanged to PBS

through use of centrifugal filters (10,000 MWCO – Amicon). Protein purity was assessed with SDS-PAGE at 150 V for 40-60 min followed by Coomassie staining. Protein concentration was determined through use of the Bradford assay (Thermo Fischer) using bovine serum albumin as a control.

A2.1.4 *Alanine mutations of GRLMR*

As a negative control, a soluble and expressible inactive GRLMR mutant was cloned. The two active site cysteines in GRLMR were exchanged to alanine residues with a Q5® Site Directed Mutagenesis Kit (New England Biolabs) using primers listed in the Appendix. Lack of activity of the purified enzyme was indicated by an absence of color change in the presence of NADPH and selenite.

A2.1.5 *Selenium reduction selection protocol*

An assay correlating enzyme-mediated selenium nanoparticle formation with cell survival in toxic quantities of sodium hydrogen selenite was developed in Luria Low Salt LB growth medium (Sigma Aldrich). Starter cultures of transformed T7 lysY cells containing ampicillin-resistant pET20b plasmids were grown overnight in 5 mL LB medium containing carbenicillin (LB/carb). The following morning, 100 uL of the overnight growths were inoculated to a fresh 2.5 mL low salt LB/carb and grown to an OD600 of 0.5 in an incubating shaker set to 250 RPM and 37 C. Subsequently, 100 uL of the resulting cultures were again inoculated to fresh low salt LB/carb containing 50 uM isopropyl β-D-1-thiogalactopyranoside (IPTG, Thermo Fischer) and sodium hydrogen selenite in varying amounts ranging from 30 mM to 60 mM. Cell quantities were determined over subsequent days through plating serial dilutions of 10 uL spots in triplicate on carbenicillin LB plates until notable culture growth or death was observed. In cases where cell growth was observed, 100 uL of the selection growth medium was inoculated to fresh LB/carb and grown to confluency for further DNA collection, sequencing, and in some cases additional rounds of selection.

A2.1.6 *Selenodiglutathione and tellurodiglutathione syntheses*

A reaction mixture was prepared with sequential addition of 394 uL Millipore water, 660 uL 0.1 M HCl, 110 uL 100 mM sodium hydrogen selenite or potassium tellurite (Alfa Aesar), and 440 uL 100 mM reduced glutathione (Sigma Aldrich) at room temperature. After 1 h the reaction mixture was loaded to a Alltima 3 um 150 x 4.6 mm C18 column equilibrated at 5% methanol in 0.05% acetic acid on an Cytiva UPC10 fast protein liquid chromatographer. Selenodiglutathione/tellurodiglutathione fractions were collected from 20-24 min as the 3rd of three total peaks absorbing in the UV range.

A2.1.7 *Enzyme kinetics*

Kinetics data was obtained via NADPH depletion (solution concentration 200 uM) using 50 ug enzyme in the presence of varying amount of substrate per reaction. Each reaction was run in a 1 mL plastic cuvette in a NanoDrop 2000 (Thermo Fischer) in triplicate. Data was fitted and plotted using Origin Software[124].

A2.1.8 *Enzymatic SeNP formation*

At 25^{o}C, four aliquots of enzymatic SeNPs were made using wild type GRLMR and turbo GRLMR. Two concentrations of Se were compared for each type of enzyme, yielding a 5 mM Se sample set and a 50 mM Se sample set. Additionally, a 0.934 M NADPH solution was made with PBS at a pH of 7.4.

To make 1 mL enzymatic solutions, the following was added. To make a 5 mM wild type solution, 5 µL 1 M $HNaSeO_3$ and 250 µL of a 3.87 mg/mL wild type stock were added to 650 µL PBS. To make a 50 mM wild type solution, 50 µL 1 M $HNaSeO_3$ and 250 µL of wild type stock were added to 600 µL PBS. To make a 5 mM turbo solution, 5 µL 1 M $HNaSeO_3$ and 100 µL of a 23.1 ng/mL turbo stock were added to 850 µL PBS. To make a 50 mM turbo solution, 50 µL 1 M $HNaSeO_3$ and 100 µL of turbo stock were added to 800 µL PBS. To all four solutions, 50 µL of the NADPH solution was introduced to start the reaction; all four tubes were allowed to react for three hours. Following reaction, the SeNP samples were all centrifuged at 7,000 rpm at 4^{o}C for 5 minutes for purification purposes; the supernatant was removed

and an orange nanoparticle pellet was retained. The nanoparticles were rinsed twice with 500 µL fresh PBS and centrifuged according to the same parameters as mentioned before. Final resuspension was achieved with 100 µL fresh PBS.

A2.1.9 *Performing DLS on enzymatic SeNPs for size distribution*

DLS was conducted for all four SeNP samples listed in the previous section. Using Zetasizer 7.12 for data collection and analysis of particle sizes, each measurement parameter was set up under the 'measurement' tab of the program. After naming the sample for each trial, the materials manager function allowed for the selection of Se nanoparticles in a PBS dispersant. Having set the material and dispersant, the machine was allowed to select an optimized equilibration temperature for sample equilibration over 2 minutes. The cell type set for these experiments was a disposable cuvette and the measurement angle was set to 173o backscatter. The DLS machine was set to automatic parameters for the optimization of number of runs and run duration. Automatic attenuation was also used, and the machine was set to three run sets per sample input. Finally, under the data processing setting, the default general purpose setting was utilized.

Each SeNP sample was loaded into a clean disposable cuvette and fresh PBS was used to bring each cuvette to the appropriate sample volume. Once filled appropriately, the cuvettes were capped and inserted into the machine. Using the parameters described above, each sample was run in a set of three measurements for a duration of 12-16 10 second runs. This data was then extrapolated and analyzed with Zetasizer 7.12.

A2.1.10 *TEM methods*

200 mesh copper TEM grids with carbon support film (Electron Microscopy Sciences) were glow discharged in a PELCO easiGlow (Ted Pella) to make them hydrophilic and to clean them. TEM samples were prepared by drop-casting 5 µL of enzymatically produced SeNP samples onto the 200 mesh copper TEM grids for 3-minutes before blotting the excess solution. Grids were washed twice with 5 µL filtered

ultrapure water for 1 minute each. After samples air-dried for 5 minutes, they were ready for imaging. Imaging was conducted in a JEOL 2100F Transmission Electron Microscope at 200 kV equipped with an Ultra-High Resolution (UHR) pole-piece and Gatan Ultrascan 2K x 2K CCD camera. Elemental analysis was conducted using an Oxford Instruments EDS detector operating while operating in STEM mode with a JEOL HAADF detector.

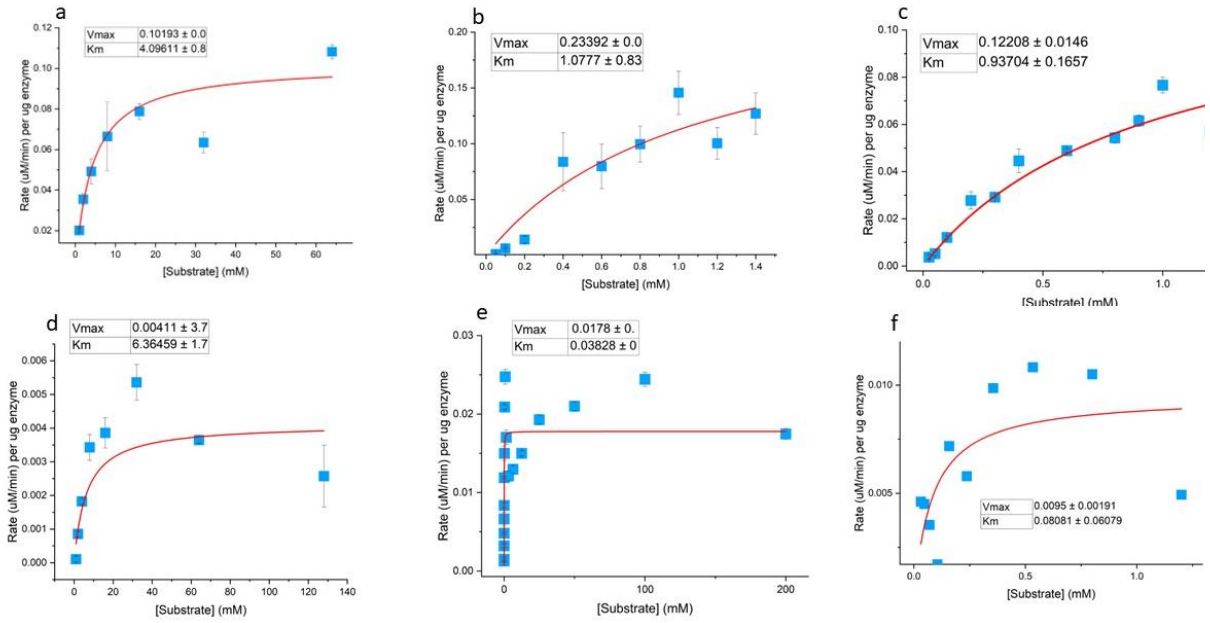

Figure A2.1: SeR nonlinear regression analysis of a) selenite, b) GSSG, c) GS-Se-SG, d) selenate, e) tellurite, f) GS-Te-SG. For panels d, e, and f, the substrate inhibition aspect of the enzyme mechanism causes a clear under-estimation of V_{max}.

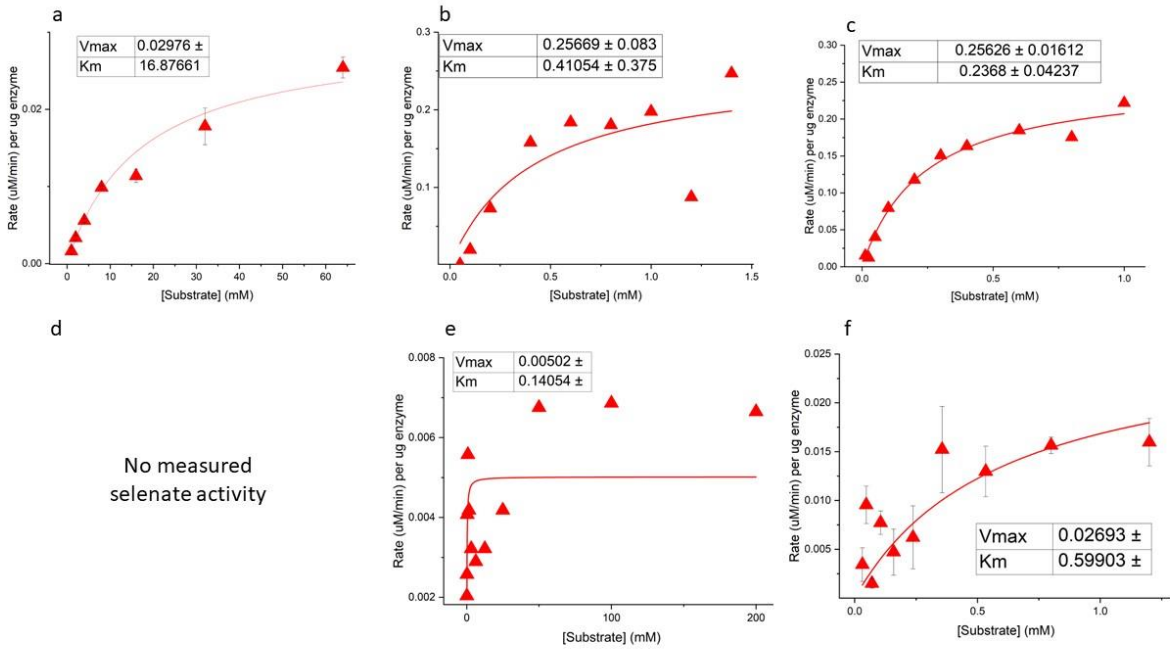

Figure A2.2: GRLMR nonlinear regression analysis of a) selenite, b) GSSG, c) GS-Se-SG, d) selenate, e) tellurite, f) GS-Te-SG. For panel e the substrate inhibition aspect of the enzyme mechanism causes a clear under-estimation of V_{max}.

A2.2 Protein modeling

A2.2.1 *Sequences utilized*

> WT-GRLMR
MAYDFDLYVIGAGSGGVRAARFAAGFGAKVAVAESRYLGGTCVNVGCVPKKLLVYGAHFAEDFEQASGFGWNLGEA
NFDWATLIANKDREINRLNGIYRNLLVNSGVTLHEAHAKIVGPHEVEVNGERFTAKNILIATGGWPQIPGIPGHEHAIGS
NEAFFLKELPKRVLVVGGGYIAVEFAGIFHGLGANTTLLYRGDLFLRGFDGSVRKHLQEELTKRGLDLQFNADIARIDKQA
DGSLKATLKDGRVLEADCVFYATGRRPMLDNLGLENIDVQLDDKGFIKVDGEYQTTEPSILALGDVIGRVQLTPVALAEG
MAVARRLFKPEQYRPVDYKMIPTAVFSLPNIGTVGLSEEEARECGHEVVIFESRFRPMKLTLTDCQEKTLMKLVVDART
DKVLGCHMVGPDAGEIVQGLAIALKAGATKRDFDDTIGVHPTAAEEFVTMRTPVSALEHHHHHH:MAYDFDLYVIGA
GSGGVRAARFAAGFGAKVAVAESRYLGGTCVNVGCVPKKLLVYGAHFAEDFEQASGFGWNLGEANFDWATLIANKD
REINRLNGIYRNLLVNSGVTLHEAHAKIVGPHEVEVNGERFTAKNILIATGGWPQIPGIPGHEHAIGSNEAFFLKELPKRV
LVVGGGYIAVEFAGIFHGLGANTTLLYRGDLFLRGFDGSVRKHLQEELTKRGLDLQFNADIARIDKQADGSLKATLKDGR
VLEADCVFYATGRRPMLDNLGLENIDVQLDDKGFIKVDGEYQTTEPSILALGDVIGRVQLTPVALAEGMAVARRLFKPE
QYRPVDYKMIPTAVFSLPNIGTVGLSEEEARECGHEVVIFESRFRPMKLTLTDCQEKTLMKLVVDARTDKVLGCHMVGP
DAGEIVQGLAIALKAGATKRDFDDTIGVHPTAAEEFVTMRTPVSALEHHHHHH

> SeR
MAYDFDLYVIGAGSGGVRAARFAAGFGAKVAVAESRYLGGTCVNVGCVPKKLLVYGAHFAEDFEQASGFGWNLGEA
NFDWATLIANKDREINRLNGIYRNLLVNSGVTLHEAHAKIVGPHEVEVNGERFTAKNILIATGGWPQIPGIPGHEHAIGS

NEAFFLKELPKRVLVVGGGYIAVEFAGIFHGLGANTTLLYRGDLFLRGFDGSVRKHLQEELTKRGLDLQFNADIARIDKQA
DGSLKATLKDGRVLEADCVFYATGRRPMLDNLGLENIDVQLDDKGFIKVDGEYQTTEPSILALGDVIGRVQLTPVAHAE
GMAVARRLFKPEQYRPVDYKMIPTAVFSLPNIGTVGLSEEEARECGHEVVIFESRFRPMKLTLTDCQEKTLMKLVVDAR
TDKVLGCHMVGPEAGEIVQGLAIALKAGATKRDFDDTIGVHPTAAEEFVTMRTPVSALEHHHHHH:MAYDFDLYVIGA
GSGGVRAARFAAGFGAKVAVAESRYLGGTCVNVGCVPKKLLVYGAHFAEDFEQASGFGWNLGEANFDWATLIANKD
REINRLNGIYRNLLVNSGVTLHEAHAKIVGPHEVEVNGERFTAKNILIATGGWPQIPGIPGHEHAIGSNEAFFLKELPKRV
LVVGGGYIAVEFAGIFHGLGANTTLLYRGDLFLRGFDGSVRKHLQEELTKRGLDLQFNADIARIDKQADGSLKATLKDGR
VLEADCVFYATGRRPMLDNLGLENIDVQLDDKGFIKVDGEYQTTEPSILALGDVIGRVQLTPVAHAEGMAVARRLFKPE
QYRPVDYKMIPTAVFSLPNIGTVGLSEEEARECGHEVVIFESRFRPMKLTLTDCQEKTLMKLVVDARTDKVLGCHMVGP
EAGEIVQGLAIALKAGATKRDFDDTIGVHPTAAEEFVTMRTPVSALEHHHHHH

> mycothione reductase from *rhodococcus erythropolis* (strain PR4/ NBRC 100887)
MTHYDLAIIGSGSGNSLPDERFDGKKIAILEEGTFGGTCLNVGCIPTKMFVYAAEVARTITTAEKYGVDATLDGVRWSDI
VKRVFGRIDPISAGGERYRSEDSPNTTVYRGHATFTGDKTIDTGTGETITADQVVIAAGSRPIIPEEIASSGVKYYTNEDIM
RLPELPEHLVIVGSGFIATEFAHVFSALGSRVSIIGRSQRLLRHLDDEISERFTELAEQKWDVHLGSPLTSVRGDGDNIAVE
LANGTVVSGDVLLVAVGRQPNGDLLGLDKAGVELDDKGSVVVDEYQRTTAEGVFALGDVSSPYQLKHVANHEARVVQ
HNLLQDAWKDTSGLRSTDHRFVPAAVFTDPQIADVGMTEKQARDAGLDITVKVQAYGDVAYGWAMEDQEGICKVIA
ERGTGRILGAHVMGTQAPTVIQPLIQAMSFGLSAQDMARGQYWIHPALAEVVENALLGLDI

> mercuric reductase, merA, from *streptomyces lividans*
MLQAHTGYDLAIIGSGAGAFAAAIAARNKGRSVVMVERGTTGGTCVNVGCVPSKALLAAAEARHGAQAASRFPGIQA
TEPALDFPALISGKDTLVGQLRAEKYTDLAAEYGWQIVHGTATFADGPMLEVALNDGGTATVEAAHYLIATGSAPTAPH
IDGLDQVDYLTSTTAMELQQLPEHLLILGGGYVGLEQAQLFARLGSRVTLAVRSRLASREEPEISAGIENIFREEGITVHTR
TQLRAVRRDGEGILATLTGPDGDQQVRASHLLIATGRRSVTNGLGLERVGVKTGERGEVVVDEYLRTDNPRIWAAGDV
TCHPDFVYVAAAHGTLVADNALDGAERTLDYTALPKVTFTSPAIASVGLTEAQLTEAGIAHQTRTLSLENVPRALVNRDT
RGLVKLIAERGTGKLLAAHVLAEGAGDVITAATYAITAGLTVDQLARTWHPYLTMAEALKLAAQTFTSDVAKLSCCAG

A2.2.2 *Clustal Omega Sequence Alignment*

```
WT_GRLMR                ----------------------MAYDFDLYVIGAGSGGVRAARFAAGFGAKVAVAESRYL
        38
3O0H,                   MAHHHHHHMGTLEAQTQGPGSMGSFDFDLFVIGSGSGGVRAARLAGALGKRVAIAEEYRI
        60
4DNA,                   ----------------------XSAFDYDLFVIGGGSGGVRSGRLAAALGKKVAIAEEFRY
        39
1ONF,                   ------------------------MVYDLIVIGGGSGGMAAARRAARHNAKVALVEKSRL
        36
2HQM,                   ---------------YVEFMSTNTKHYDYLVIGGGSGGVASARRAASYGAKTLLVEAKAL
        45
GR_homo                 ------ACRQEPQPQGPPPAAGAVASYDYLVIGGGSGGLASARRAAELGARAAVVESHKL
        54
6B4O,                   --------------------SNAMKTYDYIVIGGGSGGIASANRAGMHGANVLLIEGNEI
        40
6DU7,                   ------------------------MREYDIIAIGGGSGGIATMNRAGEHGAQAAVIEEKKL
        37
5V36,                   --------------------SNAMTKQYDYIVIGGGSGGIASANRAAMHGAKVILFEGKQV
        41
6N7F,                   --------------------SNAMVIPYDYIVIGGGSAGIASANRAAMHGAKVLLAEGKEI
        41
5U1O,                   ---------------SNAMEKVMATHFDYICIGGGSGGIASANRAAMYGAKVALIEAQDL
        45
5VDN,                   ---------SNAMTGYLMETTLMTKHYDYLAIGGGSGGIASINRAAMYGKKCALIEAKQL
        51
```

```
1GER,                   ----------------------MTKHYDYIAIGGGSGGIASINRAAMYGQKCALIEAKEL
        38
1GES,                   ----------------------MTKHYDYIAIGGGSGGIASINRAAMYGQKCALIEAKEL
        38
mercuric_reductase,     -------------------MLQAHTGYDLAIIGSGAGAFAAAIAARNKGRSVVMVERGTT
        41
mycothione_reductase    ----------------------MTHYDLAIIGSGSGNSLP--DERFDGKKIAILEEGTF
        35
                                             :*   **.*:.           .    : *

WT_GRLMR                GGTCVNVGCVPKKLLVYGAHFAEDFE-QASGFG------WNLGEANFDWATLIANKDREI
        91
3O0H,                   GGTCVIRGCVPKKLYFYASQYAQEFS-KSIGFG------WKYADPIFNWEKLVAAKNKEI
        113
4DNA,                   GGTCVIRGCVPKKLYVYASQFAEHFE-DAAGFG------WTVGESRFDWAKLVAAKEQEI
        92
1ONF,                   GGTCVNVGCVPKKIMFNAASVHDILE-NSRHYG------FDT-KFSFNLPLLVERRDKYI
        88
2HQM,                   GGTCVNVGCVPKKVMWYASDLATRVS-HANEYGLYQNLPLDKEHLTFNWPEFKQKRDAYV
        104
GR_homo                 GGTCVNVGCVPKKVMWNTAVHSEFMH-DHADYG------FPSCEGKFNWRVIKEKRDAYV
        107
6B4O,                   GGTCVNVGCVPKKVMWQASSMMEMMERDTAGYG------FDVEIKNFSFKQLVENREKYI
        94
6DU7,                   GGTCVNVGCVPKKIMWYGAQIAETFHQFGEDYG------FKTTDLNFDFATLRRNRESYI
        91
5V36,                   GGTCVNVGCVPKKVMWYGAQVAETINNYAADYG------FDVTTQAFHFDVLKQNRQAYI
        95
6N7F,                   GGTCVNLGCVPKKVMWYGAQVADILGTYAKDYG------FDFKEKAFDFKQLKANRQAYI
        95
5U1O,                   GGTCVNVGCVPKKVMWHGAQIAEAMNLYAEDYG------FDVDVKGFDWSKLVESRQAYI
        99
5VDN,                   GGTCVNVGCVPKKVMWHAAQIAEAIHLYGPDYG------FDTTVNHFDWKKLIANRTAYI
        105
1GER,                   GGTCVNVGCVPKKVMWHAAQIREAIHMYGPDYG------FDTTINKFNWETLIASRTAYI
        92
1GES,                   GGTCVNVGCVPKKVMWHAAQIREAIHMYGPDYG------FDTTINKFNWETLIASRTAYI
        92
mercuric_reductase,     GGTCVNVGCVPSKALLAAAEARHGAQAASRFPG------IQATEPALDFPALISGKDTLV
        95
mycothione_reductase    GGTCLNVGCIPTKMFVYAAEVARTITTAEKY-G------VDATLDGVRWSDIVKRVFGRI
        88
                        ****:  **:*.*     :             *            .    :      :

WT_GRLMR                NRLN---GIYRNLLVNSGVTLHEAHAKIVGPHEVE--------------VNGERFTAKNI
        134
3O0H,                   SRLE---GLYREGLQNSNVHIYESRAVFVDEHTLEL------------SVTGERISAEKI
        158
4DNA,                   ARLE---GLYRKGLANAGAEILDTRAELAGPNTVKL------------LASGKTVTAERI
        137
1ONF,                   QRLN---NIYRQNLSKDKVDLYEGTASFLSENRILIKGTKDNNNKDNGPLNEEILEGRNI
        145
2HQM,                   HRLN---GIYQKNLEKEKVDVVFGWARFNKDGNVEVQ---------KRDNTTEVYSANHI
        152
GR_homo                 SRLN---AIYQNNLTKSHIEIIRGHAAFTSDPKPTI------------EVSGKKYTAPHI
        152
6B4O,                   DFLH---GAYNRGLDSNNIERIHGYATFTGE--QTI------------EVNGTEYTAPHI
        137
6DU7,                   DRAR---SSYDGSFKRNGVDLIEGHAEFVDS--HTV------------SVNGELIRAKHI
        134
5V36,                   DRIH---DSYERGFDSNGVERVYGYATFVDA--HTV------------EVAGEHYTAPHI
        138
```

```
6N7F,                   DRIH---ASYERGFEQNGVDRIYDYAVFKDA--HTV------------EIAGQLYTAPHI
        138
5U1O,                   GRIH---QSYDRVLGNNKVNVIKGFAKFVDE--KTV------------EVNGEHYTADHI
        142
5VDN,                   DRIH---QSYERGLGNNKVDVIQGFARFVDA--HTV------------EVNGETITADHI
        148
1GER,                   DRIH---TSYENVLGKNNVDVIKGFARFVDA--KTL------------EVNGETITADHI
        135
1GES,                   DRIH---TSYENVLGKNNVDVIKGFARFVDA--KTL------------EVNGETITADHI
        135
mercuric_reductase,     GQL--RAEKYTDLAAEYGWQIVHGTATFADGPMLEVA---------LNDGGTATVEAAHY
        144
mycothione_reductase    DPISAGGERYRSED-SPNTTVYRGHATFTGDK----T---------IDTGTGETITADQV
        134
                                *              * :                          . .

WT_GRLMR                LIATGGWPQI---PGIPGHEHAIGSNEAFFLKELPKRVLVVGGGYIAVEFAGIFHGLGAN
        191
3O0H,                   LIATGAKIVSN--SAIKGSDLCLTSNEIFDLEKLPKSIVIVGGGYIGVEFANIFHGLGVK
        216
4DNA,                   VIAVGGHPSPH--DALPGHELCITSNEAFDLPALPESILIAGGGYIAVEFANIFHGLGVK
        195
1ONF,                   LIAVGNKPVFP---PVKGIENTISSDEFFNIKES-KKIGIVGSGYIAVELINVIKRLGID
        201
2HQM,                   LVATGGKAIFP--ENIPGFELGTDSDGFFRLEEQPKKVVVVGAGYIGIELAGVFHGLGSE
        210
GR_homo                 LIATGGMPSTPHESQIPGASLGITSDGFFQLEELPGRSVIVGAGYIAVEMAGILSALGSK
        212
6B4O,                   LIATGGRPKKL---GIPGEEYALDSNGFFALEEMPKRVVFVGAGYIAAELAGTLHGLGAE
        194
6DU7,                   VIATGAHPSIP---NIPGAELGGSSDDVFAWEELPESVAILGAGYIAVELAGVLHTFGVK
        191
5V36,                   LIATGGHALLP---DIPGSEYGITSDGFFELDAIPKRTAVVGAGYIAVEISGILHALGSE
        195
6N7F,                   LIATGGHPVFP---DIEGAQYGISSDGFFALDEVPKRTAVVGAGYIAVELAGVLHALGSK
        195
5U1O,                   LIAVGGRPTIP---NIPGAEYGIDSNGFFDLAEQPKRVAVVGAGYIAVEIAGVLHALGTE
        199
5VDN,                   LIATGGRPSHP---DIPGAEYGIDSDGFFELDEMPKRVAVVGAGYIAVEIAGVLNGLGTE
        205
1GER,                   LIATGGRPSHP---DIPGVEYGIDSDGFFALPALPERVAVVGAGYIAVELAGVINGLGAK
        192
1GES,                   LIATGGRPSHP---DIPGVEYGIDSDGFFALPALPERVAVVGAGYIGVELGGVINGLGAK
        192
mercuric_reductase,     LIATGSAPTAPHIDGLDQVDYL-TSTTAMELQQLPEHLLILGGGYVGLEQAQLFARLGSR
        203
mycothione_reductase    VIAAGSRPIIPEEIASSGVKYY-TNEDIMRLPELPEHLVIVGSGFIATEFAHVFSALGSR
        193
                        ::*.*             .    .   :          . *.*::. *    :  :*

WT_GRLMR                TTLLYRGDLFLRGFDGSVRKHLQEELTKRGLDLQFNADIARIDKQADGSL-KATLK----
        246
3O0H,                   TTLLHRGDLILRNFDYDLRQLLNDAMVAKGISIIYEATVSQVQSTENCYN-VV-LT----
        270
4DNA,                   TTLIYRGKEILSRFDQDXRRGLHAAXEEKGIRILCEDIIQSVSADADGRR-VATTX----
        250
1ONF,                   SYIFARGNRILRKFDESVINVLENDMKKNNININVTFADVVEIKKVSDKNL-SIHLS----
        256
2HQM,                   THLVIRGETVLRKFDECIQNTITDHYVKEGINVHKLSKIVKVEKNVETDKLKIHMN----
        266
GR_homo                 TSLMIRHDKVLRSFDSMISTNCTEELENAGVEVLKFSQVKEVKKTLSGLE-VSMVTAVPG
        271
```

```
6B4O,                   THWAFRHERPLRSFDDMLSEKVVERYQEMGMQIHPNATPAKIEKTAQNEY-VITFE----
        249
6DU7,                   TDLFVRRDRPLRGFDSYIVEGLVKEMERTNLPLHTHKVPVKLEKTTDG-I-TIHFE----
        245
5V36,                   THLFVRRDRPLRKFDKEIVGTLVDEMKKDGPHLHTFSVPKEVIKNTDNSL-TLILE----
        250
6N7F,                   TDLFIRHDRPLRSFDKTIVDVLVDEMAVNGPRLHTHAEVAKVVKNTDESL-TLYLK----
        250
5U1O,                   THLFVRKESPLRSFDPMIIDTLVEVMEAEGPTLHTHSVPKEVVKEADGSL-TLHLE----
        254
5VDN,                   THLFVRKHAPLRTFDPLIVETLLEVMNTEGPKLHTESVPKAVIKNADGSL-TLQLE----
        260
1GER,                   THLFVRKHAPLRSFDPMISETLVEVMNAEGPQLHTNAIPKAVVKNTDGSL-TLELE----
        247
1GES,                   THLFEMFDAPLPSFDPMISETLVEVMNAEGPQLHTNAIPKAVVKNTDGSL-TLELE----
        247
mercuric_reductase,     VTLAVRSRLASRE-EPEISAGIENIFREEGITVHTRTQLRAVRRDGEGILATLT------
        256
mycothione_reductase    VSIIGRSQRLLRHLDDEISERFT-ELAEQKWDVHLGSPLTSVRGDGDNIAVELA------
        246
                                    :                :       :    .

WT_GRLMR                ----DGRVLEADCVFYATGRRPMLDNLGLENIDVQLDDKGFIKVDGEYQTTEPSILALGD
        302
3O0H,                   ----NGQTICADRVMLATGRVPNTTGLGLERAGVKVNEFGAVVVDEKMTTNVSHIWAVGD
        326
4DNA,                   ----KHGEIVADQVXLALGRXPNTNGLGLEAAGVRTNELGAIIVDAFSRTSTPGIYALGD
        306
1ONF,                   ---DGRIYEHFDHVIYCVGRSPDTENLKLEKLNVETN-NNYIVVDENQRTSVNNIYAVGD
        312
2HQM,                   ---DSKSIDDVDELIWTIGRKSHL-GMGSENVGIKLNSHDQIIADEYQNTNVPNIYSLGD
        322
GR_homo                 RLPVMTMIPDVDCLLWAIGRVPNTKDLSLNKLGIQTDDKGHIIVDEFQNTNVKGIYAVGD
        331
6B4O,                   ----NGESITTDAVIFGTGRQPNTDQLGLENTKVALDEKGYVKVDKFQNTTQNGIYAVGD
        305
6DU7,                   ----DGTSHTASQVIWATGRRPNVKGLQLEKAGVTLNERGFIQVDEYQNTVVEGIYALGD
        301
5V36,                   ----NGEEYTVDTLIWAIGRAANTKGFNLEVTGVTLDSRGFIATDAFENTNVEGLYALGD
        306
6N7F,                   ----DGQEVEVDQLIWAIGRKPNLEGFSLDKTGVTLNDKGYIETDAYENTSVKGIYAVGD
        306
5U1O,                   ----NGESQNVDQLIWAIGRHPATDAINLASTGVATNEKGYIKVDEYQETNVKGIYCVGD
        310
5VDN,                   ----NGTEVTVDHLIWAIGREPATDNLNLSVTGVKTNDKGYIEVDKFQNTNVKGIYAVGD
        316
1GER,                   ----DGRSETVDCLIWAIGREPANDNINLEAAGVKTNEKGYIVVDKYQNTNIEGIYAVGD
        303
1GES,                   ----DGRSETVDCLIWAIGREPANDNINLEAAGVKTNEKGYIVVDKYQNTNIEGIYAVGD
        303
mercuric_reductase,     -GPDGDQQVRASHLLIATGRRSVTNGLGLERVGVKTGERGEVVVDEYLRTDNPRIWAAGD
        315
mycothione_reductase    -N---GTVVSGDVLLVAVGRQPNGDLLGLDKAGVELDDKGSVVVDEYQRTTAEGVFALGD
        302
                              . :    **      :      :  .  . : .*    *    : . **

WT_GRLMR                V-I---------------------------------GRVQLTPVALAEGMAVARRLFKPE
        328
3O0H,                   V-T---------------------------------GHIQLTPVAIHDAMCFVKNAFENT
        352
4DNA,                   V-T---------------------------------DRVQLTPVAIHEAXCFIETEYKNN
        332
```

```
1ONF,                   CCMVKKSKEIEDLNLLKLYNEERYLNKKENVTEDIFYNVQLTPVAINAGRLLADRLFLKK
        372
2HQM,                   V-V---------------------------------GKVELTPVAIAAGRKLSNRLFGPE
        348
GR_homo                 V-C---------------------------------GKALLTPVAIAAGRKLAHRLFEYK
        357
6B4O,                   V-I---------------------------------GKIDLTPVAIAAGRRLSERLFNGQ
        331
6DU7,                   V-T---------------------------------GEKELTPVAIKAGRTLSERLFNGK
        327
5V36,                   V-N---------------------------------GKLELTPVAVKAGRQLSERLFNHK
        332
6N7F,                   V-N---------------------------------GKLALTPVAVAAGRRLSERLFNGK
        332
5U1O,                   IME---------------------------------GGIELTPVAVKAGRQLSERLFNNK
        337
5VDN,                   N-T---------------------------------GVVELTPVAVAAGRRLSERLFNNK
        342
1GER,                   N-T---------------------------------GAVELTPVAVAAGRRLSERLFNNK
        329
1GES,                   N-T---------------------------------GAVELTPVAVAAGRRLSERLFNNK
        329
mercuric_reductase,     V-T---------------------------------CHPDFVYVAAAHGTLVADNALDG-
        340
mycothione_reductase    V-S---------------------------------SPYQLKHVANHEARVVQHNLLQDA
        328
                                                            :  **   .  .

WT_GRLMR                -----QYRPVDYKMIPTAVFSLPNIGTVGLSEEEARECGH--EVVIFESRFRPMKLTLT-
        380
3O0H,                   -----ST-TPDYDLITTAVFSQPEIGTVGLSEEDALHRYK--RVEIYRTVFRPMRNVLS-
        403
4DNA,                   -----PT-SPDHDLIATAVFSQPEIGTVGITEEEAARKFQ--EIEVYRAEFRPXKATLS-
        383
1ONF,                   ------TRKTNYKLIPTVIFSHPPIGTIGLSEEAAIQIYGKENVKIYESKFTNLFFSVYD
        426
2HQM,                   K---FRNDKLDYENVPSVIFSHPEAGSIGISEKEAIEKYGKENIKVYNSKFTAMYYAML-
        404
GR_homo                 -----EDSKLDYNNIPTVVFSHPPIGTVGLTEDEAIHKYGIENVKTYSTSFTPMYHAVT-
        411
6B4O,                   -----TDLYLDYNLVPTVVFTHPPVATIGLTEKAALEEYGEDQVKIYRSSFTPMYFALG-
        385
6DU7,                   -----TTAKMDYSTIPTVVFSHPAIGTVGLTEEQAIKEYGQDQIKVYKSSFASMYSACT-
        381
5V36,                   -----PQAKMDYKDVATVIFSHPVIGSIGLSEEAALDQYGEENVTVYRSTFTSMYTAVT-
        386
6N7F,                   -----TDEKLDYQNVATVIFSHPVIGSVGLSEEAAVKQYGQEAVKTYQSRFTSMFTAIT-
        386
5U1O,                   -----PNAKMDYDLVPTVVFSHPPIGTIGLTTQEAEEKYGKDNIKVYTSGFTAMYTAVT-
        391
5VDN,                   -----PDEHLDYSNIPTVVFSHPPIGTIGLTEPQAREKFGDDQVKVYTSSFTAMYSAVT-
        396
1GER,                   -----PDEHLDYSNIPTVVFSHPPIGTVGLTEPQAREQYGDDQVKVYKSSFTAMYTAVT-
        383
1GES,                   -----PDEHLDYSNIPTVVFSHPPIGTVGLTEPQAREQYGDDQVKVYKSSFTAMYTAVT-
        383
mercuric_reductase,     -----AERTLDYTALPKVTFTSPAIASVGLTEAQLTEAGIAHQTRTLS--LENVPRALV-
        392
mycothione_reductase    WKDTSGLRSTDHRFVPAAVFTDPQIADVGMTEKQARDAGLDITVKVQA--YGDVAYGWA-
        385
                                  ::  :  . *: *  . :*::
```

```
WT_GRLMR                ---DCQEKTLMKLVVDARTDKVLGCHMVGPDAGEIVQGLAIALKAGATKRDFDDTI-GVH
        436
3O0H,                   ---GSPEKMFMKLVVDGESRIVVGAHVLGENAGEIAQLIGISLKGKLTKDIFDKTM-AVH
        459
4DNA,                   ---GRKEKTIXKLVVNAADRKVVGAHILGHDAGEXAQLLGISLRAGCTKDDFDRTX-AVH
        439
1ONF,                   IEPELKEKTYLKLVCVGKDELIKGLHIIGLNADEIVQGFAVALKMNATKKDFDETI-PIH
        485
2HQM,                   ---SEKSPTRYKIVCAGPNEKVVGLHIVGDSSAEILQGFGVAIKMGATKADFDNCV-AIH
        460
GR_homo                 ---KRKTKCVMKMVCANKEEKVVGIHMQGLGCDEMLQGFAVAVKMGATKADFDNTV-AIH
        467
6B4O,                   ---EYRQKCDMKLICVGKEEKIVGLHGIGIGVDEMLQGFAVAIKMGATKADFDNTV-AIH
        441
6DU7,                   ---RNRQESRFKLITAGSEEKVVGLHGIGYGVDEMIQGFAVAIKMGATKADFDATV-AIH
        437
5V36,                   ---SHRQACKMKLVTVGEDEKIVGLHGIGYGVDEMIQGFAVAIKMGATKADFDNTV-AIH
        442
6N7F,                   ---NHRQPCLMKLVTVGDTEKIVGLHGIGYGVDEMIQGFAVAIKMGATKADFDNTV-AIH
        442
5U1O,                   ---KHRQPCKMKLVCAGEEETVVGLHGIGFTVDEMIQGFGVAMKMGATKADFDSVV-AIH
        447
5VDN,                   ---QHRQPCRMKLVCVGAEEKIVGIHGIGFGMDEILQGFAVAMKMGATKKDFDNTV-AIH
        452
1GER,                   ---THRQPCRMKLVCVGSEEKIVGIHGIGFGMDEMLQGFAVALKMGATKKDFDNTV-AIH
        439
1GES,                   ---THRQPCRMKLVCVGSEEKIVGIHGIGFGMDEMLQGFAVALKMGATKKDFDNTV-AIH
        439
mercuric_reductase,     ---NRDTRGLVKLIAERGTGKLLAAHVLAEGAGDVITAATYAITAGLTVDQLART--W-H
        446
mycothione_reductase    ---MEDQEGICKVIAERGTGRILGAHVMGTQAPTVIQPLIQAMSFGLSAQDMARGQYWIH
        442
                                  *::       : . *  .           ::    :   :       *

WT_GRLMR                PTAAEE-FVTMRTPVSAGS----------    454
3O0H,                   PTMSEE-LVTMYKPSYVYENGEKLDN---    484
4DNA,                   PTAAEE-LVTXYQPSYRVRNGERVG----    463
1ONF,                   PTAAEE-FLTLQPWMK-------------    500
2HQM,                   PTSAEE-LVTMRGSHHHHHH---------    479
GR_homo                 PTSSEE-LVTLR-----------------    478
6B4O,                   PTGSEE-FVTMR-----------------    452
6DU7,                   PTSSEE-FVTMR-----------------    448
5V36,                   PTGSEE-FVTMR-----------------    453
6N7F,                   PTGSEE-FVTMR-----------------    453
5U1O,                   PTGSEE-FVTMR-----------------    458
5VDN,                   PTAAEE-FVTMR-----------------    463
1GER,                   PTAAEE-FVTMR-----------------    450
1GES,                   PTAAEE-FVTMR-----------------    450
mercuric_reductase,     PYLTMAEALKLAAQ-TFTSDVAKLSCCAG    474
mycothione_reductase    PALA--EVVENA---LLGLDI--------    458
                        *  :    :
```

A2.2.3 *AlphaFold modeling*

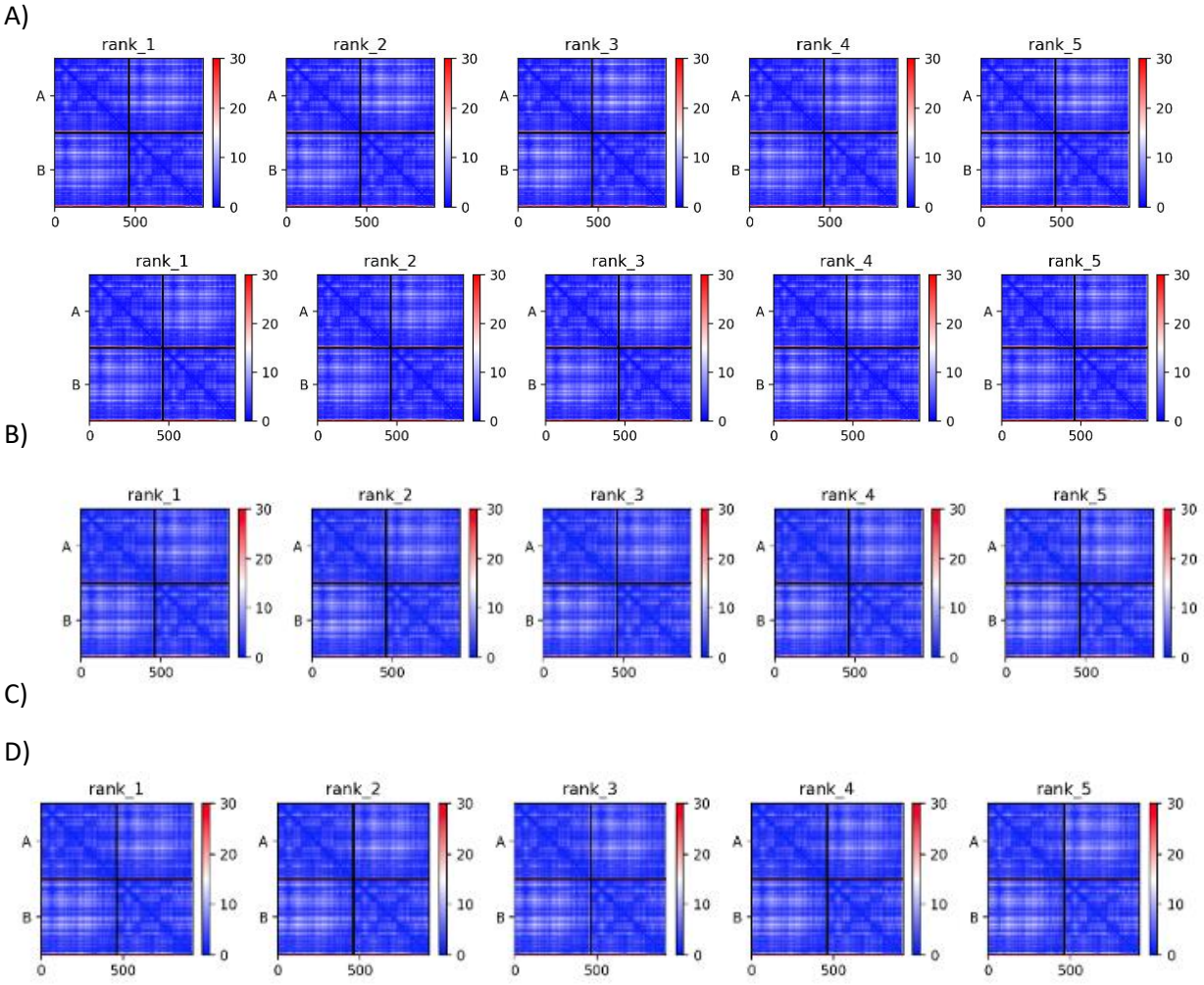

Figure A2.3. The PAE scores are plotted for each of the five alphafold2 ranked models generated for (A) GRLMR with templates, (B) SeR with templates, (C) GRLMR without templates, (D) SeR without templates. Each axis corresponds to individual amino acid positions and "A" and "B" indicate the chain ID. These plots are separated into four quadrants. The top left quadrant corresponds to residue distance errors between residues within chain A, top right to chain A residues and chain B residues, bottom left in chain B residues to chain A and lower right one represents errors within residues in chain B. The error is displayed on a color spectrum going from blue (0 angstroms) to white (15 angstroms) to red (30 angstroms). A) the wildtype metrics and B) the SeR metrics. There are low PAE scores overall with the highest error consistently being at the C-termini of both chains with respect to all of the rest of the residues (two horizontal red lines at the bottom of all four quadrants). There are also some white shaded regions in the two quadrants which would relate chains A and B relative errors but within a single chain the PAE are very low (almost a block of blue shading).

Table A2.1: pLDDT scores for each of 5 models generated for GRLMR and SeR with templates.

GRLMR	Average alpha-Carbon pLDDT	Average PAE (angstroms)
Rank 1 model 5	96.54	4.61
Rank 2 model 3	96.17	4.76
Rank 3 model 1	96.36	4.74
Rank 4 model 4	96.40	4.78
Rank 5 model 2	96.29	4.85
SeR	Average alpha-Carbon pLDDT	Average PAE (angstroms)
Rank 1 model 3	96.22	4.72
Rank 2 model 5	96.48	4.62
Rank 3 model 4	96.43	4.71
Rank 4 model 1	96.38	4.75
Rank 5 model 2	96.26	4.87

Table A2.2: pLDDT scores for each of 5 models generated for GRLMR and SeR without templates

GRLMR	Avg plddt	Average PAE (angstroms)
Rank 1 model 3	95.99	4.71
Rank 2 model 5	96.34	4.72
Rank 3 model 1	96.45	4.69
Rank 4 model 4	96.40	4.75
Rank 5 model 2	96.17	4.94
SeR	Avg plddt	Average PAE (angstroms)
Rank 1 model 3	96.25	4.72
Rank 2 model 5	96.30	4.76
Rank 3 model 1	96.45	4.70
Rank 4 model 4	96.37	4.82
Rank 5 model 2	96.10	5.00